A Determination of the Neutron Spin Structure Function g_1^n with the 1995 HERMES Data

Thesis by

Bruce D. Bray

In Partial Fulfillment of the Requirements

for the Degree of

Doctor of Philosophy

California Institute of Technology

Pasadena, California

1998

(Submitted July 23, 1997)

Acknowledgements

First, I would like to thank my wife, Laura, for her support, understanding and love through this endeavor. Earning a Ph.D. required many long days and nights in laboratories or in front of a computer and she has been understanding of these many trials since the day we first met.

The Bray and Miller families both deserve special recognition for their support and encouragement during my studies.

Many people have been involved in my education and development as a physicist. I would like to acknowledge and thank Brad Filippone for his guidance, time, and support. I would like to acknowledge many of the members of the HERMES collaboration who made this endeavor worthwhile with their companionship and example. There are far too many members who deserve to be thanked and I will only mention a few. Allison Lung deserves special thanks for the many hours she spent working with and guiding me during the construction and installation of the hodoscopes: Art Mateos and Dirk DeSchepper for their work with me on the NAPA analysis: Ralf Kaiser for the many thankless hours checking particle identification routines.

Finally, a general mention of all the people in Hamburg who made my stay an unforgettable experience.

Abstract

The internal spin structure of the neutron was studied in deep inelastic scattering of longitudinally polarized positrons from a polarized ^3He target in the HERMES spectrometer at the DESY storage ring. The spin asymmetry was measured at an energy of 27.52 GeV in the range $0.023 < x < 0.8$ at an average Q^2 of 2.5 $(\text{GeV/c})^2$. The results are evolved to a constant Q^2 of 2.5 $(\text{GeV/c})^2$ and are in agreement with the world data for the spin dependent structure function g_1^n. The integral of g_1^n ($\int_0^1 g_1^n(x, Q^2 = 2.5(Gev/c)^2)dx$) is found to be $-0.036 \pm 0.012(stat) \pm 0.005(syst) \pm 0.003(extrapolation)$ which is 2 standard deviations from the Ellis-Jaffe Sum Rule and, combined with the world data for the proton, is in good agreement with the Bjorken Sum Rule.

Combining this result with the weak coupling constants F and D implies the quarks carry $(38 \pm 11)\%$ of the nucleon spin and the polarization of the strange sea represents $(-7 \pm 4)\%$ of the nucleon spin.

Contents

3 Particle Identification   **61**

4 Data Analysis   **73**

List of Figures

List of Tables

Chapter 1   Physics Motivation

1.1   Introduction

Much of the current knowledge of nucleon structure has been developed through the deep inelastic scattering (DIS) of lepton beams from nuclear targets. In DIS the high energy leptons are scattered by the constituents of the nucleon. The unpolarized nucleon structure functions determined by DIS have revealed the momentum distribution of partons within protons and neutrons. This was compelling evidence of structure within the nucleon. Quantum Chromo-Dynamics (QCD) implies that the nucleon contains three valence quarks held together by a sea of gluons and virtual quark anti-quark pairs.

The development of polarized lepton beams and polarized nuclear targets has opened a new avenue to probe the spin structure of the nucleon. Previous experiments measuring the spin dependent structure of the nucleon suggested the surprising result that little of the spin of the nucleon is carried by the quarks. [1] [2] [3] [4] [5]

These results have spurred several new experiments to measure the spin structure of the neutron and the proton more accurately. These structure functions will be able to test predictions about the nature of the 'sea' of virtual quarks and gluons binding the nucleus together.

The HERMES experiment is part of a new generation of spin structure experiments underway at SLAC, CERN, and HERA, and has many unique features which will allow it to make a significant contribution to the knowledge of the spin structure of the nucleon:

- A pure internal target eliminates corrections due to dilution and minimizes the external radiative corrections

- An open spectrometer design with a large acceptance allows measurements of semi-inclusive asymmetries in tandem with inclusive measurements for further
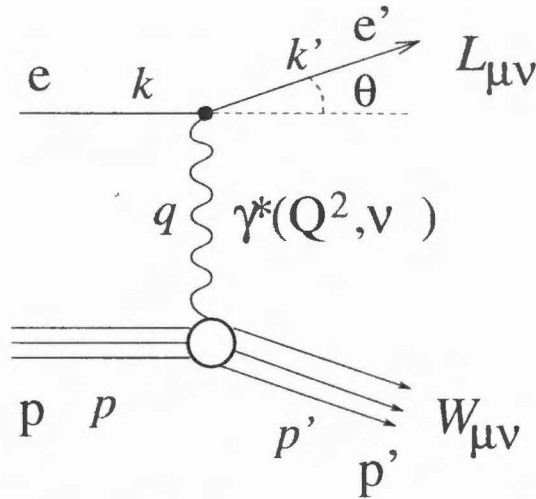
Figure 1.1: Feynman diagram for lowest order DIS lepton-nucleon collision

spin decomposition

- A polarized e^+ beam in a storage ring provides significant luminosity in combination with the internal target

- A measurement of H,D, and ^3He spin structure with the same spectrometer at the same kinematics reduces problems from combining the spin structure functions from different experiments

This thesis will discuss the result of the recent experiment to measure the spin-dependent structure function g_1^n at HERMES in 1995.

1.2   The Formalism of Polarized Deep Inelastic Scattering

The formalism for the deep inelastic scattering of leptons from a nucleon can be described in terms of Feynman diagrams. In the first order approximation, a virtual photon is exchanged between the lepton and nucleon as shown in Figure 1.1. The quantities in the figure and used in this discussion of deep inelastic scattering are defined in Table 1.1.

At high energies, the negative invariant mass of the virtual photon, the energy transfer, and the invariant mass of the final state have the following values in the lab frame:

Four Vector	Lab Frame Components	Definition
k	$(E, \vec{k}\,)$	incident positron momentum
k'	$(E', \vec{k'}\,)$	scattered positron momentum
q	$(\nu, \vec{q}\,)$	virtual photon momentum
p	$(M, \vec{0}\,)$	initial nucleon momentum
p'	$(M + \nu, \vec{q}\,)$	baryon final state momentum

Table 1.1: DIS variables

$$Q^2 = -q^2 = (k - k')^2 \overset{lab}{=} -4EE' sin^2(\Theta/2) \tag{1.1}$$

$$\nu = \frac{p \cdot q}{M} \overset{lab}{=} E - E' \tag{1.2}$$

$$W^2 = p'^2 \overset{lab}{=} M^2 + 2M\nu - Q^2 \tag{1.3}$$

Calculating the doubly differential cross section for the process in Figure 1.1 by the standard prescriptions for QED [6] yields:

$$\frac{d^2\sigma}{d\Omega dE'} = \frac{4\alpha^2}{Q^4} \frac{E'}{E} L_{\mu\nu} W^{\mu\nu} \tag{1.4}$$

where α is the fine structure constant and the tensors $L_{\mu\nu}$ and $W^{\mu\nu}$ describe the leptonic and hadronic currents.

The leptonic tensor can be calculated from QED and takes the form of a sum over final spin states:

$$L_{\mu\nu} = \Sigma_{s'} \overline{u}(k', s') \gamma_\mu u(k, s) \overline{u}(k, s) \gamma_\nu u(k', s') \tag{1.5}$$

$$= k'_\mu k_\nu + k'_\nu k_\mu - g_{\mu\nu} k' \cdot k + im\epsilon_{\mu\nu\alpha\beta} s^\alpha q^\beta \tag{1.6}$$

$$= L^S_{\mu\nu} + L^A_{\mu\nu} \tag{1.7}$$

where m, the lepton mass, is included to cancel the normalization factor in the spin vector.

The spin symmetric and antisymmetric terms are:

$$L_{\mu\nu}^{S} = k_{\mu}' k_{\nu} + k_{\nu}' k_{\mu} - g_{\mu\nu} k' \cdot k \tag{1.8}$$

$$L_{\mu\nu}^{A} = im\epsilon_{\mu\nu\alpha\beta} s^{\alpha} q^{\beta} \tag{1.9}$$

The advantage of lepton - nucleon scattering is that this tensor is known. The structureless leptons can be used to probe the structure of the nucleon, that is determine the unknown hadronic tensor $W^{\mu\nu}$ from its tensor product with the known lepton tensor $L_{\mu\nu}$.

Similar to the lepton current, the hadronic current can be decomposed into spin symmetric and spin anti-symmetric components:

$$W^{\mu\nu} = W_{S}^{\mu\nu} + W_{A}^{\mu\nu} \tag{1.10}$$

Furthermore, this arbitrary tensor can be decomposed into four unknown structure functions. Parity and time reversal invariance constraints, hermiticity, and current conservation determine that these are the only independent components for electromagnetic scattering.

The symmetric term is defined as [7]:

$$W_{S}^{\mu\nu} = -(g^{\mu\nu} - \frac{q^{\mu}q^{\nu}}{q^2})W_1(\nu, Q^2) + \frac{1}{M^2}(P^{\mu} - \frac{P \cdot q}{q^2}q^{\mu})(P^{\nu} - \frac{P \cdot q}{q^2}q^{\nu})W_2(\nu, Q^2) \tag{1.11}$$

and the antisymmetric term:

$$W_{A}^{\mu\nu} = M\epsilon^{\mu\nu\alpha\beta}q_{\alpha}s_{\beta}G_1(\nu, Q^2) + \frac{1}{M}\epsilon^{\mu\nu\alpha\beta}q_{\alpha}(P \cdot q s_{\beta} - S \cdot q P_{\beta})G_2(\nu, Q^2) \tag{1.12}$$

The structure functions W_1 and W_2 describe the spin averaged scattering which is described in standard discussions of DIS [8]. Just as the spin independent portion of the hadronic tensor amplitude can be described in terms of two structure functions (W_1 and W_2), the spin dependent portion contains two spin dependent structure

functions (G_1 and G_2).

1.3 The Polarized Structure Functions

When the lepton is in a state of positive helicity (spin parallel to the beam momentum), the difference between cross sections for nucleon polarizations at an angle ϕ and at an angle $\phi + \pi$ summing over the final lepton and hadron polarizations is [9]

$$\frac{d\sigma^{\uparrow(\phi)}}{dQ^2 dE'} - \frac{d\sigma^{\uparrow(\phi+\pi)}}{dQ^2 dE'} = \frac{4\pi\alpha^2}{E^2 Q^2}([E\cos\phi + E'\cos(\theta - \phi)]MG_1(\nu, Q^2) \\ -2EE'[\cos\phi - \cos(\theta - \phi)]G_2(\nu, Q^2)). \tag{1.13}$$

The angles are the polarization axis (ϕ) and the scattering angle (θ) relative the the direction of the lepton's momentum. For a longitudinally polarized target ($\phi = 0$), which was the case for the 1995 HERMES data. this reduces to

$$\frac{d\sigma^{\uparrow(\uparrow)}}{dQ^2 dE'} - \frac{d\sigma^{\uparrow(\downarrow)}}{dQ^2 dE'} = \frac{4\pi\alpha^2}{E^2 Q^2}([E + E'\cos(\theta)]MG_1(\nu, Q^2) - Q^2 G_2(\nu, Q^2)). \tag{1.14}$$

For a transversely polarized target ($\phi = \pi/2$). this asymmetry can be expressed as

$$\frac{d\sigma^{\uparrow(\rightarrow)}}{dQ^2 dE'} - \frac{d\sigma^{\uparrow(\leftarrow)}}{dQ^2 dE'} = \frac{4\pi\alpha^2}{E^2 Q^2}[E'\sin(\theta)](MG_1(\nu, Q^2) + 2EG_2(\nu, Q^2)). \tag{1.15}$$

It is possible to determine the spin dependent structure functions from these doubly differential cross sections, but it is more practical experimentally to make instead asymmetry measurements. The systematic errors of the measurement of these structure functions can be reduced by calculating an asymmetry as opposed to a difference of doubly differential cross sections. The parallel and transverse asymmetries can be defined as:

$$A^{\parallel} = \frac{\sigma^{\uparrow\downarrow} - \sigma^{\uparrow\uparrow}}{\sigma^{\uparrow\uparrow} + \sigma^{\uparrow\uparrow}} \tag{1.16}$$

$$A^{\perp} = \frac{\sigma^{\uparrow\rightarrow} - \sigma^{\uparrow\leftarrow}}{\sigma^{\uparrow\rightarrow} + \sigma^{\uparrow\leftarrow}}. \tag{1.17}$$

These asymmetries can be related to the asymmetries for the virtual photons scattering from the nucleon

$$A_1 = \frac{\sigma_{1/2} - \sigma_{3/2}}{\sigma_{1/2} + \sigma_{3/2}} = \frac{M\nu G_1(\nu, Q^2) - Q^2 G_2(\nu, Q^2)}{W_1(\nu, Q^2)} \tag{1.18}$$

where $\sigma_{1/2}$ and $\sigma_{3/2}$ are the virtual photon absorption cross sections with the photon and nucleon spins anti-parallel and parallel.

$$A_2 = \frac{\sqrt{Q^2}}{W_1(\nu, Q^2)}(MG_1(\nu, Q^2) + \nu G_2(\nu, Q^2)). \tag{1.19}$$

The relation is as follows:

$$A^{\|} = \frac{\sigma^{\uparrow\downarrow} - \sigma^{\uparrow\uparrow}}{\sigma^{\uparrow\downarrow} + \sigma^{\uparrow\uparrow}} = D(A_1 + \eta A_2) \tag{1.20}$$

$$A^{\perp} = \frac{\sigma^{\uparrow\rightarrow} - \sigma^{\uparrow\leftarrow}}{\sigma^{\uparrow\rightarrow} + \sigma^{\uparrow\leftarrow}} = d(A_2 - \zeta A_1) \tag{1.21}$$

Where

$$D = \frac{1 - (E'/E)\epsilon}{1 + \epsilon R} \tag{1.22}$$

can be regarded as the depolarization of the virtual photon and

$$R = \sigma_L/\sigma_T \tag{1.23}$$

is the ratio of longitudinal and transverse virtual photon cross sections. The kinematic factor η is given by

$$\eta = \epsilon\sqrt{Q^2}/(E - E'\epsilon). \tag{1.24}$$

For the transverse case the kinematic factors are

$$d = D\sqrt{\frac{2\epsilon}{1+\epsilon}} \tag{1.25}$$

and

$$\zeta = \eta(\frac{1+\epsilon}{2\epsilon}). \tag{1.26}$$

In these formulae

$$\epsilon = [1 + 2(1 + \nu^2/Q^2)tan^2(\frac{1}{2}\theta)]^{-1} \tag{1.27}$$

is the ratio of longitudinal to transverse virtual photon fluxes. The factors η and ζ are small so the photon asymmetries are approximately proportional to the longitudinal and transverse asymmetries. The factor D represents the polarization of the virtual photon for a fully polarized lepton.

The photon asymmetries can be written in terms of the measured counting asymmetries by inverting these equations to give

$$A_1 = \frac{A_{\|}}{D(1 + \zeta\eta)} - \frac{\eta A_{\perp}}{d(1 + \zeta\eta)} \simeq \frac{A_{\|}}{D} \tag{1.28}$$

and

$$A_2 = \frac{A_{\perp}}{d(1 + \zeta\eta)} - \frac{\zeta A_{\|}}{D(1 + \zeta\eta)} \simeq \frac{A_{\perp}}{d}. \tag{1.29}$$

If A_1 is written in terms of $A_{\|}$ and A_2, we obtain a formula which will be used throughout this analysis.

$$A_1 = \frac{A_{\|}}{D} - \eta A_2. \tag{1.30}$$

The photon asymmetry A_1 is bound by

$$|A_1| \leq 1 \tag{1.31}$$

while A_2 has the restriction [10]
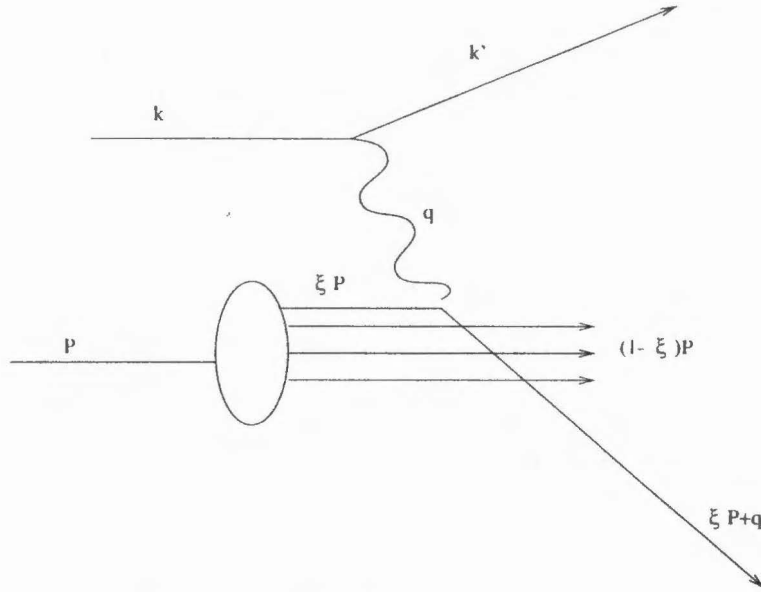
Figure 1.2: DIS in the quark-parton model

$$|A_2| \leq \sqrt{R}. \tag{1.32}$$

1.4 The Quark Parton Model

In the quark-parton model [11] [12], a nucleon is composed of point-like constituents, each carrying a fraction of the total nucleon momentum. In the limit of an infinite momentum frame, time dilation suppresses any interactions between these partons.

Consider the scattering of a virtual photon with four momentum q as shown in Figure 1.2. For sufficiently large Q^2, during the lifetime of the virtual photon $(1/\sqrt{Q^2})$ the constituent partons can be considered to be free.

In the Bjorken limit $(Q^2 \to \infty$ and $\nu \to \infty$ with $x = \frac{Q^2}{2M\nu}$ constant) we can then consider deep inelastic scattering from a nucleon to be elastic scattering from a free quark and write

$$(\xi P + q)^2 = m^2 \tag{1.33}$$

where m is the mass of the parton, P is the momentum of the nucleon, and ξ is the

fraction of the nucleon momentum carried by the struck quark. In the Bjorken limit we neglect terms proportional to m^2 (the mass of the parton) and M^2 (the mass of the nucleon) to observe the behavior of the terms proportional to Q^2 and $M\nu$. The equation for the momentum fraction of the struck quark then reduces to

$$\xi = \frac{Q^2}{2M\nu} = x. \tag{1.34}$$

The Bjorken scaling variable x represents the fraction of the parent nucleon momentum which was carried by the scattered parton.

It is convenient to define a new set of four dimensionless structure functions ($F_{1,2}$ and $g_{1,2}$) for discussions of this high energy limit:

$$MW_1(\nu, Q^2) = F_1(x, Q^2) \tag{1.35}$$

$$\nu W_2(\nu, Q^2) = F_2(x, Q^2) \tag{1.36}$$

$$M^2\nu G_1(\nu, Q^2) = g_1(x, Q^2) \tag{1.37}$$

$$M\nu^2 G_2(\nu, Q^2) = g_2(x, Q^2). \tag{1.38}$$

In the Bjorken limit, these new structure functions are predicted to be functions of only x independent of Q^2. This behavior is called scaling. Experiments are performed at finite ν and Q^2 where scaling violations are expected and experimental results are presented in terms of g_1 and g_2. These structure functions take the following form at finite Q^2

$$g_1 = \frac{F_2}{2x(1+R)}[A_1 + \frac{\sqrt{Q^2}}{\nu} A_2] \tag{1.39}$$

and

$$g_2 = \frac{F_2}{2x(1+R)}[A_2 \frac{\nu}{\sqrt{Q^2}} - A_1]. \tag{1.40}$$

Rewriting the structure function g_1 in terms of the observed asymmetry $A_\parallel$ and A_2, we obtain

$$g_1 = \frac{F_2}{2x(1+R)}[\frac{A_\parallel}{D} + (\frac{\sqrt{Q^2}}{\nu} - \eta)A_2]. \tag{1.41}$$

These structure functions can be interpreted in terms of the momentum distribution of the partons in the nucleon, written as:

$$F_1(x) = \frac{1}{2}\Sigma_i f_i(x)c_i^2 \tag{1.42}$$

$$F_2(x) = x\Sigma_i f_i(x)c_i^2 \tag{1.43}$$

where the index i runs over flavors, c_i is the charge and $f_i(x)$ is the probability of finding a parton of flavor i and momentum fraction x in the nucleon.

In an analogous fashion, $g_1(x)$ and $g_2(x)$ can be interpreted in terms of the helicity dependent momentum distributions of the partons

$$g_1(x) = \frac{1}{2}\Sigma_i(f_i^+(x) - f_i^-(x))c_i^2 \tag{1.44}$$

$$g_1(x) + g_2(x) = \frac{1}{2Mx}\Sigma_i(f_i^{+T}(x) - f_i^{-T}(x))c_i^2 m_i \tag{1.45}$$

where $f_i^+(x)$ is the probability of finding a parton of flavor i, with momentum fraction x and the same helicity as the parent nucleon.

In the Bjorken limit. the virtual Compton asymmetries A_1 and A_2 can be written as

$$A_1 = \frac{g_1 - \frac{4M^2x^2}{Q^2}g_2}{F_1} \tag{1.46}$$

$$A_2 = \frac{2M_{bj}}{\sqrt{Q^2}}\frac{g_1 + g_2}{F_1}. \tag{1.47}$$

A_1 has a simple interpretation in the Bjorken limit. As $Q^2 \to \infty$, A_1 becomes g_1/F_1 both of which have interpretations in the parton model. Thus, A_1 can be interpreted in terms of the spin distribution of the nucleon. In the Bjorken limit
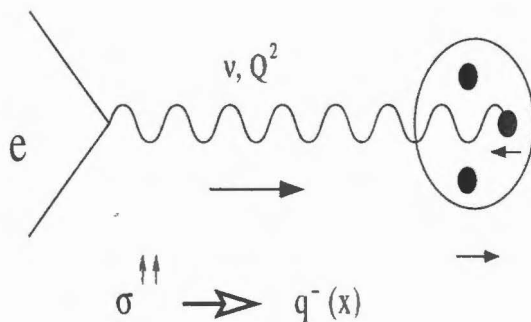
Figure 1.3: $\sigma^{\uparrow\uparrow}$ in the Bjorken Limit
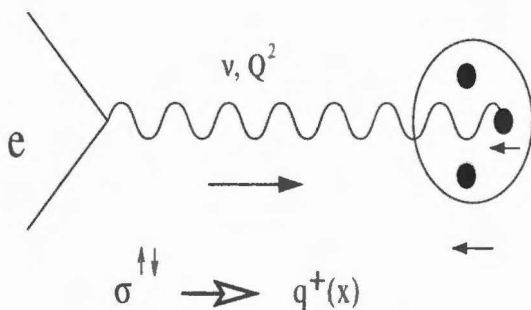
Figure 1.4: $\sigma^{\uparrow\downarrow}$ in the Bjorken Limit

$$A_1 = \frac{g_1}{F_1} = \frac{\Sigma_i(f_i^+(x) - f_i^-(x))e_i^2}{\Sigma_i f_i(x)e_i^2} \simeq \frac{1}{D}\frac{\sigma^{\uparrow\downarrow} - \sigma^{\uparrow\uparrow}}{\sigma^{\uparrow\uparrow} + \sigma^{\uparrow\uparrow}}. \tag{1.48}$$

This a consequence of helicity conservation in the ultra-relativistic limit. The sign convention of A_1 can be understood heuristically in terms of the spin of the quarks that the lepton scatters from within the nucleon as shown in Figures 1.3 and 1.4. Neglecting the masses of the leptons and partons, the positive helicity lepton can only couple to a positive helicity quark in the center of mass frame. If the spin of the nucleon is parallel to the beam spin, this selects partons with spins opposite the nucleon spin (f^-) (Figure 1.3).

We can calculate A_1 for a SU(6) model of the nucleon with three constituent quarks. Given the proton wave function [13]:

$$|p> = \frac{1}{\sqrt{2}}[\Phi_{MS}\hat{\chi}_{MS} + \Phi_{MA}\hat{\chi}_{MA}] \qquad (1.49)$$

with

$$\Phi_{MS}^{'} = \frac{1}{\sqrt{6}}[udu + duu - 2uud] \qquad (1.50)$$

$$\Phi_{MA} = \frac{1}{\sqrt{2}}[udu - duu] \qquad (1.51)$$

$$\hat{\chi}_{MS} = \frac{1}{\sqrt{6}}[\uparrow\downarrow\uparrow + \downarrow\uparrow\uparrow - 2\uparrow\uparrow\downarrow] \qquad (1.52)$$

$$\hat{\chi}_{MA} = \frac{1}{\sqrt{2}}[\uparrow\downarrow\uparrow - \downarrow\uparrow\uparrow]. \qquad (1.53)$$

It is easy to show

$$A_1^p = \frac{4/9(u\uparrow - u\downarrow) - 1/9(d\uparrow - d\downarrow)}{4/9(u\uparrow - u\downarrow) + 1/9(d\uparrow - d\downarrow)} = \frac{5}{9} \qquad (1.54)$$

or interchanging u and d $A_1^n = 0$. These naive predictions might be expected to be valid at medium values (~ 0.3) of x where the valence quarks dominate.

1.5 Spin Structure Function Sum Rules

The initial motivating factor to measure spin dependent structure functions was to test two sum rules: the Bjorken and Ellis-Jaffe sum rules, which relate the integral of the spin structure functions $g_1^{p,n}$ to the baryon weak decay couplings.

Bjorken Sum Rule

The Bjorken sum rule [14] relates the spin structure functions g_1^p and g_1^n to the ratio of the axial to vector couplings, g_A/g_V observed in beta decay. The Bjorken sum Rule is amazing because it relates high energy physics to weak nuclear decays with only the assumption of isospin symmetry and current algebra. In the Bjorken limit it can be written as

$$\int_0^1 [g_1^p(x) - g_1^n(x)]dx = \frac{1}{6}|\frac{g_A}{g_V}| = 0.210 \pm 0.002. \tag{1.55}$$

The Bjorken sum rule has been derived in terms of an operator product expansion in order to calculate the QCD corrections at finite Q^2. For three quark flavors it takes the form [15]

$$\int_0^1 [g_1^p(x) - g_1^n(x)]dx = \frac{1}{6}|\frac{g_A}{g_V}|[[1 - \frac{\alpha_s(Q^2)}{\pi} - 3.5833(\frac{\alpha_s(Q^2)}{\pi})^2 - 20.2153(\frac{\alpha_s(Q^2)}{\pi})^3] \tag{1.56}$$

The HERMES data is taken at an average Q^2 of 2.5 GeV/c^2. At this energy transfer the strong coupling constant (α_s) is [16] given by

$$\alpha_s(Q^2 = 2.5(GeV/c)^2) = 0.305. \tag{1.57}$$

The Bjorken sum rule then has the numerical value

$$\int_0^1 [g_1^p(x, Q^2 = 2.5(GeV/c)^2) - g_1^n(x, Q^2 = 2.5(GeV/c)^2)]dx = \frac{1}{6}|\frac{g_A}{g_V}|[0.8506]$$
$$= 0.179 \pm 0.008. \tag{1.58}$$

Ellis-Jaffe Sum Rule

The Ellis-Jaffe sum rules [17] were motivated by the original g_1^p experiments. A sum rule relating to just g_1^p was derived because at the time no neutron data was anticipated in the near future. The Ellis-Jaffe sum rules make two additional assumptions to relate the structure functions of the proton and neutron to F and D the symmetric and antisymmetric constants describing baryon octet decay. The assumptions are

- exact SU(3) symmetry in the baryon octet decays

- no net strange sea polarization

The sum rules can be written as

$$\int_0^1 g_1^p(x)dx = \frac{1}{12}\frac{g_A}{g_V}(1 + \frac{5}{3}\frac{3F - D}{F + D}) \tag{1.59}$$

and

$$\int_0^1 g_1^n(x)dx = \frac{1}{12}\frac{g_A}{g_V}(-1 + \frac{5}{3}\frac{3F-D}{F+D}).$$ (1.60)

The violation of the Ellis-Jaffe sum rule is often interpreted in terms of the spin asymmetry of the strange sea.

Defining a new variable $\Delta i = \int_0^1 (f_i^+(x) - f_i^-(x))dx$ as the total fraction of the helicity carried by a quark flavor, the integrals of the structure functions for the proton and neutron can be written as:

$$\int_0^1 g_1^p(x)dx \equiv \Gamma_1^p = \frac{4}{18}\Delta u + \frac{1}{18}\Delta d + \frac{1}{18}\Delta s$$ (1.61)

$$\int_0^1 g_1^n(x)dx \equiv \Gamma_1^n = \frac{1}{18}\Delta u + \frac{4}{18}\Delta d + \frac{1}{18}\Delta s.$$ (1.62)

It is convenient to replace the flavor helicities with the singlet $(\Delta u + \Delta d + \Delta s)$, triplet $(\Delta u - \Delta d)$, and octet $(\Delta u + \Delta d - 2\Delta s)$ terms. These can be related to the baryon octet decay constants by writing F and D in terms of the quark helicities.

$$\Delta u - \Delta d = F + D = |\frac{g_A}{g_V}|$$ (1.63)

$$\Delta u + \Delta d - 2\Delta s = 3F - D$$ (1.64)

$$\Delta u + \Delta d + \Delta s = \Delta q.$$ (1.65)

The current best fit for F and D is [18]

$$F = 0.459 \pm 0.008$$
$$D = 0.798 \pm 0.008$$
$$F/D = 0.575 \pm 0.016.$$ (1.66)

The structure function integrals are decomposed into singlet and non-singlet terms to include QCD corrections from an operator-product expansion.

$$\Gamma_1^n = -\frac{1}{12}(\Delta u - \Delta d)C_{ns} + \frac{1}{36}(\Delta u + \Delta d - 2\Delta s)C_{ns} + \frac{1}{9}(\Delta u + \Delta d + \Delta s)C_s. \quad (1.67)$$

$$\Gamma_1^p = +\frac{1}{12}(\Delta u - \Delta d)C_{ns} + \frac{1}{36}(\Delta u + \Delta d - 2\Delta s)C_{ns} + \frac{1}{9}(\Delta u + \Delta d + \Delta s)C_s. \quad (1.68)$$

where the perturbative QCD corrections take the form [19]:

$$C_{ns} = 1 - (\frac{\alpha_s(Q^2)}{\pi}) - 3.5833(\frac{\alpha_s(Q^2)}{\pi})^2 - 20.2153(\frac{\alpha_s(Q^2)}{\pi})^3 \quad (1.69)$$

$$C_s = 1 - \frac{1}{3}(\frac{\alpha_s(Q^2)}{\pi}) - 0.5495(\frac{\alpha_s(Q^2)}{\pi})^2. \quad (1.70)$$

These perturbative corrections are necessary to make a meaningful test of the Ellis-Jaffe sum rule at finite Q^2. At an average Q^2 of 2.5 $(GeV/c)^2$, these sum rules make the following predictions for the proton and neutron:

$$\Gamma_1^n = -0.013 \pm 0.005 \quad (1.71)$$

$$\Gamma_1^p = 0.165 \pm 0.005 \quad (1.72)$$

1.6 Spin Decomposition of the Nucleon

The spin of the nucleon can be decomposed into parts due to the quarks, the gluons and the angular momentum.

$$\Sigma = 1/2 = 1/2\Delta q + \Delta G + L_q + L_g \quad (1.73)$$

where L_q is the orbital angular momentum of the quarks, ΔG is the gluon spin contribution, and L_g is the angular momentum of the gluons. Since the gluons carry about half the momentum of the nucleon, it would not be surprising for them to carry

a significant fraction of the spin as well.

DIS alone does not provide enough information for the decomposition of the nucleon spin. However, some additional assumptions and measurements can allow an extraction of Δq.

The proton and neutron integrals can be expressed as:

$$\int_0^1 g_1^p(x)dx = \Gamma_1^p = I_3 + I_8 + I_0 \tag{1.74}$$

$$\int_0^1 g_1^n(x)dx = \Gamma_1^n = -I_3 + I_8 + I_0 \tag{1.75}$$

where I_3, I_8, and I_0 are the triplet octet and singlet terms from equations 1.67 and 1.68.

Solving these equations for $\Delta q = \Delta u + \Delta d + \Delta s$, one can solve for the nucleon spin carried by the quarks.

$$\Delta q = \frac{9}{C_s}(\Gamma_1^p - (\frac{F+D}{12} + \frac{3F-D}{36})C_{ns}) \tag{1.76}$$

$$\Delta q = \frac{9}{C_s}(\Gamma_1^n - (-\frac{F+D}{12} + \frac{3F-D}{36})C_{ns}) \tag{1.77}$$

or:

$$\Delta q = \frac{9}{C_s}(\frac{\Gamma_1^p + \Gamma_1^n}{2} - \frac{3F-D}{36}C_{ns}) \tag{1.78}$$

Assuming SU(3) symmetry, it is possible to separate the components of the quarks' spin with the measurements of any three of the following: Γ_1^n, Γ_1^p, F+D = $\Delta u - \Delta d$, and 3F-D = $\Delta u - \Delta d - 2\Delta s$.

1.7 World Data Before HERMES

Since the first measurement of g_1^p [20], a series of experiments at SLAC and CERN [1] [2] [3] [4] [5] have measured the spin structure functions with increasing accuracy. These measurements have indicated a 'spin crisis' because the Ellis-Jaffe sum rules
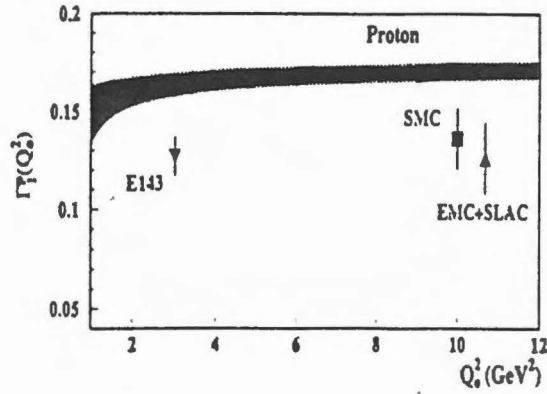
Figure 1.5: World Data for Γ_1^p
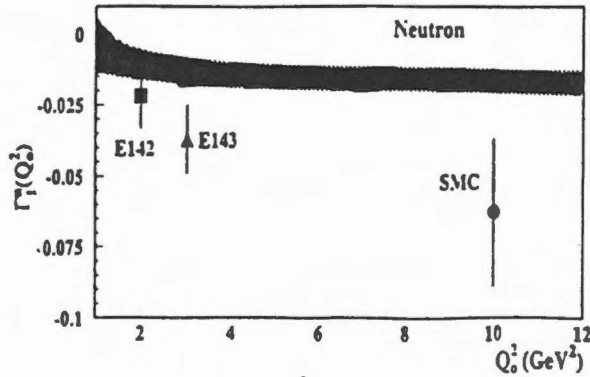
Figure 1.6: World Data for Γ_1^n

appear to be violated. New data from HERMES and SLAC (E154 and E155) will contribute to the understanding of spin structure.

Current results for the Ellis-Jaffe sum rules for the proton and neutron from these experiments are shown in Figures 1.5 and 1.6. The violation of the Ellis-Jaffe sum rules seen in this data have sparked much interest in what carries the spin of the nucleon.

1.8 Semi-Inclusive Physics

The HERMES spectrometer is designed to measure semi-inclusive asymmetries concurrently with the inclusive measurements. (The spectrometer is described in Chapter

2.) Additional information about the spin distribution of the nucleon can be determined by measuring the asymmetries with the leading hadron detected in coincidence with the scattered lepton. For example, the K^- meson ($\bar{u}s$) is an all sea object and should be sensitive to the spin of the strange quark sea Δs. Only a limited amount of hadron identification was available for the 1995 running period (see Section 2.Cerenkov) and these results will not be discussed further. The semi-inclusive physics at HERMES will be significantly extended for the 1996 to 1999 running period.

HERMES is the only spin structure experiment which can measure semi-inclusive asymmetries with good particle identification. These measurements will become increasingly important as our knowledge of the inclusive measurements improves.

Chapter 2   Experimental Apparatus

2.1   HERA

The HERMES experiment is installed in the East hall of the HERA collider ring at DESY (Figure 2.1). The HERA ring is a high energy, high current positron and proton colliding beam facility. The beams are stored in 6.3 km circumference rings with energies of 27.5 GeV (positrons) and 820 GeV (protons). There are four intersection points for the beams at the North, South, East and West Halls. Two collider experiments, H1 and ZEUS, are installed in the North and South Halls and two fixed target experiments, HERMES and HERA-B (b quark production with the proton beam), are in the East and West Halls. HERA was designed to allow the storage of spin polarized positrons and provides longitudinally polarized positrons at the East Hall interaction point. At the East hall, the proton and positron beams have been horizontally separated by 72 cm. This allows HERMES to operate an internal target without affecting the proton beam conditions.
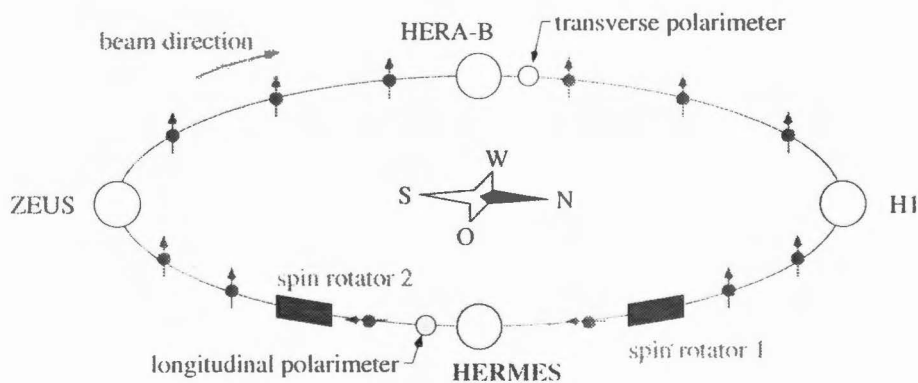
Figure 2.1: Polarized Electrons in a Storage Ring
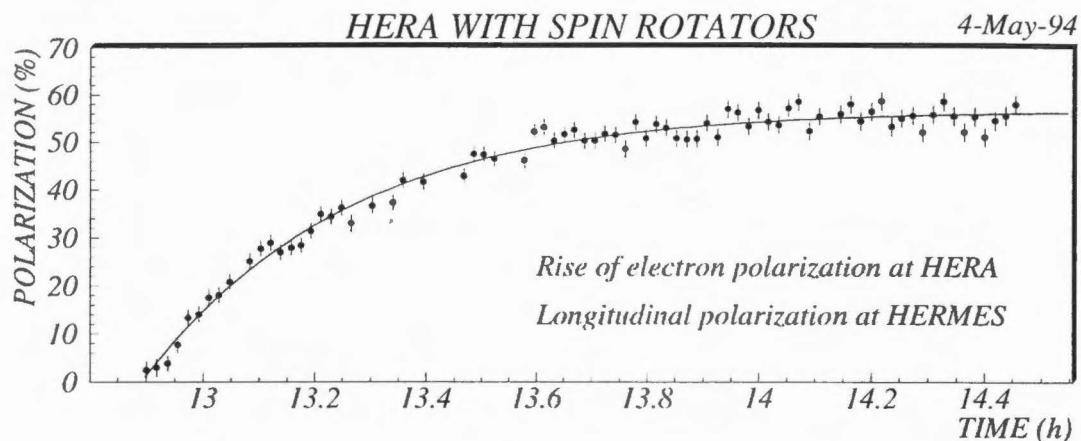
Figure 2.2: Polarized Electrons in the HERA Storage Ring

2.2 The Polarized Positron Storage Ring

The development of techniques to polarize the positron beam and measure the polarization were crucial for the approval of the HERMES experiment and represent an enormous technical achievement.

The beam is polarized by the Sokolov-Ternov effect [21]. Positrons in a storage ring can become polarized parallel to the magnetic guide field because of a small difference in the spin flip synchrotron emission rates. The spin flip represents only a very small fraction of the synchrotron emission process so the polarization tends to build-up over a long time scale. [22]

The polarization increases in time exponentially with

$$P(t) = P_{ST}(1 - e^{-t/\tau_P}). \tag{2.1}$$

For an ideal ring, the time constant for the polarization rise is

$$\tau_P = \frac{8 m_e}{5\sqrt{3} r_e} \frac{\rho^3}{\gamma^5} \tag{2.2}$$

with r_e the classical electron radius and ρ the bending radius of the magnetic field (707 m for HERA). At 27.5 GeV, $\gamma = E/m_e = 54000$ and the time constant $\tau_P = 37$ minutes. Figure 2.2 shows the rise of the beam polarization in the positron ring.

P_{ST} of 92.4% is the theoretical maximum for the equilibrium polarization with a

homogeneous magnetic field. In practice, the polarization must be optimized for the non-homogeneous fields of the ring.

It is important to minimize any depolarization effects because of the slow build up time of the Sokolov-Ternov effect. Any out of plane bending in the beam optics will cause a reduction in the polarization achieved. A positron with a betatron orbit (an out of plane oscillation) will feel non-vertical fields in the quadrupoles which causes spin diffusion.

The solution for a closed betatron orbit is slightly more complicated but the basic result is the same as the polarization in a constant magnetic field. A discussion of the closed orbit solution [23] adds an additional term to describe the spin precession around the axis of the magnetic field due to the positrons gyromagnetic ratio. The frequency of the spin precession ($\nu = \frac{\gamma(g-2)}{2}$) is referred to as the spin tune. Resonant depolarization occurs when the perturbing fields add coherently over orbits of the ring. Resonances are expected to satisfy

$$\nu = k \pm l\nu_h \pm m\nu_r \pm n\nu_s. \tag{2.3}$$

k,l,m,n are integers, ν_h and ν_v are the horizontal and vertical betatron tunes and ν_s is the synchrotron tune. [24]

Special tunes are used to maximize the polarization of the positron beam. The tunes are empirically optimized to maximize the beam polarization.

The polarization generated by the Sokolov-Ternov effect is transverse but a longitudinal polarization is needed for the asymmetry measurements. Two spin rotators (Figure 2.1) are used to first rotate the positron polarization to longitudinal before the HERMES interaction point and then to rotate the beam polarization back to transverse. The rotators [25] are designed to rotate the spin direction by 90° without changing the beam position or slope at the interaction point. Switching the longitudinal beam polarization requires the movement and alignment of the spin rotator magnets. The beam polarization was not switched during the 1995 run because of the several day shutdown required for this realignment.
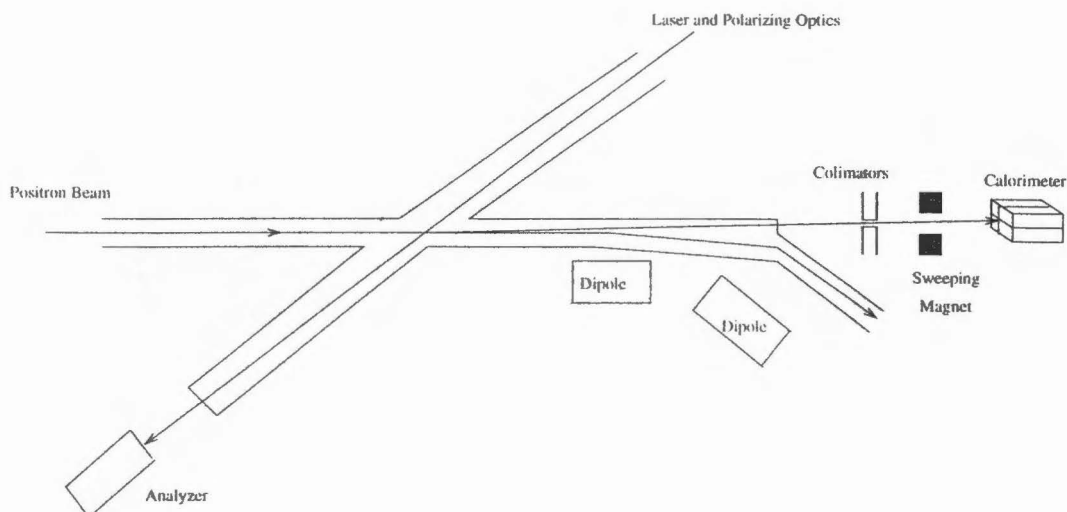
Figure 2.3: Schematic Diagram of the Compton Polarimeter

2.2.1 Measurement of the Beam Polarization

A Compton laser polarimeter [26] measures the polarization of the positron beam. The scattering cross section of circularly polarized photons on transversely polarized positrons is asymmetric with respect to the polarization axis of the positrons.

The laser light is scattered almost head on with the positron beam and is boosted from 514 nm to high energies ($E_\gamma = 0$ to 13.8 GeV). The scattered photons are collinear with the positron beam. The energy and point of incidence is measured with a sampling calorimeter composed of lead-tungsten and scintillator sheets. Figure 2.3 shows the layout of the polarimeter in the storage ring. A calorimeter divided into four quadrants can measure the total energy and point of incidence from the energies deposited in each quadrant.

The polarization of the laser is switched at 90 Hz and the asymmetry in the calorimeter as a function of vertical (parallel to beam polarization) position can be converted to a beam polarization. [22]

The polarization measured with the beam polarimeter is calibrated with rise time measurements. Resonant depolarization can be used to quickly depolarize the beam. A measurement of the buildup of the polarization versus time can be used to determine P_{MAX} for the beam.
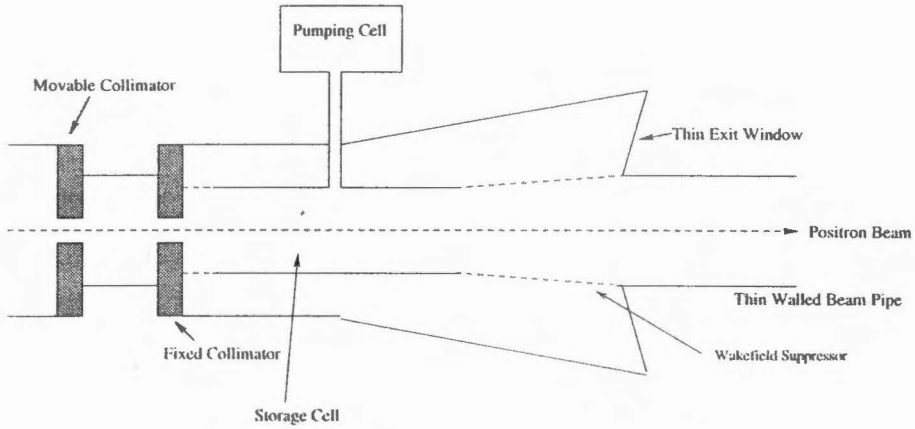
Figure 2.4: Polarized Positrons in a Storage Ring

$$P_{compton}(t) = kP_{MAX}(1 - e^{-(t-t_0)\frac{C}{P_{MAX}}}). \tag{2.4}$$

The constant C can be extracted from machine parameters and is independent of any depolarization mechanisms which may affect the maximum polarization. The values of P_{MAX} and k are determined from a fit to the polarization risetime and asymptotic value after depolarization. The 'k factor' is used to calibrate the beam polarimeter measurements. The uncertainty in the beam polarization is dominated by a 5% uncertainty in the 'k factor'.

2.2.2 Synchrotron Radiation

Bends in the positron ring have been minimized near the East Hall to reduce the amount of synchrotron radiation incident on the experiment. A double collimator system is used to absorb the remaining synchrotron radiation before the target. A fixed collimator is located close to the target and a second movable collimator is located 2 m upstream of the target as shown in Figure 2.4. After filling the ring, the movable collimator is closed to 3.0 mm from the beam axis. The two collimators are designed to shield the target cell from radiation produced in the magnets before the target and radiation which scatters from the first collimator.

2.3 The HERMES ^{3}He Target

The development of highly polarized ^{3}He internal targets has been very important in the field of nuclear physics. With high intensity circularly polarized laser light it is possible to achieve atomic polarizations of up to 80% for ^3He in sealed cells by metastability exchange. [27]

The HERMES experiment uses a slightly more complicated apparatus. The He atoms are polarized in a pumping cell and flow into a storage cell where they cross the positron beam several times before being pumped away. The polarizations attained in a flowing cell are lower than a sealed cell.

In order to polarize the helium atoms, they are first excited by a weak rf discharge (f $\sim$ 200kHz) in the pumping cell to the 2^3S_1 level. Circularity polarized laser light at 1083 nm excites the $2^3S_1 \rightarrow 2^3P$ transition and the polarization is transmitted to the nuclei by hyperfine interactions. Finally, the polarization is transferred to the ground state nuclei by metastability exchange.

$$^3\vec{H}e(2^3S_1) +^3 He(1^1S_0) \longrightarrow^3 \vec{H}e(1^1S_0) +^3 He(2^3S_1) \tag{2.5}$$
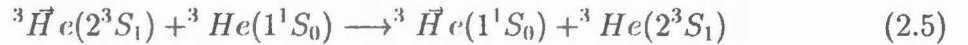
At HERMES the gas is polarized in a pumping cell and the polarized gas flows into the positron ring. A T-shaped target cell (Figure 2.5) is used to store the polarized gas in the positron ring. The target cell is elliptically shaped and large enough that scattering from the cell walls was negligible. Figure 2.6 shows the closest approach of reconstructed tracks to the beam. The storage cell has no end caps so the beam interacts with a pure ^3He target with no dilution from other atoms. The storage cell increases the target density 100-fold over a gas jet and can create target densities of the order of 10^{15} atoms/cm^2 for the ^{3}He target.

The target thickness in the HERMES storage cell is determined to have little effect on the positron lifetime in the ring. The lifetime of the beam for atomic bremsstrahlung from the target gas is [28]

$$\tau_{gas}(Z,n) = T_0 \frac{1}{\ln(\frac{183}{Z^{1/3}})} \frac{1}{Z(Z+1)} \frac{8.1\text{x}10^{25}\text{atoms/cm}^2}{n}, \tag{2.6}$$
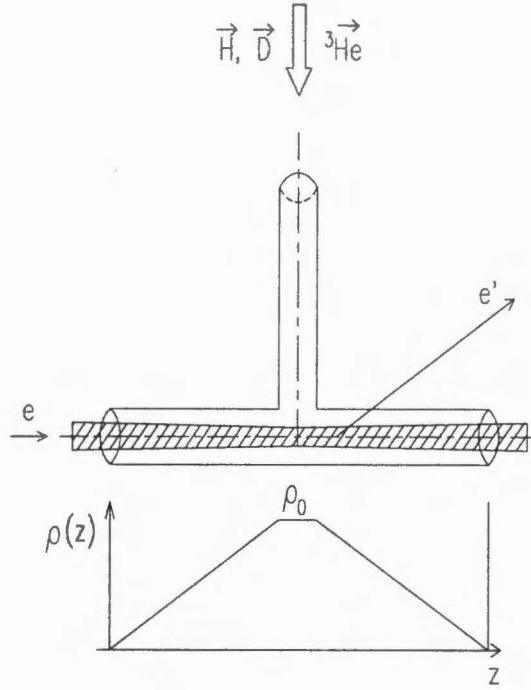
Figure 2.5: Schematic of the T-Shaped Storage Cell
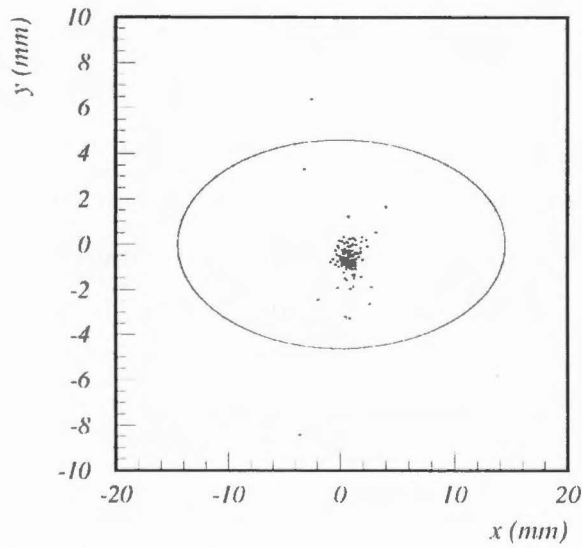
Figure 2.6: Vertex Distribution of Reconstructed Tracks in the Target

where T_0 is the revolution time around the ring (21 μs).

The total lifetime for the beam with the target gas is

$$\frac{1}{\tau_{total}} = \frac{1}{\tau_{gas}} + \frac{1}{\tau_{beam}}.$$ (2.7)

For τ_{beam} of 10 hours we are allowed a lifetime due to bremsstrahlung in the internal target (τ_{gas}) of 45 hours which corresponds to a target density of $10^{15} nucleons/cm^2$. The total lifetime in this case is 8 hours so the operation of the other experiments is not significantly affected.

The gas is stored in the target for a few milliseconds (~ 100 wall bounces) before leaving the storage cell and being pumped away. It is obviously important to limit the depolarization of the target during the time it is in the cell. A pair of large Helmholtz coils provide a uniform 10 G magnetic field in the target region with gradients of a few mG/cm in the cell with a smaller set of correction coils to cancel the residual gradient (~ 200 mG/cm) of the spectrometer magnet.

Wakefield suppressors [22] connect the target to the beam pipe. These perforated pipes reduce wake fields from the electron bunches and allow the target gas to exit toward the pumps.

The polarization obtainable in a flowing cell is lower than that obtainable in a sealed cell because the polarization is dependent on the residence time of the atoms in the laser light. Thus, it is desirable to minimize the flow rate by cooling the target as much as possible without depolarization.

The storage cell is cryogenically cooled to lower its conductance. The conductance of the storage cell depends on temperature so the flow rate of the cell can be decreased if the temperature is lowered. The density of the target is given by

$$\rho = \frac{Fl}{2C} \propto \frac{F}{\sqrt{T}}$$ (2.8)

where F is the flow rate; l is the length of the storage cell; C is the conductance and T the temperature. The depolarization of the ^3He due to wall bounces is small at temperatures > 20 K [29] due to helium's closed electronic shell. A series of tests were performed at Caltech with a deuteron beam $(^3\vec{H}e(d,p)^4He)$ [30] to determine
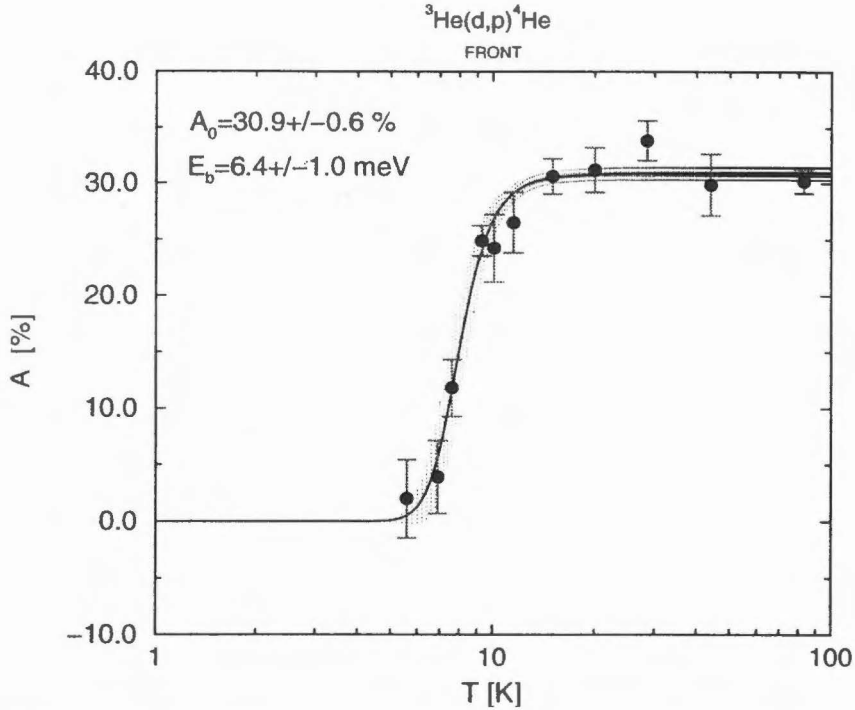
Figure 2.7: Temperature Dependence of ^3He Depolarization from Tests at Caltech

the temperature dependence of the polarization precisely. The results of analyzing power of this interaction (A_0) as a function of temperature are shown in Figure 2.7. The curve and parameters in the plot are a model of depolarization due to sticking to the cell walls [31]. It was determined that the target could be cryogenically cooled to 25 K with no significant depolarization due to wall sticking.

The absence of entrance and exit windows on the storage cell has significant benefits for the experiment. The external radiative corrections and smearing (discussed in Section 4.2.2), especially for the small x data, could be limited by reducing the amount of material for beam interactions before the target gas and interactions after scattering.

2.3.1 The Measurement of the Target Polarization

Two polarimeters were used to measure the target polarization. A pumping cell polarimeter (PCP) provides precise measurement of the polarization of the gas in the
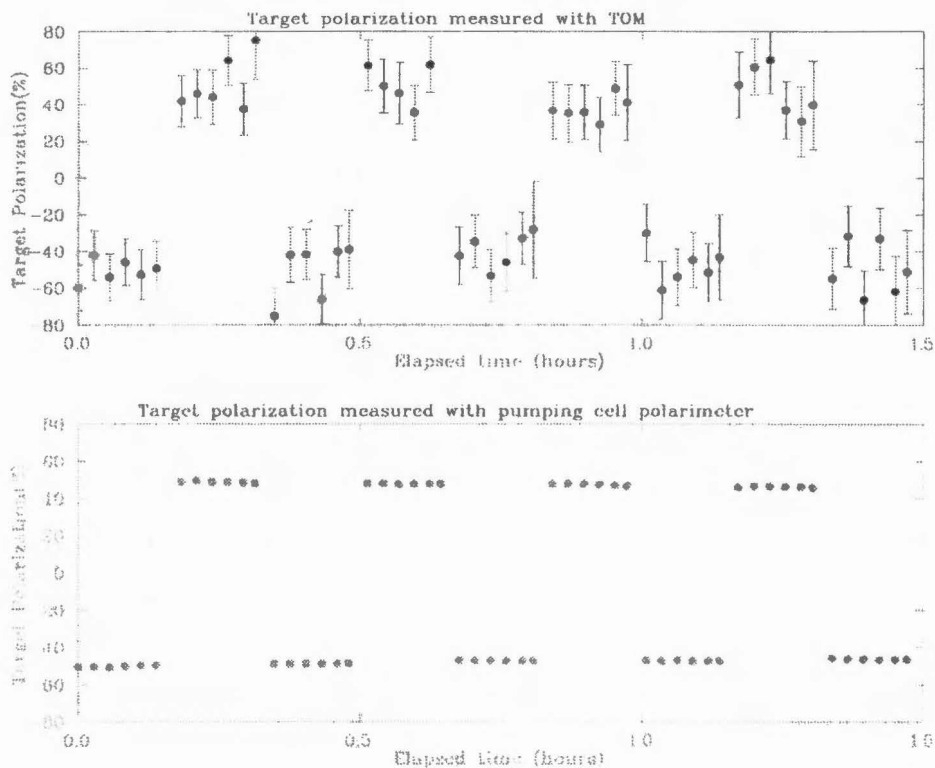
Figure 2.8: Polarization Measurements in the TOM and Pumping Cell Polarimeter

pumping cell. The PCP measures the circular polarization of 668 nm light emitted from the 3^1D_2 state. The nuclear polarization is mixed with the electronic polarization of this state by hyperfine interactions and the relation of circular polarization to nuclear polarization has been calibrated to within 5% with NMR measurements. [32]

The target optical monitor (TOM) measures the optical excitation of the target atoms in the storage cell by the beam. The $^4D_1$ excited state of helium has a long lifetime (37 ns) compared to the hyperfine mixing (1.5ns). Thus, for this level the nuclear polarization is transferred to the circularly polarized photons emitted by this level. The polarization of the atoms in the storage cell can be measured by analyzing the circular polarization asymmetry of this line. [33]

Figure 2.8 shows the polarizations measured by the TOM and PCP which suggest there is negligible loss of polarization between the pumping cell and the target.

The PCP measurement has a higher statistical accuracy and is used in the asymmetry analysis. The TOM provides a useful cross check of the polarization of the

target and is also used for the polarization measurement during a short period when the PCP was not working.

2.4 The HERMES Spectrometer

The HERMES spectrometer was designed for the measurements of inclusive and semi-inclusive asymmetries. To accommodate this goal the spectrometer has a large acceptance: up to $\pm$ 170 mrad in the horizontal direction and $\pm$ 140 mrad in the vertical direction. The storage ring beam lines divide the the spectrometer into two symmetric halves above and below the plane of the beam lines. The front detectors are placed as close to the beam line as possible and the minimum angular acceptance of the spectrometer is 40 mrad.

2.4.1 A General Overview

The HERMES spectrometer, which is shown in Figure 2.9, has been designed to provide a large acceptance for both inclusive and semi-inclusive physics. At the center of the spectrometer is a dipole magnet with a large acceptance both above and below the plane of the beam. The spectrometer is left-right symmetric for the simultaneous measurement of positive and negative charged leptons and hadrons.

Tracking chambers in front and behind the magnet give a good momentum resolution over a large acceptance for both the scattered positron and the hadronic final state.

A particle identification package containing a Cerenkov detector, transition radiation detector, preshower, and calorimeter are used to separate the positrons from the hadronic background and identify hadrons over a limited kinematic range.

2.4.2 Magnet

The HERMES experiment uses a single H-frame magnet to bend charged particles for momentum measurements. The magnet was designed to satisfy many constraints:[28]

- an $\int B \cdot dl = 1.3T \cdot m$ with less than a 10% variation within the geometric acceptance.

30

FIELD CLAMPS

MAGNET

DRIFT CHAMBERS

TRIGGER HODOSCOPE

PRESHOWER DETECTOR

³He PUMPING CELL

DRIFT CHAMBERS

VERTEX CHAMBERS

PROPORTIONAL CHAMBERS

LUMINOSITY MONITOR

STORAGE CELL

SEPTUM PLATE

TRD   CALORIMETER

ČERENKOV

FIG. 1.
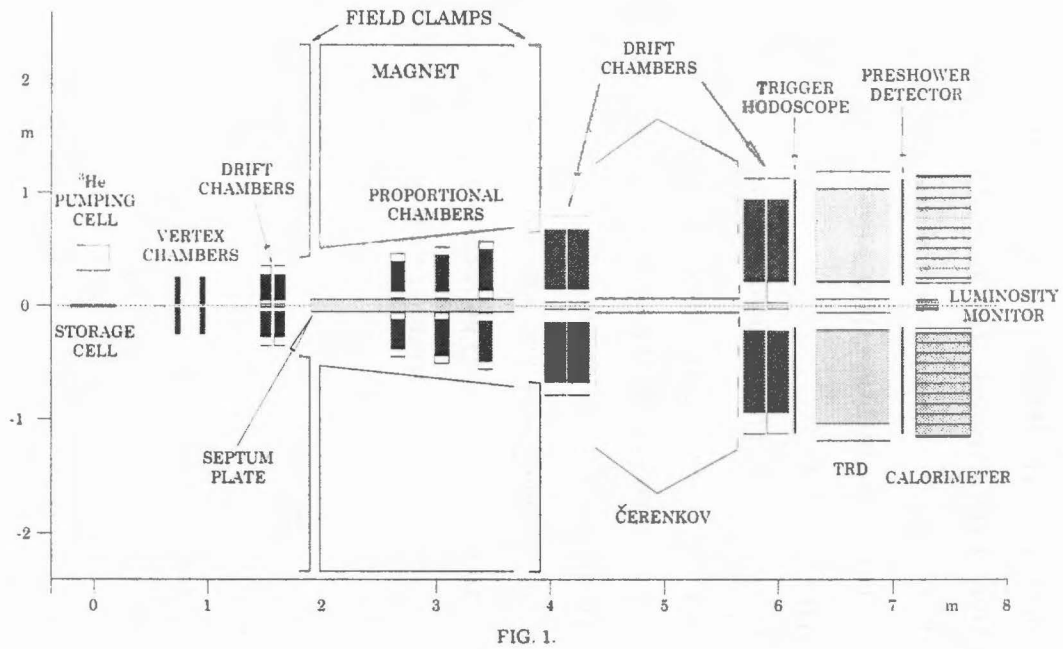
Figure 2.9: The HERMES Spectrometer

- small stray fields ($< .1T$) near the drift chambers

- minimal influence on the electron and proton beam optics

- a large acceptance to match the detector acceptance

- low power requirements (600 kW)

A magnet with field clamps in front and behind the magnet and an iron septum plate in the center plane meets all these constraints. The field clamps minimize the stray fields outside the magnet region. The septum plate surrounds the beam pipes, shields them from the magnetic field, and divides the spectrometer into two identical halves (top and bottom).

2.4.3 Tracking

For the 1995 data, the tracking was performed with drift chambers in front (FC) and behind (BC) the spectrometer magnet. The vertex chambers (VC) were not used in the tracking because of efficiency and hot wire problems. Separate track segments were formed in front and behind the magnet. These partial tracks were joined by requiring the front tracks segments to join the back segments at the plane in the center of the magnet bend. Figure 2.10 shows the front and back segments for an event with a high multiplicity. The average multiplicity was 1.5 tracks/event for events containing a DIS positron.

The HERMES reconstruction program (HRC) uses a pattern recognition algorithm [34] to look for groups of wire chamber hits which are consistent with tracks through the front or back region of the detector. The algorithm divides the detector in small subsections (bins) and replaces the position and resolution information of the chamber with a binary hit - no hit pattern. The pattern for the event is compared to a database of all possible patterns corresponding to tracks. A tree search [35] is used to improve the efficiency of this method. Rather than check all patterns at a fine resolution, the bins are ORed together to produce a lower resolution detector. The search is initially performed on a very low resolution detector (2 bins per plane). Figure 2.11 shows the start of a tree search for an event containing two tracks. As the resolution is increased
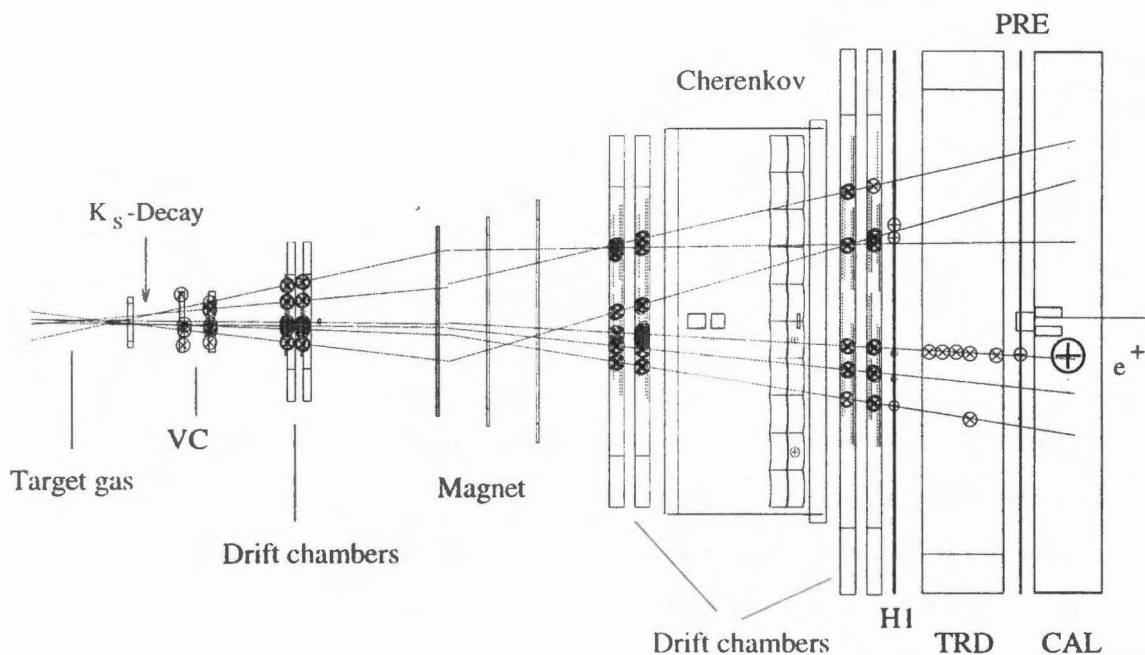
Figure 2.10: A High Track Multiplicity Event in the HERMES Spectrometer

only the patterns (sons) which are linked to patterns (fathers) which were matched at the next lowest resolution are checked. Because the magnetic field clamps contain most of the magnetic field to the magnet region, the tracks are essentially straight in the tracking regions. This limits the number of sons per father so the number of patterns checked in the tree search is significantly smaller than the number of patterns in the database at the final resolution.

Some triggers still required an exorbitant amount of computational effort to attempt to find tracks. These events have very high chamber multiplicities and produce large numbers of possible tracks which must be processed in the tree search algorithm. This can be understood in terms of the number of patterns generated by the extra noise hits. As the computer generates large numbers of possible patterns containing the noise at low resolution, the algorithm becomes a sequential search of all patterns at each level. (Dell'Orzo and Ristori [36] provide a good discussion of this and their simulation results are tabulated in table 2.1 for a 4 by 128 bin detector.)

A maximum multiplicity cut was implemented in the back chambers to eliminate these triggers. Events with large multiplicities consumed large amounts of processing

Noise (%)	Patterns Checked per Track Found
0	54
1	82
2	135
3	212
4 ˴	315
5	446

Table 2.1: Mean number of patterns compared per track as a function of noise (Monte Carlo simulation) for a 4 by 128 bin detector

time and did not have tracks reconstructing to the target. It was determined through careful study that these events were the result of stray 800 GeV/c protons starting showers in or behind the calorimeter which would fire the trigger and produce a large number of tracks behind the magnet. The parameter for the multiplicity cut was optimized by minimizing the time to reconstruct a series of runs with large proton background without reducing the number of tracks found.

The drift chambers have vertical wires for x position measurement and wires at $\pm 30°$ to the x wires (u and v). Three tree line searches are performed in the back region for the u, v, and x directions. A tree line is found if a valid pattern is matched at the final resolution of the tree search. All hits within a certain distance (called the road width in Table 2.2) of the found tree line are used to fit to the line in the u,v, or x plane. The tree lines found are joined to form partial tracks.

In the front region the tree search is performed in the u and v directions and the hits in the x region are matched to the x projection of the intersection of the u,v tree lines. This alteration of the tracking algorithm was dictated by the desire to include the VCs in the analysis. The VC x wires are not coplanar and cannot be used in the tree search.

The chambers have some inefficiencies; in fact, with the large number of chamber planes in the HERMES spectrometer, it is likely that at least one plane does not register a hit for any given track. The search algorithm is modified to accept tracks that match only partial patterns. The maximum number of planes without hits (called the missing hits per treeline) represents the number of bins which can be missing in a partial pattern match. The number of required hits is the total number
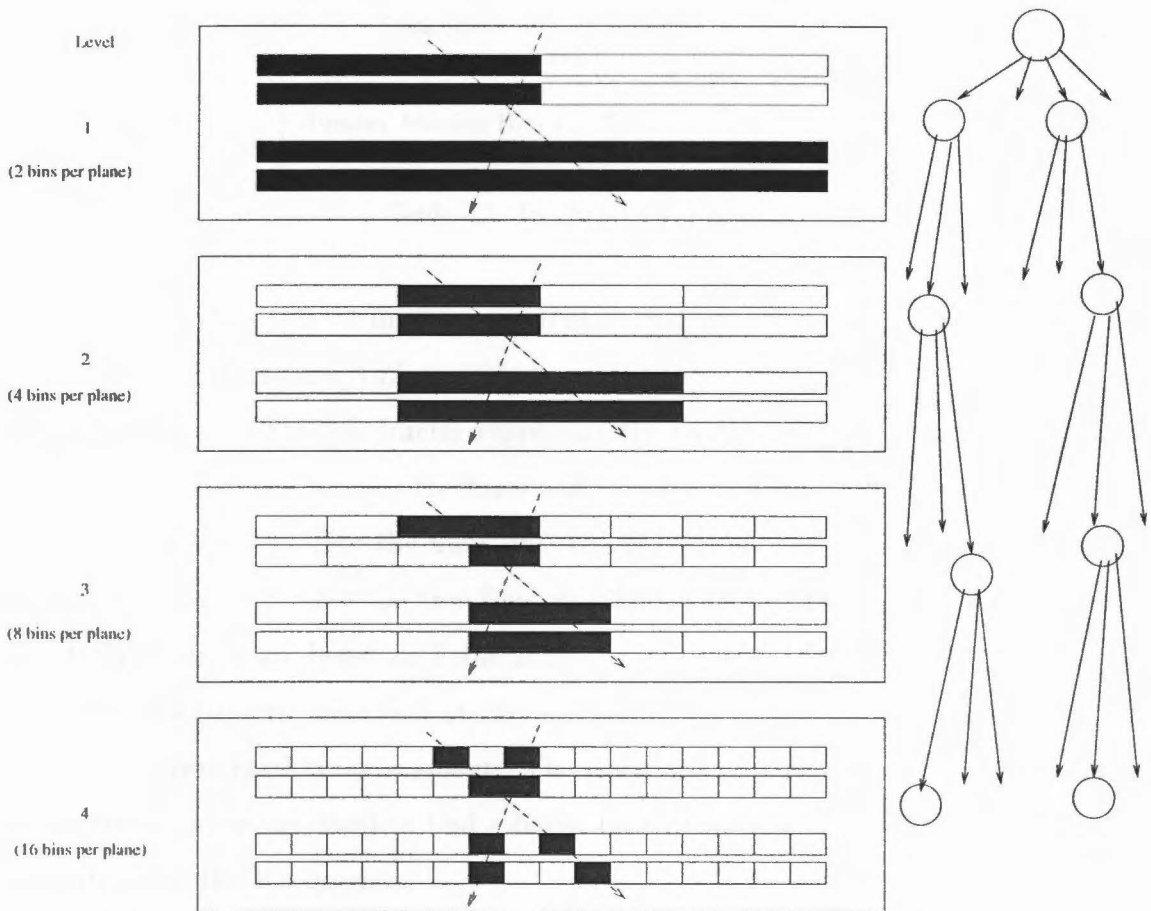
Figure 2.11: Track Finding with a Tree Search at Increasingly Higher Resolutions

Tree Search Parameter	Value
Road Width	1.3 bins
Front	
Number of Tree Levels	11
Final Resolution of Search	322 μm
Resolution of Chambers	300 μm
Number Missing Hits Per Tree Line	1
Number Missing Hits Per Tree Segment	3
Road Width (X Tree Line)	0.4 cm
Back	
Number of Tree Levels	12
Final Resolution of Search	469 μm
Resolution of Chambers	225 μm
Number Missing Hits Per Tree Line	3
Number Missing Hits Per Tree Segment	9
Maximum Multiplicity	22

Table 2.2: Tree Search Parameters

of planes per direction (4 in the front region, 8 in the back) minus the missing hits. An additional parameter (missing hits per tree segment) can place a more restrictive track finding cut. This parameter represents the total number of missing hits allowed in the three treelines (or two treelines and x projection in the front) which match to form a track segment. For the final 1995 tracking, this parameter did not represent a more restrictive cut than the tree line cut. The standard tree search parameters for the 1995 analysis are listed in Table 2.2.

Any valid pattern identified at the maximum resolution of the tree search is used to define a potential track segment. The positions and resolutions of the chambers along the segment are used to find a linear best fit for the track. A χ^2 test is used to identify valid track segments.

If multiple track segments use the same hits, the segment with the best χ^2 is considered the valid track segment and others are rejected.

The track segments found in the front and back are matched at the center of the magnet. This matching is referred to as 'bridging'. The track segments are projected to the center of bend of the magnet and required to match within a maximum distance in x and y and slope in y. (The magnet primarily bends in the x direction and the difference in the x slope is used to determine the momentum of a track.) The bridging parameters are listed in Table 2.3.

Allowed Pattern (Contained in database of valid patterns)

Illegal Pattern (Not in database)

Database contains straight line projections through 100% efficiency chambers
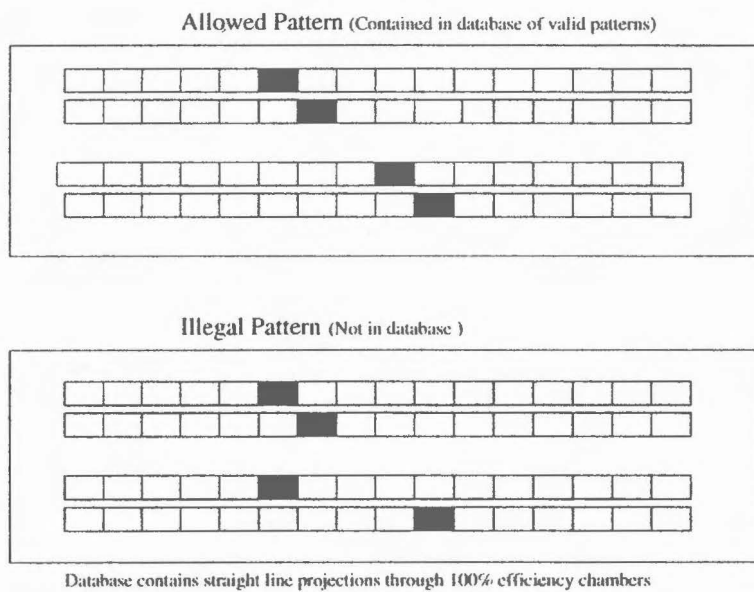
Figure 2.12: Pattern Matching Algorithm

Bridging Parameter	Value
X match	5 cm
Y match	5 cm
y slope match	0.050 (dy/dz)

Table 2.3: Bridging Parameters
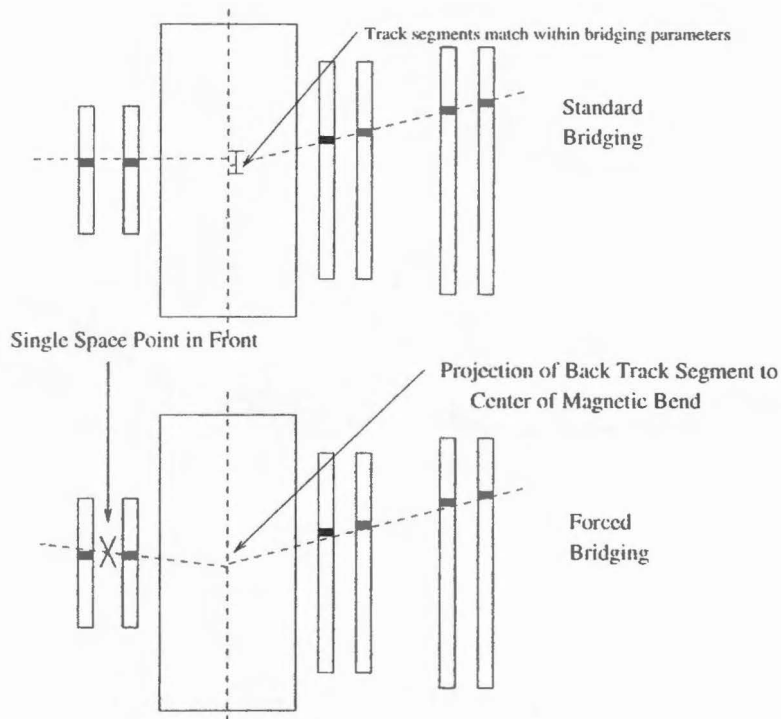
Figure 2.13: Improving the Momentum Measurement Through Forced Bridging

The momentum of a track is calculated by interpolating a lookup table in slope and difference of the front and back slopes in the magnet. The uncertainty in the angle in front of the magnet greatly reduced the resolution of the spectrometer.

The vertex chambers are not used in the 1995 analysis because problems with hot wires and efficiency limited the track reconstruction with the vertex chambers. As a result the HERMES tracking is significantly better behind the magnet than in front. The four back chambers can accurately define a position and slope of a track segment. The two front chambers are designed to function in conjunction with the vertex chambers. They are too close together to accurately define a slope. (The BCs have a lever arm of 175 cm while the FCs have a lever arm of only 12 cm.)

To improve the momentum measurement, the track information from the BCs was used to recalculate the slope in the front region. This is referred to as forced bridging. Three points are required to determine the momentum of a particle bent in the spectrometer magnetic field. The higher resolution projection to the center of the magnet from the back chambers is used to define one of the points. The front
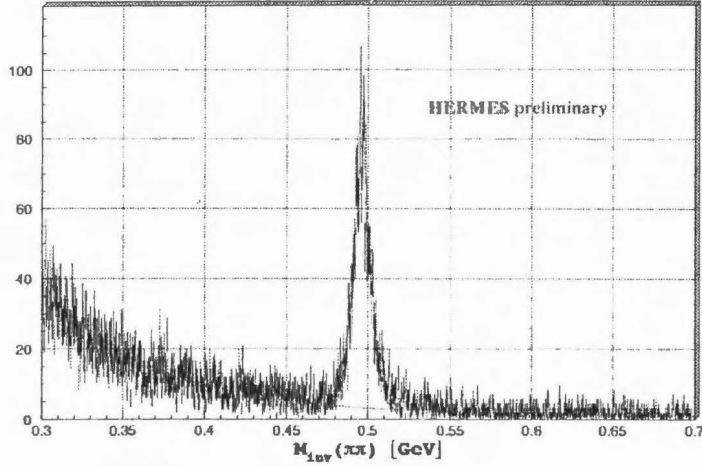
Figure 2.14: K_s Mass Reconstruction

chambers are used to define a single space point which is forced to match to the projection of the BC track segment in the plane of the center of the magnet bend. This method is shown in Figure 2.13.

A resolution of $\Delta P/P$ of 1.75% was observed for the spectrometer. (Monte Carlo simulations suggest a resolution of $\Delta P/P$ of 0.5% can be obtained with the vertex chambers. [37]) Improvements of the vertex chambers should improve the tracking resolution for the HERMES data taken in 1996.

The momentum resolution of the spectrometer can be seen in the reconstructed invariant mass of K_s decays shown in Figure 2.14.

$$K_s \rightarrow \pi^+\pi^- \tag{2.9}$$

The momentum resolution of the spectrometer was deduced from the width of the K_s peak. The invariant mass for the two pions is calculated from their momenta and opening angle.

$$M^2 \simeq 2E_1 E_2 (1 - Cos\Theta). \tag{2.10}$$

The resolution of the K_s peak can be expressed in terms of the momentum resolution of the reconstructed pions as:

$$\frac{\delta M}{M} = \frac{1}{\sqrt{2}} \frac{\delta E}{E}.$$

(2.11)

The observed K_s width of 1.2% is consistent with a momentum resolution of 1.75% which was determined from Monte Carlo reconstruction without the VCs.

2.4.4 Alignment

An initial survey was performed to align all detectors in the spectrometer at installation. Two methods are used to monitor the alignment of the tracking chambers in the spectrometer. Partial tracks either in front or behind the magnet were initially used to determine the relative alignment of the front and back drift chambers and monitor any changes.

The FCs and BCs were internally aligned by minimizing the residuals within each set of chambers for partial tracks. Data with the spectrometer magnet off was used to align the FCs and BCs with the target. Without the magnetic on, the tracks from the target can be reconstructed from the BCs through the FCs back to the target. The residuals for the chamber planes were again minimized for the full tracking system. The magnet-on residuals are checked throughout the experiment to check for relative movement of the chamber planes.

A laser alignment system is designed to monitor continuously the alignment of the tracking detectors. Two Fresnel zone plates are mounted on each detector. The interference patterns from a laser incident on the zone plates are recorded with a CCD camera. Shifts in the detector position can be observed as shifts in the focal pattern at the camera. Although the calorimeter frame is separate from the structural supports on the rest of the spectrometer, the alignment systems checks for any changes caused by vibrations due to the calorimeter movement.

2.4.5 Efficiency

The efficiency of the tracking detectors was carefully monitored with a program (ACE) which uses the tracks found in HRC to calculate the efficiency for each plane of chambers and an overall efficiency for the front and back regions. The efficiency for
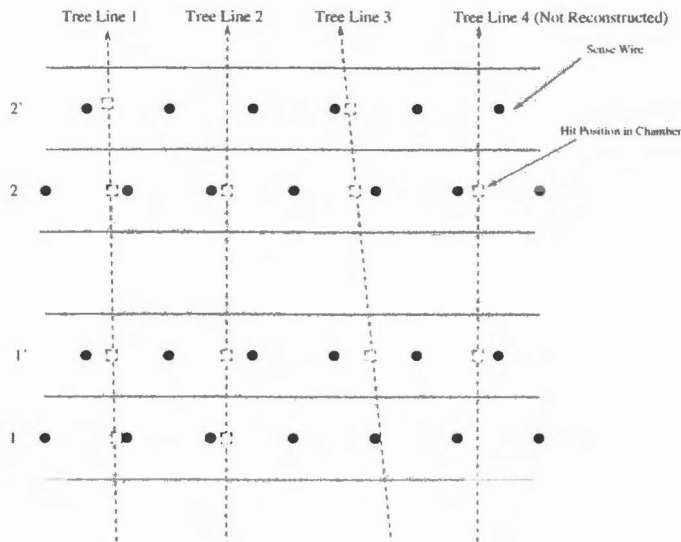
Figure 2.15: The Chamber Efficiency Algorithm

a given plane is defined by:

$$\epsilon = \frac{\text{number of tracks which have a hit in the specified region of the detector plane}}{\text{number of tracks}}$$

(2.12)

HERMES does not have the luxury of auxiliary tracking detectors which can be used to define a sample of tracks. The hodoscopes provide only crude resolution in the x direction and there is no information on the possible track position in front of the magnet without the tracking chambers. An attempt has been made to select subsamples of tracks which do not introduce a bias in the calculation of the efficiency.

Track Subsamples

Each plane of chambers has its own subsample of tracks used to calculate an efficiency. This subsample consists of all tracks for which the information in that plane is redundant. That is, it is believed that the tracking algorithm would have found the track whether this particular plane did or did not fire.

For the front region this can be simply defined; a u,v,or x plane is redundant if there is a hit within the road width for this track in each of the other three planes in the same direction. In Figure 2.15 the tracks containing tree lines like 1 and 2 would

Typical Chamber Efficiency	
Front	89%
Back	93%
Typical Total Partial Track Efficiency	
Front	88%
Back	99%

Table 2.4: Typical ACE Efficiencies

be used to calculate the efficiency of plane 2'. It is important to exclude tree line 3 to avoid biasing the efficiency upward. Tree line 4 is rejected by the tree search so it cannot be considered in the efficiency calculations.

The determination is slightly more complicated in the back region because certain combinations of planes such as three missing planes in BC1 and 2 are forbidden. There is still an unambiguous determination of when a plane is redundant for a tree line.

There may still be a bias from the definition of tree lines. Using the information from the plane changes the track slope and position at center of the magnet. One could consider biases caused by a larger fraction of the tracks with four hits per tree line successfully bridging than tracks with three hits per tree line. Initial studies suggest that these biases are small [38].

It would be computationally daunting to attempt to perform the tracking repeatedly neglecting chambers. It would require 36 times the CPU to perform the tracking neglecting one plane at a time. In order to reduce this time and determine tracking efficiencies on the burst level, only one pass of the tracking was performed and the efficiency analysis was performed on the tracks found using the chambers.

ACE sorts the hits for each chamber that is required and counts the tracks where the hit is required or not required. The efficiencies are a crucial part of the determination of whether or not the data is suitable for asymmetry analysis. The efficiencies determined are functions of the high voltage, temperature, atmospheric pressure, chamber gas composition, and TDC threshold. The efficiencies varied considerably from fill to fill as is shown in Figure 2.16. Each set of points represents one fill of the ring with positrons. Typical values for the efficiencies are shown in Table 2.4. The
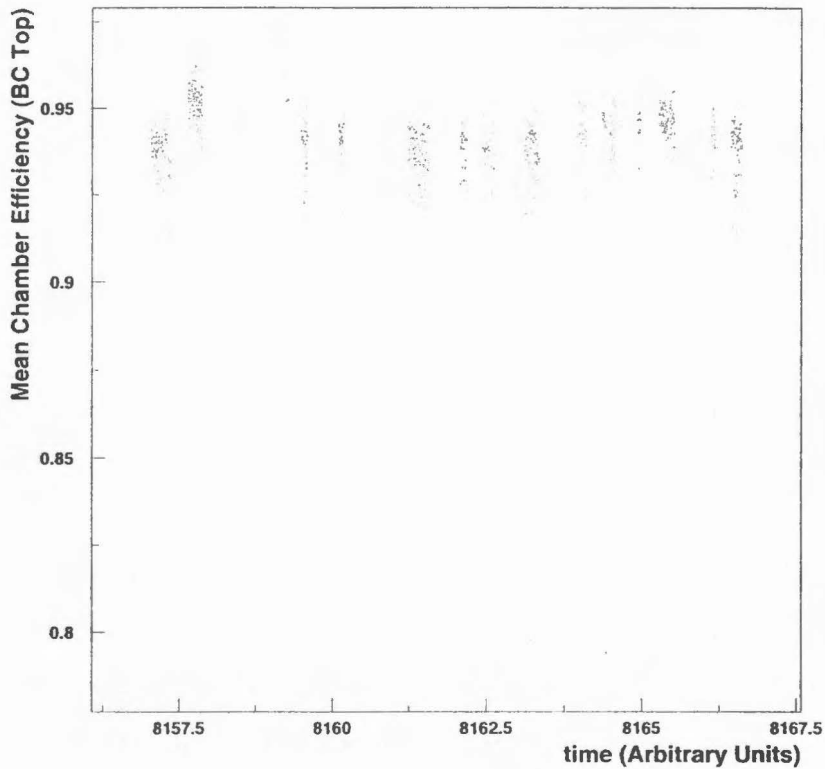
Figure 2.16: Time Dependence of the Chamber Efficiency for a Series of Fills

ACE efficiencies were used to monitor any of these effects versus time and ensure the chambers were working correctly and stably during the periods used in the asymmetry analysis. The efficiencies were not used to correct the event rate so small biases in the calculated efficiencies are not significant.

2.4.6 Particle Identification

A set of four detectors (preshower, calorimeter, Cerenkov and TRD) were used for particle identification at HERMES. The particle identification methods, efficiencies, and contaminations will be discussed in chapter 4. The location of each detector in the spectrometer and the physics involved in particle identification is described below.

2.4.7 Hodoscopes

The HERMES trigger hodoscopes were designed and built at Caltech. Their design and testing will be discussed in detail in Appendix A. Two hodoscope planes are installed in the spectrometer and provide fast signals for the first level trigger.

Each hodoscope is composed of 84 vertical scintillator paddles (42 each top and bottom). The paddles overlap to cover completely the HERMES acceptance. The scintillator provides a large response (200 p.e.) for minimum ionizing particles so the paddles have a highly efficient response at thresholds well above the single photo electron level with very little noise. The photomultiplier tubes (PMTs) (Thorn EMI 9954) were chosen to give a fast, linear response with a short recovery time. This allows a fast trigger response and good energy reconstruction even at high trigger rates.

The first plane consists of two rows of staggered scintillator paddles measuring 9.3 X 91 X 1 cm^3 (2% radiation length) of BC-412 scintillator. These 1 cm thick paddles minimize the electromagnetic interactions but provide a large signal to minimize the trigger background. This hodoscope plane is designed to discriminate photons which will shower in the other trigger detectors (Section 2.4.13).

The second plane is operated as a preshower detector. A lead sheet (1.1 cm = 2 radiation lengths) called the preshower starts electromagnetic showers before the preshower scintillator. Figure 2.17 shows the second hodoscope with the preshower as it was installed. The hadronic interaction length is much longer than the EM radiation length and the difference in energy deposited in the scintillator for hadrons and positrons (roughly proportional to the number of charged particles in the shower after two radiation lengths) can be used for hadron/positron separation.

2.4.8 Calorimeter

A lead glass calorimeter is used to measure the energy of the positrons. The calorimeter is composed of 840 9.0 x 9.0 x 50 cm^3 blocks of radiation resistant F101 lead glass as shown in Figure 2.19. The lead glass was Cerium doped to improve its radiation hardness. This increases the attenuation of light in the lead glass but will protect the
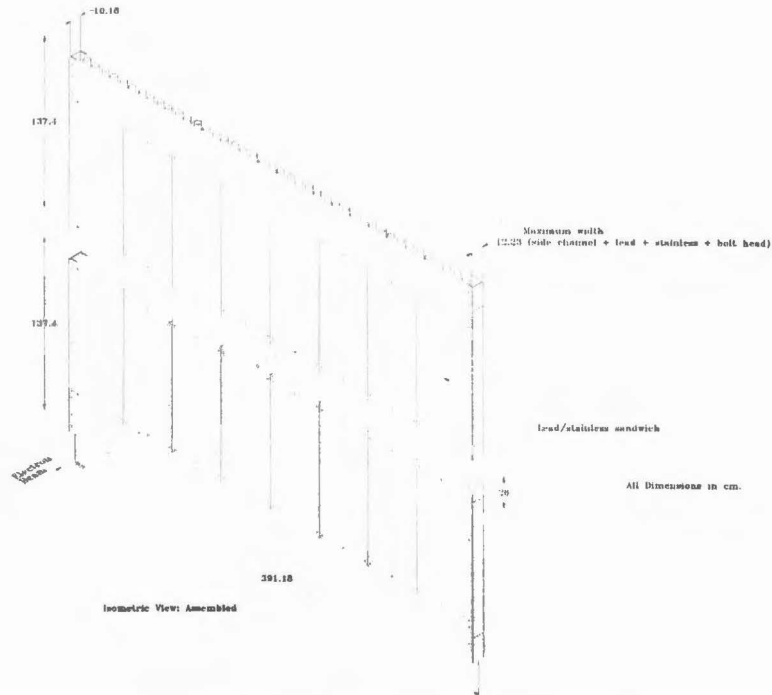
Figure 2.17: Isometric View of the Hodoscope

Density (g/cm^3)	3.86
X_0 (g/cm^2)	10.73
R_M (cm)	3.28
E_c (MeV)	17.97
λ (g/cm^2)	137.7

Table 2.5: Physical Properties of F101 Lead Glass

glass from attenuation length changes due to radiation damage.

Each block is wrapped in a layer of reflective mylar surrounded by a layer of opaque tedlar which ensures light isolation between the blocks. The calorimeter measures the Cerenkov light from the shower of particles produced by the Bremsstrahlung of the high energy positron incident in the calorimeter.

The energy deposition of electromagnetic and hadronic showers in the calorimeter can be described in terms of several parameters. The most significant of these are the radiation length (X_0), the Moliere radius (ρ_m), the critical energy (E_c), and the hadronic interaction length (λ).

The depth required to contain a shower has a logarithmic dependence on the

incident energy and for a 27.5 GeV/c shower is given by: [39]

$$L(98\%) \simeq 20X_0. \tag{2.13}$$

L(98%) is the length needed to absorb 98% of the energy of incident particle. The calorimeter is thick enough (18 radiation lengths) to stop the scattered positrons after the showers begin in the preshower (2 radiation lengths). An energy measurement is made from the Cerenkov light emitted by the shower of particles emitted through Bremsstrahlung and pair production as the positron stops.

E_c is the energy at which ionization energy loss equal the loss from Bremsstrahlung. Low energy particles ($E \simeq E_c$) are quickly stopped by ionization losses. The critical energy can be considered to be the end of shower development. At energies above the critical energy, a tree of progressively lower energy particles develops in the calorimeter. Showering particles below the ionization energy are quickly stopped. The total track length of the showering particles in the calorimeter is estimated to be proportional to E/E_c. Lead glass has a high index of refraction (n=1.65) and electrons and positrons produce Cerenkov radiation over their entire track length. The number of Cerenkov photons is therefore proportional to track length and also the incident energy.

It is necessary to select a region of blocks large enough to contain the transverse distribution of the shower. The transverse distribution is dominated by multiple scattering for the lower energy particles. The Moliere radius (ρ_m) describes the average lateral deflection of low energy electrons in one radiation length. The lateral dependence of the high energy shower is given by the typical angle for bremsstrahlung emission ($\Theta_{brems} = m/E$). The transverse distribution can be described as a central core from bremsstrahlung with a halo due to multiple scattering. For the purposes of energy measurement, the shower occurs within a cylinder of radius 2 ρ_m.

For the HERMES calorimeter, 2 ρ_m is 6.5 cm. To ensure the selected cluster contained the full energy of an electromagnetic shower, three by three clusters of blocks were chosen. Even if a track enters the calorimeter near the boundary between two blocks, the full energy should be contained in a cluster centered on either of the

blocks.

The resolution of calorimeters is described with two terms; a term due to photon statistics and an intrinsic resolution mostly due to shower leakage and miscalibration. The HERMES calorimeter clusters have a resolution [40] of

$$\sigma(E)/E[\%] = (5.1 \pm 1.1)/\sqrt{E[GeV]} + (1.5 \pm 0.5). \qquad (2.14)$$

Hadronic showers have a more complicated distribution because they combine small ionization losses with large energy depositions due to hadronic interactions. These hadronic interactions produce large numbers of pion and nucleon secondaries (including many π^0's which decay electromagnetically). Similar to the radiation length, the hadronic interaction length (λ) describes a characteristic scale for hadronic interactions. The calorimeter's length was minimized to reduce the probability of hadronic interactions. Hadronic showers are also much wider than electromagnetic showers. The secondaries in a hadronic shower have significant $< p_T >$ and produce a wider deposition of energy. As a result, a significant portion of the incident energy of hadrons can be carried out of the calorimeter by nucleons and charged pions or deposited outside the shower cluster.

Figure 2.18 shows a GEANT 3.12 [41] Monte Carlo spectra for three types of particles showering in the calorimeter. The ratio of energy deposited to momentum is normalized to 1 for the electrons. The μ peak is the energy deposition due to ionization for a particle traversing the calorimeter. The π distribution contains a broad peak due to hadronic showers with a minimum ionizing peak due to π's which do not have a large hadronic interaction in the calorimeter. The difference in the fraction of energy contained in a three by three cluster of blocks for the two shower types is used to distinguish positrons from hadrons.

The calorimeter is mounted on a movable platform. It moves 50 cm away from the beam to protect against radiation damage during dump and injection. To monitor possible radiation damage, four additional lead glass counters were mounted near the proton and electron beam pipes. These blocks were made of a much more radiation sensitive material than the calorimeter and there was no evidence of radiation damage
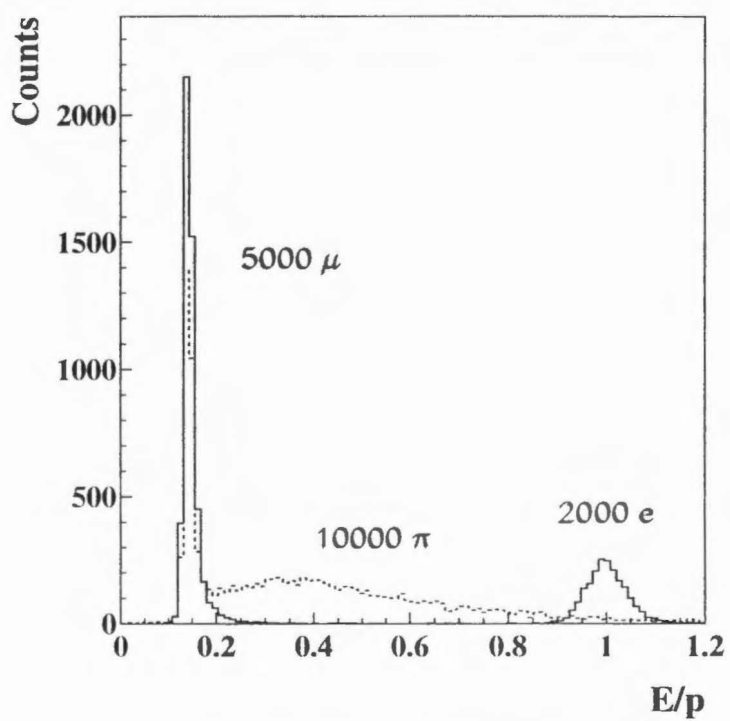
Figure 2.18: Monte Carlo Calorimeter Response for 5 GeV/c Particles
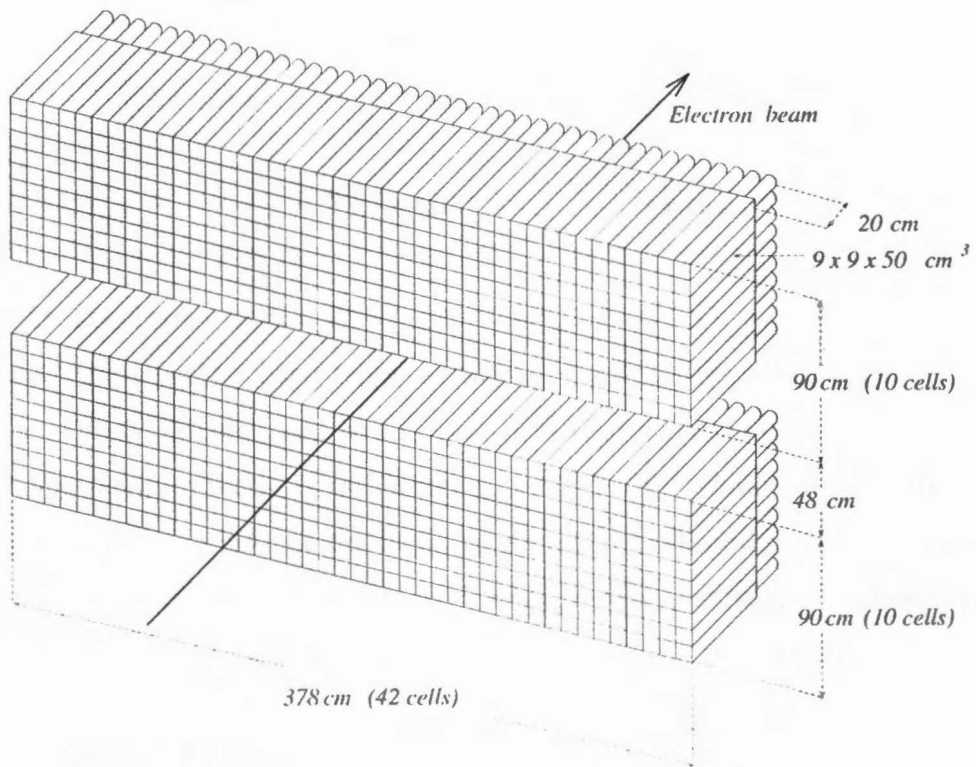
Figure 2.19: Isometric View of the Calorimeter
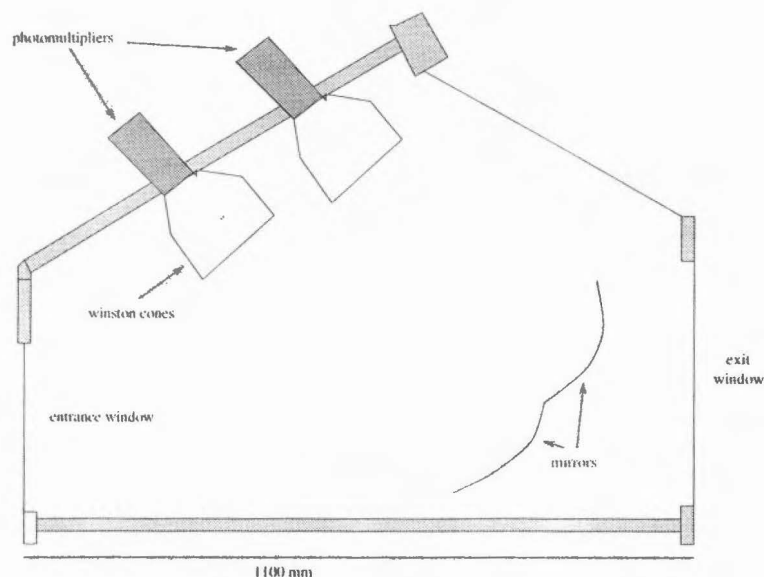
Figure 2.20: HERMES Cerenkov Detector

in these blocks during 1995.

Because the HERMES spectrometer has an open design, radiative photons from the target vertex are observed in the spectrometer. This photon distribution peaks along the momentum vector of the emitting positron. If the momentum is above about 10 GeV these photons are not resolved, but summed in the energy of the calorimeter. This can result in an upward bias in the E/p ratio because the spectrometer does not bend the high momentum positron enough to resolve the two clusters.

2.4.9 Cerenkov Detector

A threshold Cerenkov detector was used to distinguish particles which have a velocity above the local velocity of light in the medium. The Cerenkov effect is well described in numerous texts [42].

The HERMES Cerenkov detector (Figure 2.20) consists of two identical threshold detectors, above and below the beam line. The radiator in 1995 was nitrogen gas at atmospheric pressure and room temperature. The Cerenkov light is collected in each counter by a set of 20 mirrors and photomultipliers arranged in two rows of ten in each detector as shown in Figure 2.20. The entrance and exit windows are made of

Particle	Mass (GeV/c)	Momentum Threshold (GeV/c)	
		Nitrogen	C_4F_{10}
electron	0.0005	0.02	0.01
pion	0.139	5.72	2.76
kaon	0.493	20.23	9.78
proton	0.938	38.42	18.61

Table 2.6: Momentum Threshold of Cerenkov Detector

tedlar/mylar.

Gas filled Cerenkov detectors are especially useful in high energy experiments because their low index of refraction allows the separation of particles with high β. For nitrogen gas at one atmosphere pressure, this gave an index of refraction, n, of 1.000298 at 589 nm [43]. In 1995, the Cerenkov was used primarily for electron/hadron separation and this was the primary motivation for the use of nitrogen gas. The detector must have large, thin entrance and exit windows to cover the acceptance behind the magnet and minimize the scattered particle's interactions before traversing the second set of back drift chambers. Because of these windows, the Cerenkov cannot support a large pressure differential with the East Hall and must be near the local atmospheric pressure. The differential pressure with the atmosphere was slightly positive to protect the purity of the nitrogen gas from contamination by room air.

The momentum thresholds for Cerenkov light emission is determined by the equation.

$$P_t = \frac{m}{\sqrt{n^2 - 1}} \tag{2.15}$$

The Cerenkov thresholds for various particles in nitrogen gas at one atmosphere are listed in table 2.6. The Cerenkov detector was used to improve the hadron rejection for particles with a momentum below 6 GeV/c. Below this momentum, hadrons do not produce significant Cerenkov radiation in nitrogen gas at atmospheric pressure. Other gases can be used for different purposes. The Cerenkov was filled with C_4F_{10} (n=1.001270) [43] to perform π identification over a larger momentum range in 1996.

The second main issue for the performance of a Cerenkov detector is the number of photoelectrons detected in the photomultiplier tubes. The number of Cerenkov

photons is proportional to the length of the radiator so a large radiator is required to produce a large signal. The HERMES Cerenkov faced serious problems because the area behind the magnet is extremely crowded and scattered particles enter the Cerenkov at many different angles. The length of the radiator for the HERMES Cerenkov is 90 cm. The average number of photoelectrons for a $\beta = 1$ particle ($n_{pe}^{e^+}$) was 3.0.

The response for heavier particles is given by:

$$n_{pe} = n_{pe}^{e^+}(1 - (\frac{P_t}{P})^2)\Theta(P - P_t) \tag{2.16}$$

The largest component of the hadron background is expected to be pions and the $< n_{pe} >$ versus momentum is shown is Figure 2.21. The mean response as a function of momentum shows the correct threshold behavior although the observed number of photoelectrons is lower than would be expected for pions alone. This is not surprising since the hadron sample is composed of both pions and heavier hadrons which will not emit Cerenkov radiation.

The non-zero mean signal for hadrons below the Cerenkov threshold for pions is caused by scintillation in the Cerenkov gas and knock on electrons. The single photo electron peak due to these processes can be seen in Figure 2.22.

A series of LEDs were used to calibrate the Cerenkov. A separate calibration trigger fired the LEDs at 1 Hz and recorded the gain at the single photoelectron peak for each tube.

2.4.10 Transition Radiation Detector

Transition radiation (TR) is produced when a relativistic particle crosses the boundary between two media with different dielectric constants. This phenomena can be understood classically from Maxwell's equations much like Cerenkov radiation [44].

The emission of transition radiation (TR) from a single surface is linear in the Lorentz factor ($\gamma = E/m$). Ideally, a TR radiator consists of a series of foils at a regular spacing to ensure constructive interference of the generated TR at each boundary followed by an X-ray detector. It would be impossible to maintain the
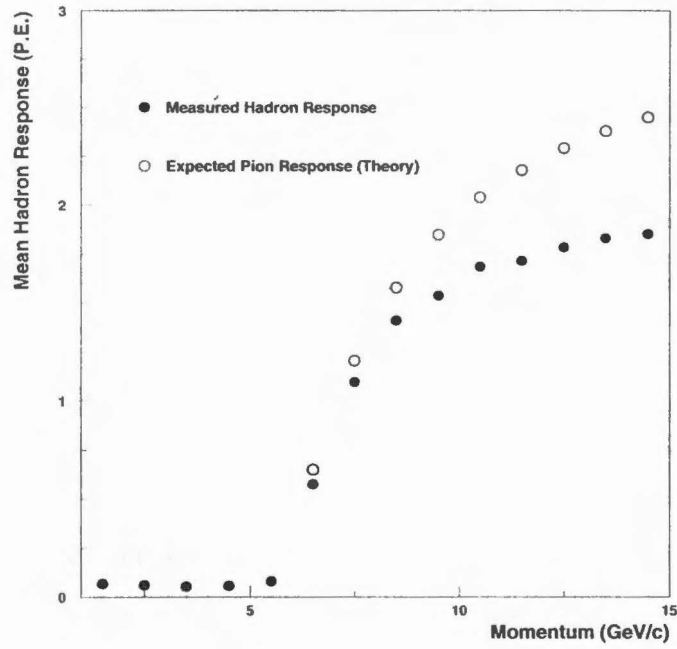
Figure 2.21: Cerenkov Response for Hadrons
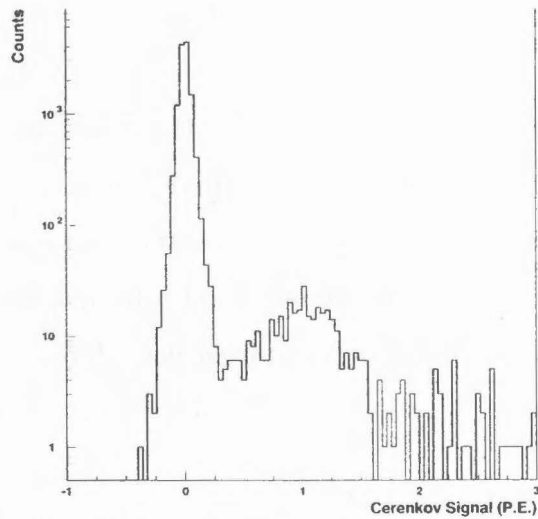
Figure 2.22: Cerenkov Response of Hadrons Below the Cerenkov Threshold

Momentum (GeV/c)	Lorentz factor (γ)	
	Positron	Pion
5	9785	36
25	48923	180

Table 2.7: Lorentz Factor for Positrons and Pions

spacing for a large TRD such as the one at HERMES. Instead, a random matrix of fibers is used to provide a large number of interfaces. In this case, the TR is viewed as forming in a "formation zone." The effects of interference cause the energy flux to saturate after the formation zone. Various configurations were tested to find a fiber matrix with a good yield of TR.

Only high energy electrons and positrons have a high enough γ to produce significant TR (see Table 2.7). Hadrons produce an energy deposition consistent with a minimum ionizing particle crossing the proportional chamber.

The HERMES TRD consists of six identical modules above and below the plane of the beam. Each module contains a radiator followed by a Xe/CH_4 filled proportional chamber as shown in Figure 2.23. A 6.5cm thick random matrix of (10-30 μm radius) polypropylene fibers is used as a radiator. The transition radiation produced by particles with high energies is typically in the X-ray region. These X-rays are detected in 2.54 cm thick proportional counters with 12.7 mm wire spacing. Xe/CH_4 (90:10) was chosen as a gas mixture for the TRD because Xe has a very high X-ray absorption cross section (i.e., high Z).

A significant background for the TRD is $\delta -$ ray production in the proportional chambers. The $\delta -$ rays are preferentially emitted perpendicular to the particle. However, the $\delta -$ rays which are emitted nearly parallel to a wire can be trapped by the wire's electric field and deposit a large amount of energy in a single module. A truncated mean of the six modules was used in the analysis on the TRD signals to improve the rejection of hadrons which emit $\delta -$ ray.

$$\text{Truncated Mean} = \frac{\Sigma_{i=1}^{6} TRD_i - max(TRD_i)}{5}. \tag{2.17}$$

The truncated mean is less sensitive than the sum of the modules to a large energy
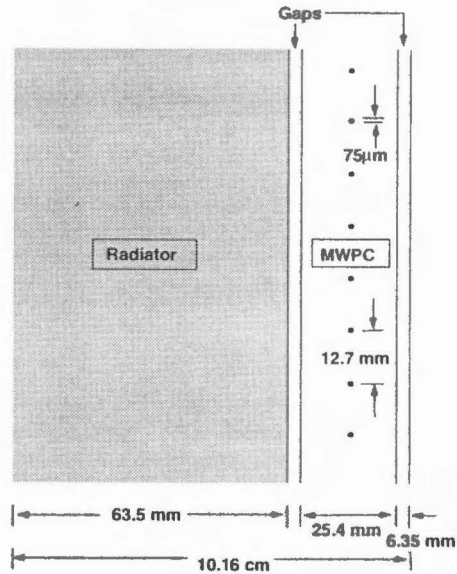
Figure 2.23: TRD Module

deposition in a single module and can provide 100:1 hadron rejection at positron efficiencies > 98%.

2.4.11 Luminosity Monitor

The luminosity monitor detects the Bhabha scattering of the positron beam from the electrons in the target atoms [45]. Two calorimeters near the beam pipe detect scattered leptons at angles expected for symmetric Bhabha scattering. The luminosity is the rate of coincidences with energies greater than 8 GeV in each calorimeter. The calorimeters are made from 12 (22 by 22 by 200) mm^3 NaBi(WO$_4$)$_2$ crystals. NaBi(WO$_4$)$_2$ was chosen for its high resistance to radiation damage.

The calorimeters are placed close (30 mm) to the beam pipe to look for Bhabha scattered positrons and electrons with energies between 8 and 20 GeV/c (Figure 2.25). There is also a significant singles rate with a large energy deposition in a single calorimeter. Coincidence rates vary between 40 and 200 Hz at a nominal target density of 10^{15} nucleons/cm^2 and beam currents between 10 and 35 mA.

Precise knowledge of the luminosity is not necessary for the asymmetry measurements. Only the ratio of the luminosities for the two spin states is necessary. Cal-
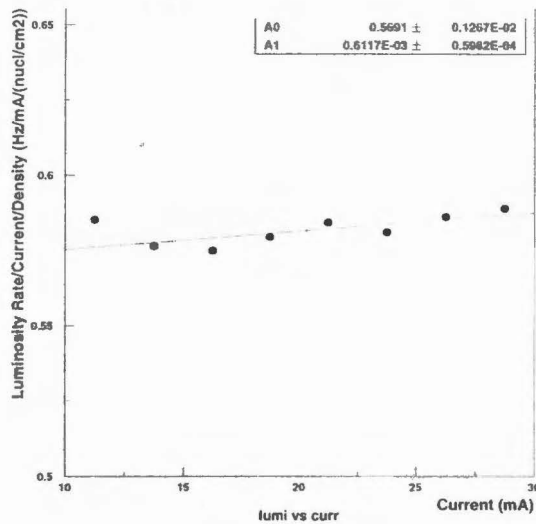
Figure 2.24: Current Dependence of the Luminosity

culations of the absolute luminosity are complicated because many Bhabha scattered leptons travel through the thin walled beam pipe and septum plate. The energy degradation in these media is significant and very sensitive to scattering angle.

The luminosity monitor has very small backgrounds. There is no rate is the luminosity monitor when the beams are circulating the rings but there is no gas in the target. Figure 2.24 shows that the luminosity rate is very well described as proportional to the product of the current and target density. A term proportional to (current times target density)^2 would be expected for random coincidences in the luminosity monitor. The random coincidences represent less than 1% of the rate in the luminosity monitor and varies slowly on the time scale of the target polarization flip.

2.4.12 Gain Monitoring System

Laser generated light signals monitor the gains of the preshower, calorimeter, and luminosity monitor. A 500 nm dye laser is used as a light source for the gain monitoring system. Fiber optic cables are used to carry the light to the second hodoscope, calorimeter, and luminosity monitor. A rotating filter wheel attenuates the laser
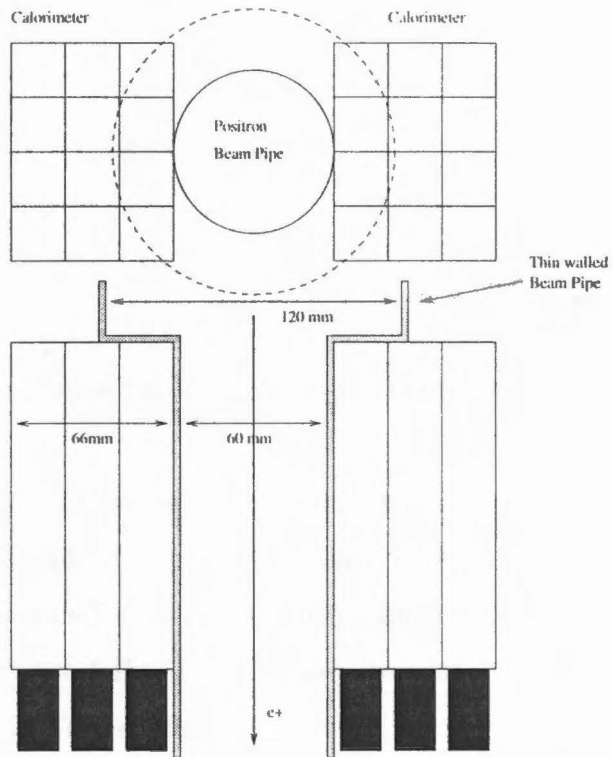
Figure 2.25: Luminosity Monitor
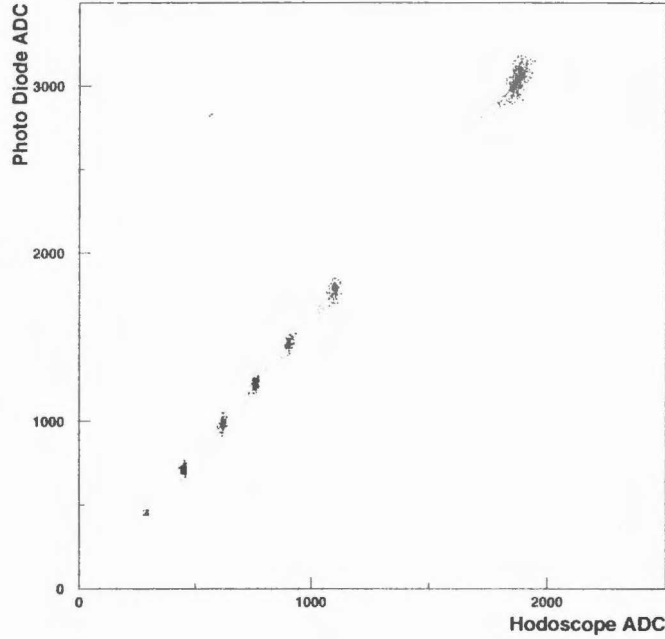
Figure 2.26: Gain Monitoring Data for One Run

pulses and provides light pulses of six different amplitudes to the detectors as well as triggers with no light. The gain is measured relative to a group of photodiodes. Photodiodes were chosen for their long term gain stability.

The laser pulses at ~ 1 Hz. The gain monitor data for a single hodoscope paddle and run are shown in Figure 2.26.

2.4.13   Trigger

The main HERMES physics trigger is a coincidence of the bunch crossing and a series of detectors which indicate a potential DIS positron in the spectrometer.

$$Trigger \equiv [(H1_{top} \cap H2_{top} \cap CAL_{top}) \cup (H1_{bot} \cap H2_{bot} \cap CAL_{bot})] \cap HC \qquad (2.18)$$

The components in the trigger are:

- HC = the bunch crossing time provided by the accelerator RF system ('HERA Clock')

- H1 = a signal above 1/2 the expected signal for a minimum ionizing particle in the first hodoscope

- H2 = a signal above 1/2 the expected signal for a minimum ionizing particle in the second hodoscope

- CAL = A signal above 3.5 GeV in a 'two column sum' in the calorimeter

The 'two column sum' is an analog OR of 20 calorimeter blocks in two adjacent columns. There are 41 column sums for each half of the calorimeter (42 columns). The column sums are staggered so every pair of adjacent columns is included in the trigger.

The details of the calorimetry were discussed in Section 2.4.8. The columns should contain most of the energy of an EM shower regardless of the position where the positron hits the face of the blocks. Scattered positrons with less than 4 GeV/c momentum cannot be used in the asymmetry analysis because of large radiative corrections (Section 4.2.2). Thus, the trigger threshold was chosen to select showers which deposit more than 3.5 GeV in the calorimeter. This calorimeter threshold provides a factor of 10 hadron rejection and accepts the positrons in the interesting energy range for the experiment.

The arrival times of beam bunches at the HERMES interaction point are measured by the HERA Clock and this signal is delayed to be the final element in the fourfold trigger coincidence.

Background

There were two major elements to the background in the HERMES spectrometer. Charged hadrons can fire the trigger if a significant energy is deposited in the calorimeter. The hodoscope elements require a charged particle to traverse the spectrometer (the first hodoscope rejects photons). An energy deposition of more than 3.5 GeV from a hadronic shower or a high energy photon in coincidence with the hadron can fire the trigger. The trigger rate from hadrons with > 4 GeV/c momentum is
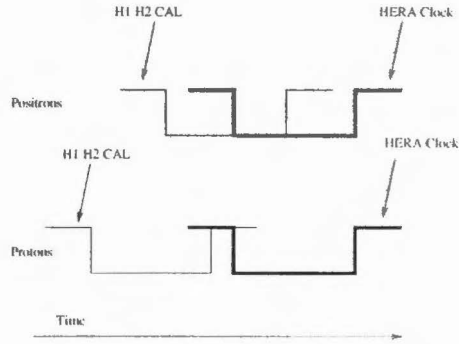
Figure 2.27: Trigger Timing

suppressed by a factor of ~ 10 by the calorimeter threshold. Hadrons in coincidence with a high energy photon also provide a significant trigger rate.

There is a second background from the proton beam. The proton and positron beams arrive at the interaction points simultaneously in the HERA ring. This means there is a time difference of 42 ns (2 x 7 m) between their interactions with the calorimeter relative to the HERA clock. This difference is exploited to veto the proton events with the clock signal. Effectively, the calorimeter and hodoscope signals are early relative to the HERA clock for protons. Figure 2.27 shows the timing for the standard proton and positron bunches. The coincidence timing is set so protons showering through the spectrometer will not fire the trigger.

The protons can also have stable orbits outside of the standard orbits defined by the RF, thus showers from protons outside the RF bunches which interact upstream of the calorimeter can fire the trigger. This background varied dramatically from fill to fill and even within fills. Triggers associated with this background do not contain tracks which reconstruct to the target and have a distinctive high multiplicity in the back detectors due to the 800GeV/c proton showers traversing the BCs. This background can contribute significantly to the dead time in the data acquisition system because they occasionally have a high rate and the triggers have a large size due to high multiplicities in the chambers events.

In general, the dead time was very small for most of the data taking. With a current of 30 mA and a target density of 10^{15}nucleons/cm^2, the expected DIS rate is 4.4 Hz [22]. Typically the trigger rate is 65 Hz and the livetime is 95%. Approximately 30 Hz

of this rate is due to hadrons which deposit enough energy to trigger the calorimeter and the remainder $\sim$ 30 Hz contain no tracks. (These are probably due to photon conversion before the first hodoscope.) The trigger rate did reach 200 Hz when the proton background was very bad.

Chapter 3   Particle Identification

3.1   Particle Identification

A clean and efficient identification of the scattered positrons is crucial for inclusive measurements in the HERMES experiment. Furthermore, it is desirable for semi-inclusive physics that hadrons be identified over a large kinematic range. The HERMES experiment uses four particle identification detectors: a lead glass calorimeter, a preshower detector, a Cerenkov detector and a transition radiation detector. In concert, these detectors provide clear separation of hadrons and positrons. The goal of the particle identification was to use this information to extract an optimal sample of positrons with a high efficiency over all momenta with low hadron contamination.

The detectors were discussed in Chapter 2. This chapter shall focus on the identification of positrons and hadrons using these detectors. As an introduction to this discussion, the response of the detectors to hadrons and positrons is shown in Figure 3.1. The samples of particles were selected by placing strict cuts on the other particle identification detectors and these cuts are a convenient starting point for the particle identification discussion.

3.2   Particle Identification Cuts

A simple particle identification scheme would be a set of cuts on the spectra in the PID detectors. This commonly used method is very convenient because the positron efficiency and hadron rejection factor can be measured for each detector independently. The hadron rejection factor for the calorimeter is low because most of the calorimeter's hadron rejection is at the trigger level. For example, most hadrons with 5 GeV/c momentum deposit less than 3.5 GeV/c in the calorimeter. (This is effectively a first level trigger cut at 0.7 in Figure 2.18.)

Efficiencies and hadron rejection factors for a series of cuts is provided in Table
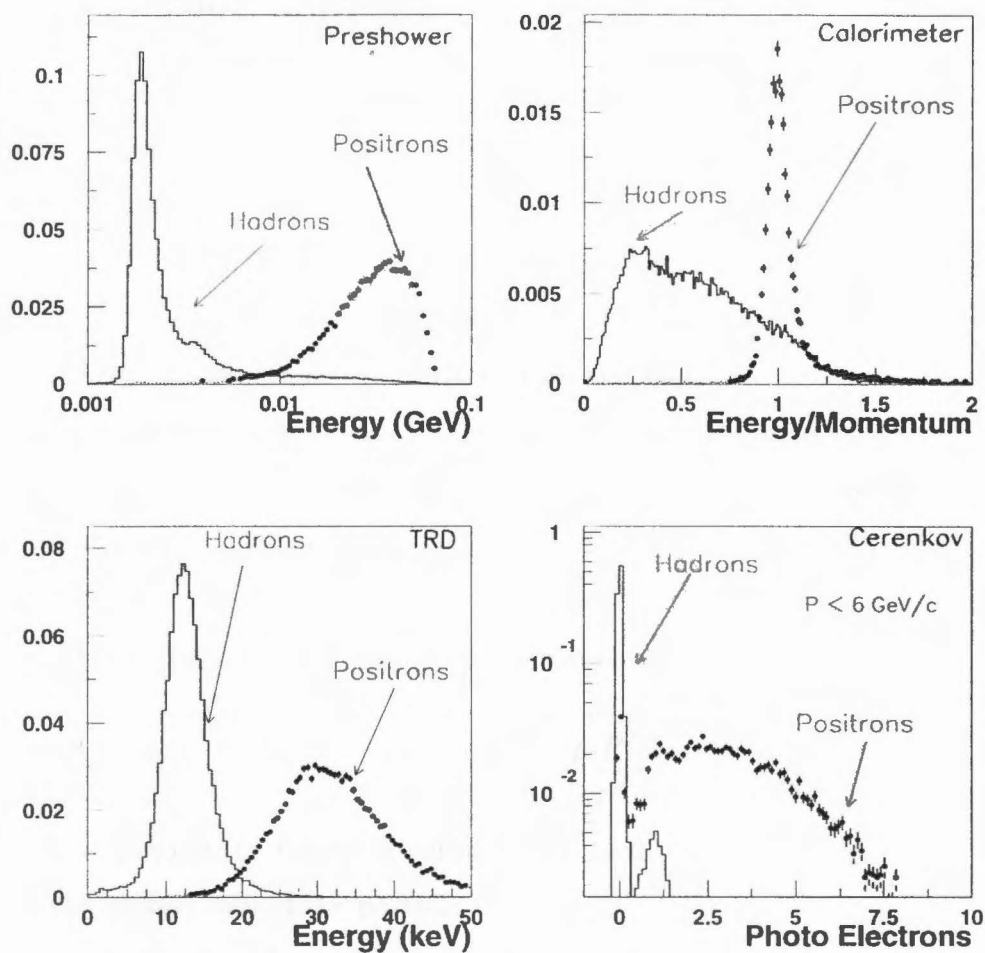
Figure 3.1: Particle Identification Detector Spectra for All Tracks in the DIS Acceptance

Detector	Cut	Positron Efficiency	Hadron Rejection
Calorimeter	$E/p > 0.8$	0.991	0.752
Preshower	$E > 0.01 GeV$	0.969	0.914
TRD	$E > 17.5 keV$	0.975	0.930
Cerenkov	$Signal > 0.25 P.E.$	0.938	0.956
All Four $(P < 6GeV/c)$		0.886	0.999
Cal/Pre/TRD $(P > 6GeV/c)$		0.945	0.998

Table 3.1: Efficiency and Rejection Factors for PID Cuts

3.1. This set of cuts provides very good hadron rejection both in the momentum range where the Cerenkov is useful for PID and at higher momenta.

3.3   Likelihood Method

Rather than using cuts on the individual detectors, the information from the particle identification detectors has been combined into a likelihood function which describes the probability that a particle is a lepton or hadron. This more complicated particle identification scheme has been chosen to achieve a higher positron efficiency while retaining a large hadron rejection factor.

The likelihood functions are derived from the measured spectra of hadrons and leptons within a momentum and angle range. The likelihood of a certain type of particle is given by the probability of a lepton at the designated momentum and angle producing the given signal divided by the probability of a hadron giving the signal.

The likelihoods are based on a Bayesian probability calculation.

$$P(e^+|p, S_{i=1,4}) = \frac{f(e^+|p)P(S_{i=1,4}|e^+,p)}{f(e^+|p)P(S_{i=1,4}|e^+,p) + f(h^+|p)P(S_{i=1,4}|h^+,p)} \tag{3.1}$$

In this equation the following variables are used:

p is the momentum of the particle,

$f(e^+|p)$ is the flux of positrons with momentum p,

$S_{i=1,4}$ are the calibrated signals of the particle identification detectors,

and $P(A|B)$ is the probability of A given B.

The probability defined in this way was not used for the particle identification because of ambiguities in the definition of the fluxes. The fluxes depend on the choice of physics (e.g., inclusive or only events with multiple tracks) and the particle identification variables (PID) were chosen so the cuts would be independent of these fluxes.

A likelihood ratio was defined for use in the particle identification:

Particle Identification cut	Fraction of Data	Average Contamination	Average Efficiency
$PID3 + 0.31TRD(keV) > 5.48$	82%	0.9%	99%
$PID2 + 0.51TRD(keV) > 9.00$	15%	1.7%	99%
$PID3 > 0$	3%	1.6%	99%

Table 3.2: Average Contamination and Efficiencies for the PID Methods Used

$$R(e^+|p, S_{i=1,4}) = \frac{P(S_{i=1,4}|e^+|p)}{P(S_{i=1,4}|h^+|p)} \tag{3.2}$$

The likelihood ratio is either very small or very large for most tracks. This distribution can be viewed more easily by displaying the log of the likelihood ratio. The PID variable

$$PID(e^+|p, S_{i=1,4}) = \log R(e^+|p, S_{i=1,4}) \tag{3.3}$$

will be used throughout this analysis.

3.3.1 The Likelihood Functions

Three different particle identification functions were defined for use in the final data analysis. Two log likelihood ratio variables were used, PID3 and PID2. PID3 is the log of the likelihood ratio for the calorimeter, preshower and Cerenkov. PID2 is the log of the likelihood ratio for the calorimeter and preshower.

PID3 and PID2 were used in conjunction with the 'down-shifting' scheme. Down-shifting is the selection of a valid PID selection based on checks of the detector responses. The details of the down-shifting are provided in Section 4.1.5. The standard PID was PID3+TRD (a cut in the PID3-TRD plane), but additional data was included where either the Cerenkov (PID2+TRD) or TRD (PID3) were not functioning correctly. No data was used when there were problems with the preshower or calorimeter because these elements are required by the HERMES DIS trigger. The shapes of the PID3 and PID3+TRD distributions are shown in Figure 3.2. Positrons are concentrated in the peak at positive values while hadrons form the broad distribution at negative values.
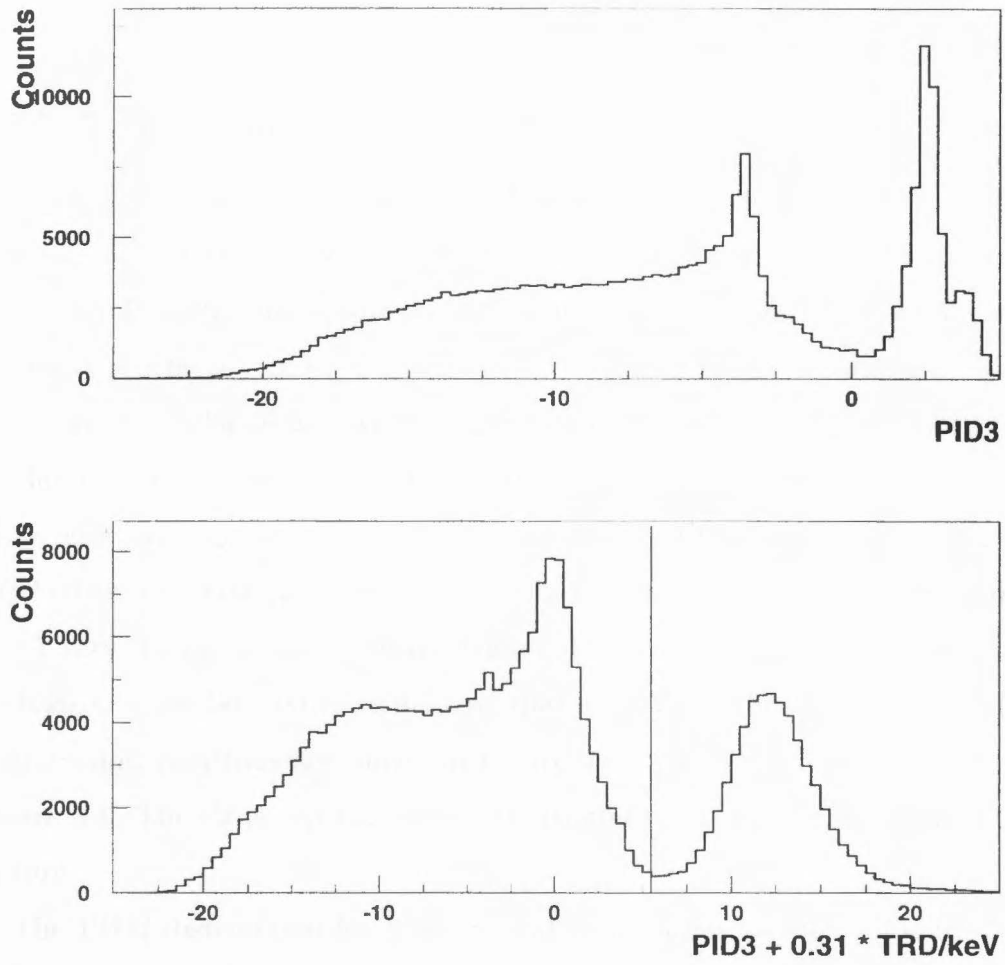
Figure 3.2: Particle Id Variable Distributions

x bin	PID3	
	Contamination	Efficiency
1	$5.5 \pm 0.6\%$	97.2%
2	$5.0 \pm 0.4\%$	97.8%
3	$2.5 \pm 0.2\%$	98.5%
4	$1.5 \pm 0.1\%$	98.8%
5.	$0.5 \pm 0.1\%$	99.2%
6	$0.2 \pm 0.1\%$	99.4%
7	$0.1 \pm 0.1\%$	99.5%
8	$0.0 \pm 0.1\%$	99.5%
9	$0.0 \pm 0.1\%$	99.5%

Table 3.3: Contamination Measurement from TRD

3.3.2 Hadron Rejection and Efficiency

Measuring the hadron rejection and efficiency of a single PID detector is straightforward. Very strong cuts placed on the other three detectors provides a very pure (although, low efficiency) positron or hadron sample. Because the signals in the four detectors are mostly independent it is possible to identify an unbiased spectra for the detectors. (There is a weak, negative correlation between the calorimeter and preshower.) The hadron rejection and efficiency of a cut can easily be calculated with these pure samples. It is more difficult to estimate the contamination and efficiency for the likelihood method because of the lack of independent detectors to place cuts on. A very strong cut on the TRD (energy deposited > 30 keV for e^+ or < 12.5 keV for hadrons) can be used to identify samples for PID3. The distributions for positive hadrons and positrons are shown in Figure 3.3. The PID3-TRD plane is shown in Figure 3.4. The clean separation of hadrons and positrons can be easily seen in this picture.

The PID3 distribution for hadrons and positrons is shown in Figure 3.2. From these distributions, the hadron rejection and contamination can be calculated for a cut on PID3. Table 3.3 shows the measured hadron contamination and positron efficiency for a cut on PID3. The x bins used in the analysis are defined in Section 4.1.17. (The lower bin numbers correspond to low x.)

These contaminations and efficiencies for PID3 are useful for periods when the TRD is not used in the PID. The other PID methods (PID3+TRD and PID2+TRD)

are not amenable to a direct calculation of efficiency and hadron rejection. The Cerenkov does not provide a clean sample of hadrons at any momentum nor a clean sample of positrons above 6 GeV/c. For the PID3+TRD cut, there is no independent particle identification information to use to calculate the efficiency and contamination.

3.4 Positron and Hadron Fluxes for the Inclusive Measurements

To determine the hadron contamination as a function of x, it is necessary to measure the relative fluxes of positrons and hadrons versus momentum for each x bin. The large number of hadrons at low momenta results in a larger contamination at low x. Some of this effect is mitigated by the Cerenkov detector which increases the hadron rejection at low momenta.

The momentum and x distributions of positive hadrons and positrons (Figure 3.5) shows the range where positron identification is critical. For scattered positrons with momenta above 15 GeV/c which corresponds to high x, the hadron contamination is negligible as the positive hadron to positron ratio decreases rapidly with energy.

3.5 Monte Carlo Comparisons

A Monte Carlo simulation of the HERMES detectors was developed to calculate efficiencies and contaminations of the various particle identification methods. In principle, these comparisons could be done with a sample of the full HERMES Monte Carlo (HMC). The simulation of particles in the PID detectors was not done in HMC because of the CPU intensive nature of simulations on EM showers. A boot strap Monte Carlo was developed in parallel with HMC to simulate the PID detectors. A sample of tracks in each detector are used to generate input spectra for the Monte Carlo.

A comparison with the measured contamination and efficiency for PID3 and straight TRD cuts suggest the simulation produces reasonable results. The contaminations from the Monte Carlo and measured with cuts on the TRD are shown in Figure 3.6.
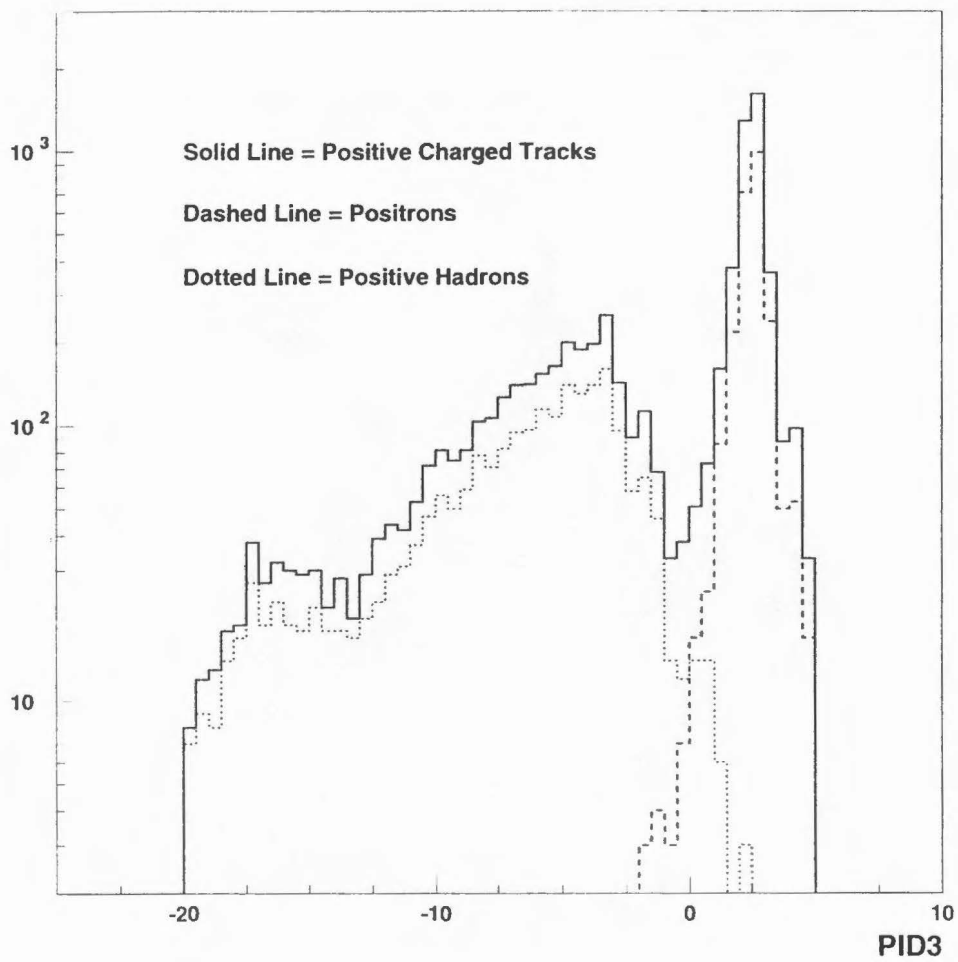
Figure 3.3: PID3: Solid Line All Particles, Dashed Line Positrons, Dotted Line Positive Hadrons
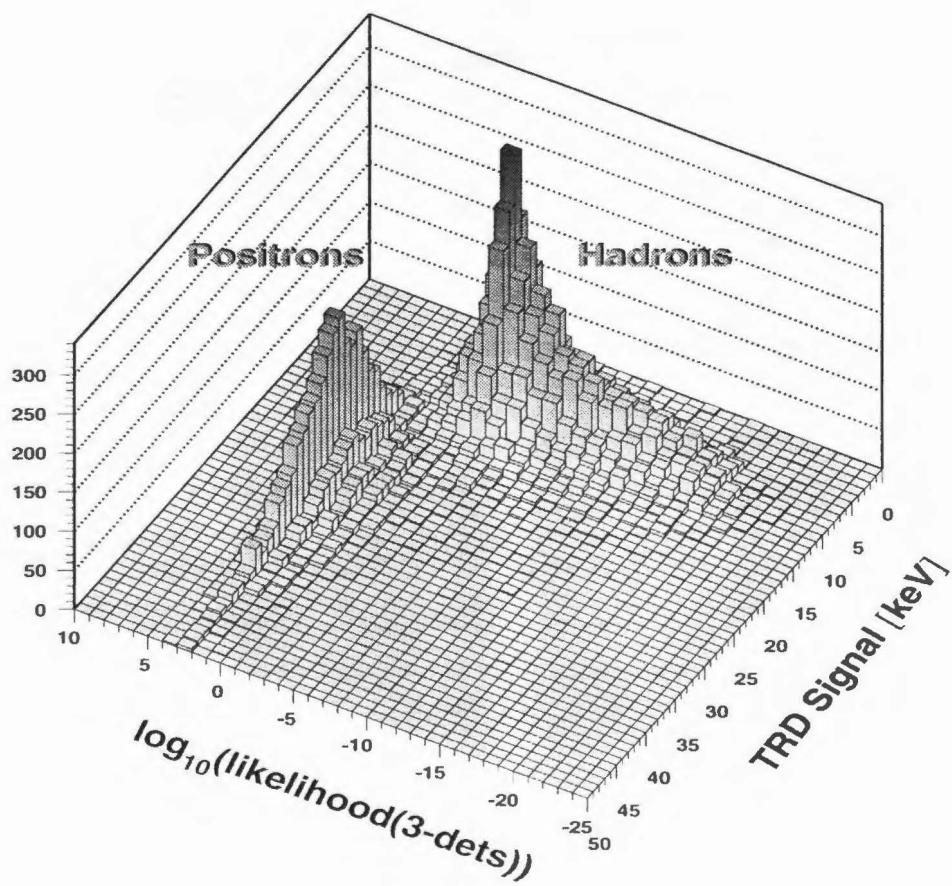
Figure 3.4: PID3 vs TRD Plane
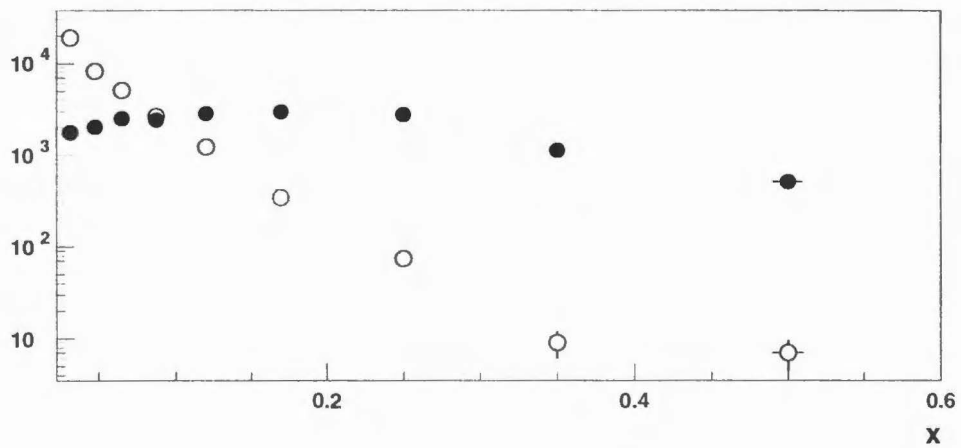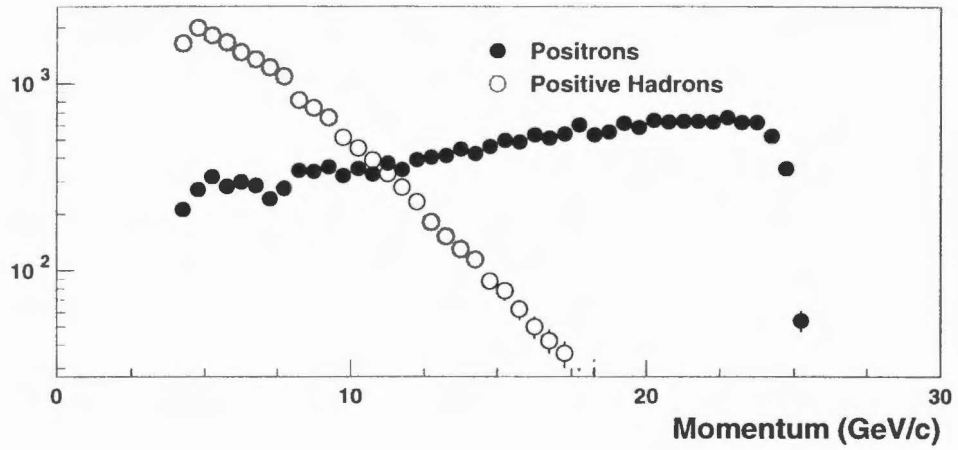
Figure 3.5: Momentum and x Distributions for Hadrons and Positrons for a Sample of Data
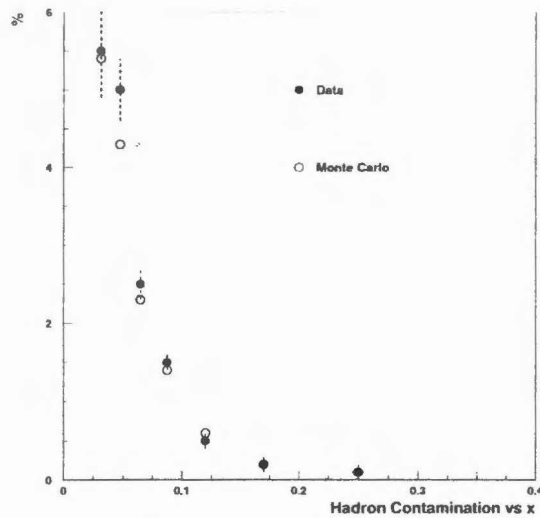
Figure 3.6: Hadron Contamination for the HERMES x Binning

It is not possible to measure the contamination for PID2 + TRD and PID3 + TRD directly. The efficiencies and contaminations for these methods were measured from the Monte Carlo, and the results from Monte Carlo agree with contaminations and efficiencies calculated by extrapolating the tails of the PID distributions [46].

The hadron contamination must be known to correct the contribution of misidentified hadrons to asymmetry measurement. The efficiencies are measured to gauge the effectiveness of the particle identification system. The HERMES experiment is statistics limited. Every attempt is made to identify the positrons as efficiently as possible while maintaining minimal hadron contamination.

X bin	PID3	
	Hadron Contamination	Efficiency
1	5.4%	98.3%
2	4.3%	98.6%
3	2.3%	98.7%
4	1.4%	98.8%
5	0.6%	98.9%
6	0.2%	98.9%
7	0.1%	98.9%
8	0.0%	98.9%
9	0.0%	99.0%

Table 3.4: Monte Carlo Contamination and Positron Efficiency for PID3

x bin	PID3-TRD		PID2-TRD	
	Hadron Contamination	Efficiency	Hadron Contamination	Efficiency
1	3.0%	99.3%	6.8%	99.3%
2	2.1%	99.3%	4.1%	99.3%
3	1.3%	99.3%	2.4%	99.3%
4	0.8%	99.3%	1.4%	99.3%
5	0.3%	99.3%	0.6%	99.3%
6	0.1%	99.3%	0.1%	99.3%
7	0.1%	99.3%	0.1%	99.3%
8	0.0%	99.3%	0.0%	99.3%
9	0.0%	99.0%	0.0%	99.0%

Table 3.5: Monte Carlo Contamination and Positron Efficiency for PID3-TRD and PID2-TRD

Chapter 4   Data Analysis

4.1   1995 HERMES Data Analysis

The 1995 HERMES experiment started in May 1995. After several months of commissioning the spectrometer and target, HERMES started recording asymmetry data in August 1995. From the start of polarized data taking to the 1995 HERA winter shutdown, 150 fills of data were recorded in the HERMES spectrometer. Each fill began with the successful injection of $\sim$ 50mA of 820GeV/c protons and $\sim$ 30 mA of 27.5 GeV/c positrons. The beams would orbit in the storage rings for the next 8 to 12 hours and the positron current would decay to 10mA before the beams were dumped.

Some fills ended prematurely but the majority of the HERMES data were recorded during complete fills. The fills are used as the starting point for the HERMES data analysis.

4.1.1   An Overview of the Data Analysis

To keep the data files a reasonable size, each fill was subdivided into a series of runs of approximately six to ten minutes. The runs contain approximately 1GB of raw data and represented about 1% of a fill. This divided the data into pieces which could be easily handled by the data analysis chain.

An initial run selection was performed to select the runs of interest for the inclusive asymmetry analysis. Runs without a polarized target and runs used to test various components of the detector were removed at this stage.

Each run is divided into a series of scaler 'bursts'. Each burst corresponds to a set of scaler and slow control information that were read every ten seconds. The events from the HERMES spectrometer were synchronized to the correct bursts to ensure that the correct slow control information and scalers (such as the luminosity scaler) were included. The burst is the smallest time unit which is used in the HERMES

analysis.

The data were analyzed burst by burst and only bursts which satisfied strict data quality controls were used in the analysis. Additional cuts were placed on the runs and fills to ensure the data used was from stable data taking periods.

The top and bottom halves of the detector are analyzed independently although some of the inputs and data quality cuts are identical (luminosity, beam polarization, target polarization).

4.1.2 The Analysis Chain

Data were taken at the HERA East Hall and stored locally on 8mm tapes and a series of local disks. At the end of a fill, the data were transferred to the computing center at the DESY main site. The data stored at the main site was used for the analysis chain and the original data storage tapes are used as a backup of the data.

At the start of the data analysis, the HERMES decoder (HDC) converted the digitized time (TDC) and integrated charge (ADC) signals to positions and energies associated with tracks through the spectrometer. The reconstruction program (HRC) used this information to reconstruct tracks through the spectrometer. The files (hrc.events) containing all tracks with no particle identification selection are substantially smaller than the raw data and are stored for further analysis. Several iterations were performed on this stage of the analysis to correct the calibration and alignment information used in the analysis and to optimize the tracking parameters. The fifth version (version E) of the reconstruction was used in the final analysis.

This tracking information is then merged with the slow control information to produce a data summary tape 'DST' which can be used for the asymmetry analysis. The DSTs include the DIS candidate events. Figure 4.1 shows the flow of information in the analysis chain.

Several iterations were performed on the extraction of the DSTs to check the event synchronization codes and information extraction. The data set has been thoroughly checked and the final analysis is based on version E5 of the g1DST.
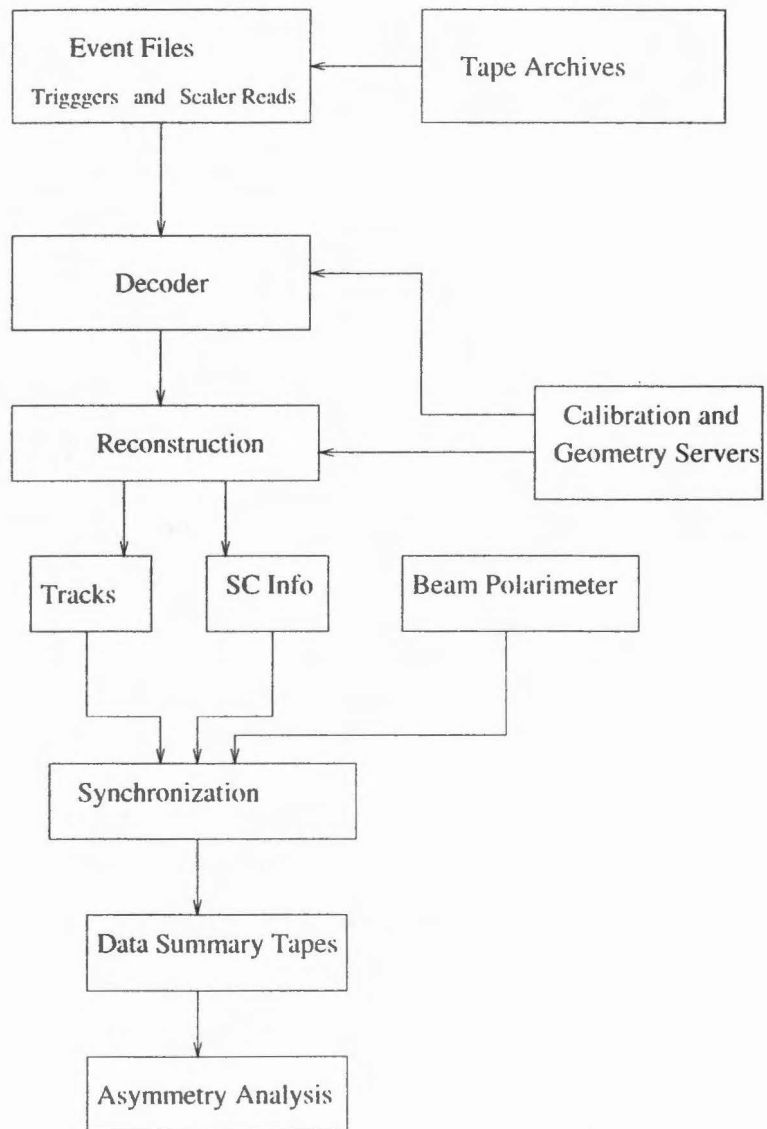
Figure 4.1: Off Line Analysis Chain

Detector	# of allowed bad channels	
	Top	Bottom
Calorimeter	3	4
Hodoscope 2	1	1

Table 4.1: GMS Gain Cuts

4.1.3 Initial Run Selection

Of the 3238 runs, 2811 were acceptable for the asymmetry analysis. Runs which were obviously not appropriate for the asymmetry analysis were rejected. These included runs with no target gas, hydrogen or deuterium gas in the target, detector studies at non-standard voltages, tracking studies with the spectrometer magnet off, and unpolarized ^3He runs.

4.1.4 Particle ID Criteria

Information from the particle identification detectors was used to reject runs without enough hadron rejection for the asymmetry analysis. Many of the checks of the particle identification detectors (such as efficiency and gain measurements) required more statistics than are in a burst. Thus, the particle identification checks are performed on a run basis.

Gain Monitoring System

The GMS was used to monitor the gain stability of the preshower, calorimeter and luminosity monitor during the experiment. The information for the preshower and calorimeter was used to check the gain of individual photomultiplier tubes to determine if the detector was functioning correctly. A linear fit of detector response vs GMS photo diode response was performed for each run. If the slope of the fit differed by more than 15% from nominal, the detector was considered bad for that run. The cuts placed on this information for the detectors are shown in Table 4.1.

The calorimeter cuts differ because a single calorimeter block in the bottom of the detector was off for the entire data taking period.

Detector Efficiencies

The efficiencies of nominal cuts for the four particle ID detectors (Cerenkov, TRD,

Detector	Nominal Cut	Good Cut
Calorimeter (E/P)	0.8	0.9
Preshower (GeV)	0.010	0.020
Cerenkov (P.E.)	0.25	0.50
TRD (keV)	17.5	25.0

Table 4.2: Cuts Used in Efficiency Studies

PID method used	Fraction of Runs
PID3 + TRD	82%
PID3	3%
PID2 + TRD	15%

Table 4.3: Fraction of Data Involved in Down-shifting

preshower, and calorimeter) were determined by the following formula, e.g.:

$$\epsilon_{cer} = \frac{N\left((cer)_{nom}(TRD)_{good}(pre)_{good}(cal)_{good}\right)}{N\left((TRD)_{good}(pre)_{good}(cal)_{good}\right)} \tag{4.1}$$

where N is the number of positrons which satisfy the chosen cuts, *nom* indicates the nominal cut for the detector, and *good* indicates a strict cut on the detector which gives a clean positron sample.

4.1.5 Down-shifting

The efficiency of the Cerenkov detector was required to be above 92.5% for the run to be used in the analysis. (The nominal efficiency for the Cerenkov was 95%.) The efficiency for the TRD was required to be above 92.5 for a cut of 17.5 keV. (The nominal efficiency of this cut was 97%.)

The efficiencies of the PID detectors monitored the performance of the detectors and selected the method of PID used in the analysis. For certain periods in the data, either the Cerenkov or the TRD was not functioning correctly. If both the Cerenkov and the TRD, or either of the Hodoscopes or calorimeter, were not functioning, the run was thrown out of the analysis. If one of the Cerenkov or TRD were not functioning, a PID 'down-shifting' scheme was used. Basicly. the information from the disabled detector was ignored. The experiment could still function with three PID detectors

Selection Criteria	Runs Remaining	
	Top	Bottom
full data set	4011	4011
log book	3046	3046
beam polarization	2326	2326
target polarization	2180	2180
particle id	2006	2130

Table 4.4: Run Quality Summary

because of the large redundancy in the HERMES spectrometer. This scheme could not be used with the hodoscopes or calorimeter. If either were not functioning nominally, preliminary analysis showed that events were not detected by the first level trigger and the detected events were therefore unusable.

4.1.6 Burst Quality Criteria

2180 runs (2006 Top and 2130 Bottom) remained after the initial run quality selections. These runs (Table 4.4) satisfied the preliminary data quality checks and are considered to be of suitable quality to use in the next stage of the asymmetry data selection.

The bursts within the selected runs were checked for problems on a shorter time scale. The burst selection is based on the following criteria:

- Beam polarization

- Target polarization

- Luminosity and live time

- Chamber efficiencies (high voltage trip detection)

- Scalar Rates

Each of these criteria will be discussed in turn. These criteria were applied to the upper and lower halves of the detector separately (when appropriate). A burst was determined to be "good" for inclusive physics if at least one half of the detector passed all the criteria listed above.

4.1.7 Beam Polarization

The beam polarization was required to be above 40%. The luminosity tunes for the storage ring include an optimization for positron polarization and easily satisfy this criteria. Establishing the luminosity tune would take approximately 45 minutes after the positron beam was ramped to its final energy. The Sokolov-Ternov effect polarizes the beam in about 30 minutes so the polarization reaches its asymptotic limit before the data taking begins. The data removed by the polarization cut fall into two other categories.

1) There are several periods where no polarization measurement was available because of problems with the beam polarimeter.

2) It is necessary to depolarize occasionally the beam in order to measure the rise time for calibration purposes (see Section 2.2.1). The rise times calculated from these fills dominate the systematic error of the beam polarimeter [22]. An attempt was made to balance the demands of the polarimeter for quality rise time measurements and the need for data with stable beam polarization.

The polarization measurements are made on a one minute time scale. The raw beam polarization is fit to a cubic spline and the spline values are used in the analysis. The average beam polarization was 55% with a fractional systematic uncertainty of 5.4%. The uncertainty was dominated by the calibration error from the rise time measurements. A resonant depolarization and subsequent rise time is shown in Figure 4.2.

4.1.8 Target Polarization

Two polarimeters (Section 2.3.1) were used to provide a redundant measurement of the target polarization. A pumping cell polarimeter (PCP) was the primary polarimeter and measured the absolute polarization of the target gas to a high statistical precision. A target optical monitor (TOM) was also used which measured the polarization relative to the PCP. The TOM was calibrated relative to the PCP at the start of the experiment and the polarimeters never significantly disagreed during the 1995 running period. The polarization value from the PCP was used for most of the data
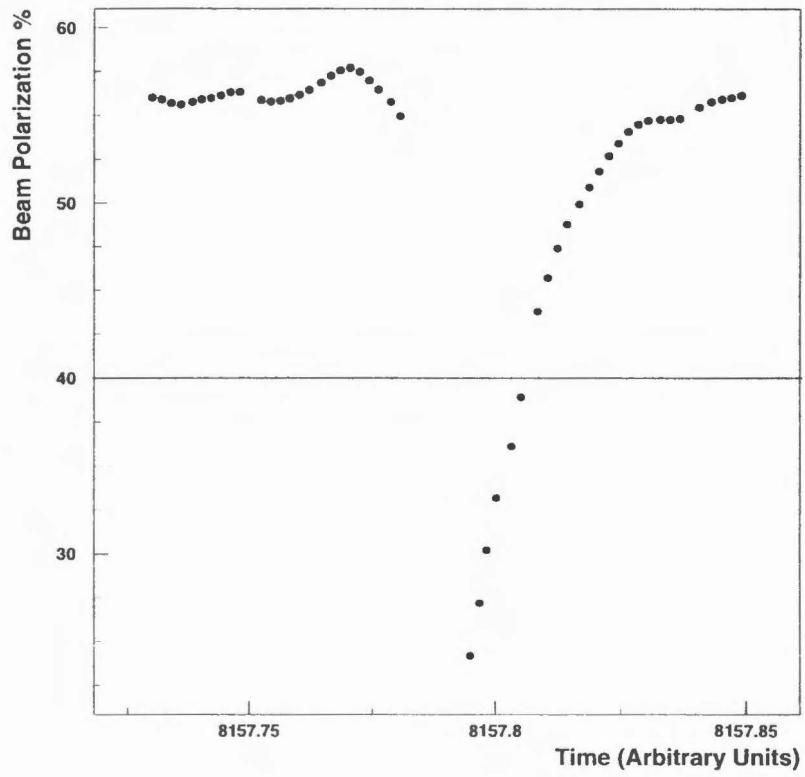
Figure 4.2: Beam Polarization Versus Time During a Risetime Measurement

set. For a small time period, the PCP was broken and the TOM was used to measure the polarization. Because of the lower statistical accuracy of the TOM, only one polarization value per fill could be determined. This value agreed with the average polarization value of the PCP during fills when both polarimeters were working and no time dependence within a fill (other than spin flipping) was observed.

The target spin direction was flipped every ten minutes and it took approximately 30 seconds for the spin to precess from one direction to the other. Data acquired while the spin was flipping were not used in the asymmetry analysis and the bursts where the spin was starting to flip and finishing the flip were also eliminated from the data set. The absolute value of the polarization as the spin flips is shown in Figure 4.3.

The target polarization measurement was required to be in a reasonable range for analysis. It was not possible to get polarizations above 60% in the flowing cell and data with a polarization below 30% was not used because of its low statistical significance.

Thus the following cuts were placed on the target information:

- Target polarization parallel or anti-parallel to beam
- PCP polarization: $30\% < P_t < 60\%$
- TOM polarization: $30\% < P_t(\text{fill average}) < 60\%$

The average target polarization was 46% for the analyzed data with a fractional systematic error of 5%.

4.1.9 Luminosity

For each burst the rate in the luminosity monitor was required to be between 40 and 210 Hz. Because the beam current varies on a time scale consistent with the target spin flip, an accurate luminosity measurement for the two spin states is crucial for the HERMES measurements. Typically the HERA e+ beam was filled to ~ 30mA and dumped at approximately 10 mA. This corresponds to a Bhabha scattering rate in the luminosity monitor of 175 Hz at the beginning of a fill and 60 Hz at the end of a fill with the standard target density (10^{15}nucleons/cm^2).

The luminosity from the luminosity monitor is cross-checked with the beam cur-
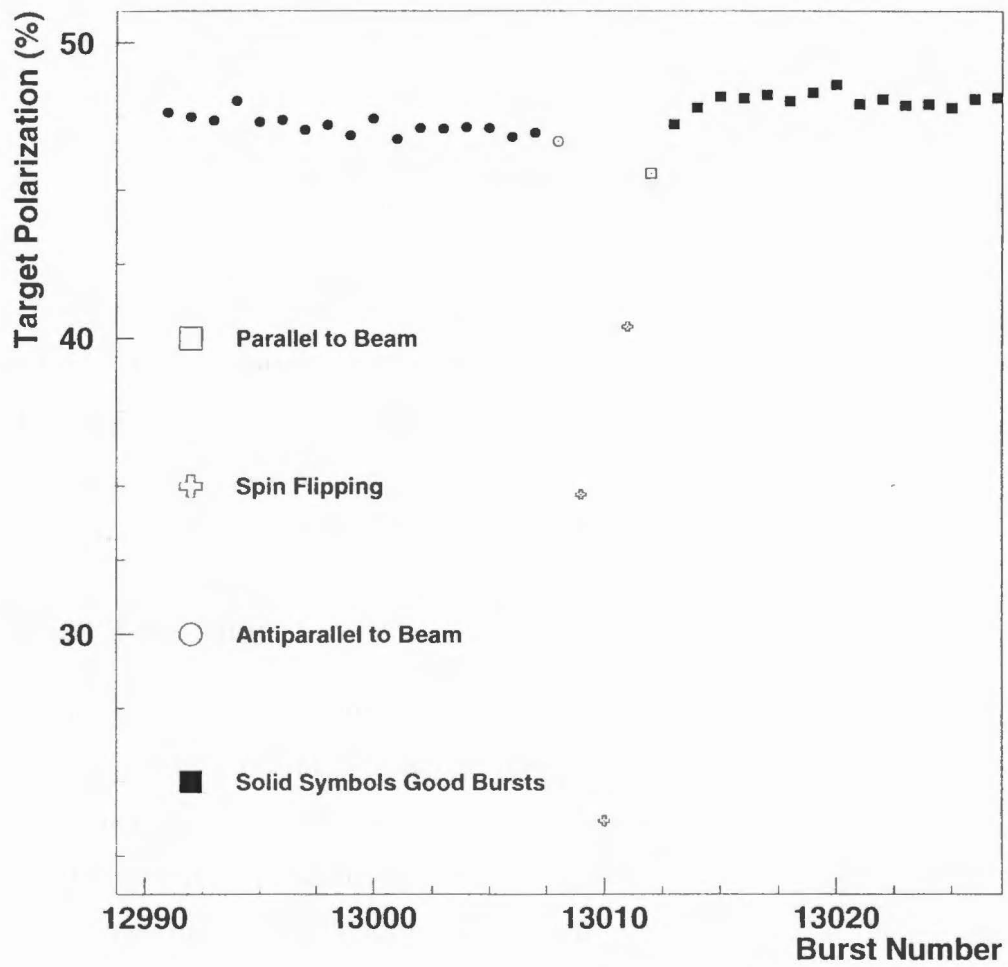
Figure 4.3: Target Polarization Versus Time Near a Spin Flip

rent and target density measurements as shown in Figure 4.4. It is possible to use the beam current and target density to calculate the total luminosity. However, the target density depends on the temperature of the gas in the target which is not well measured. The nozzle temperature is measured but the uncertainty in gas temperature is still too large to make a better measurement than the Bhabha scattering.

The following cuts were imposed:

$$40 < \text{luminosity rate} < 210Hz \tag{4.2}$$

$$5.0 \cdot 10^{-15} < \frac{\text{luminosity rate}}{\text{beam current * target thickness}} < 7.2 \cdot 10^{-15} \text{Hz/mA/(nucleon/cm}^2) \tag{4.3}$$

Within a fill, the ratio of luminosity monitor rate to beam current and target thickness was constant but it varied from fill to fill. The asymmetry analysis was performed on a fill by fill basis to avoid any problems due to fill to fill luminosity normalizations. The 1% time dependence of the luminosity within a fill is small and was discussed in Section 2.4.11.

4.1.10 Live Time

The live time was required to be at least 60%. The rates in the HERMES spectrometer are low and the livetime is usually greater than 90%. The proton background can greatly increase the event rate in the spectrometer. When the proton background is large, the livetime can noticeably decrease.

The structure seen at small live time seen in Figure 4.5(a) is the result of a period at the start of each run when the trigger is re-initialized. The first three bursts (30 seconds of 10 minutes) are not used because of this problem. The livetime for each burst in a run is shown in Figure 4.5(b).

Varying the live time cut between 50 and 80% had little effect on the result. The results of systematic variations of cuts are summarized in Section 4.6.1.
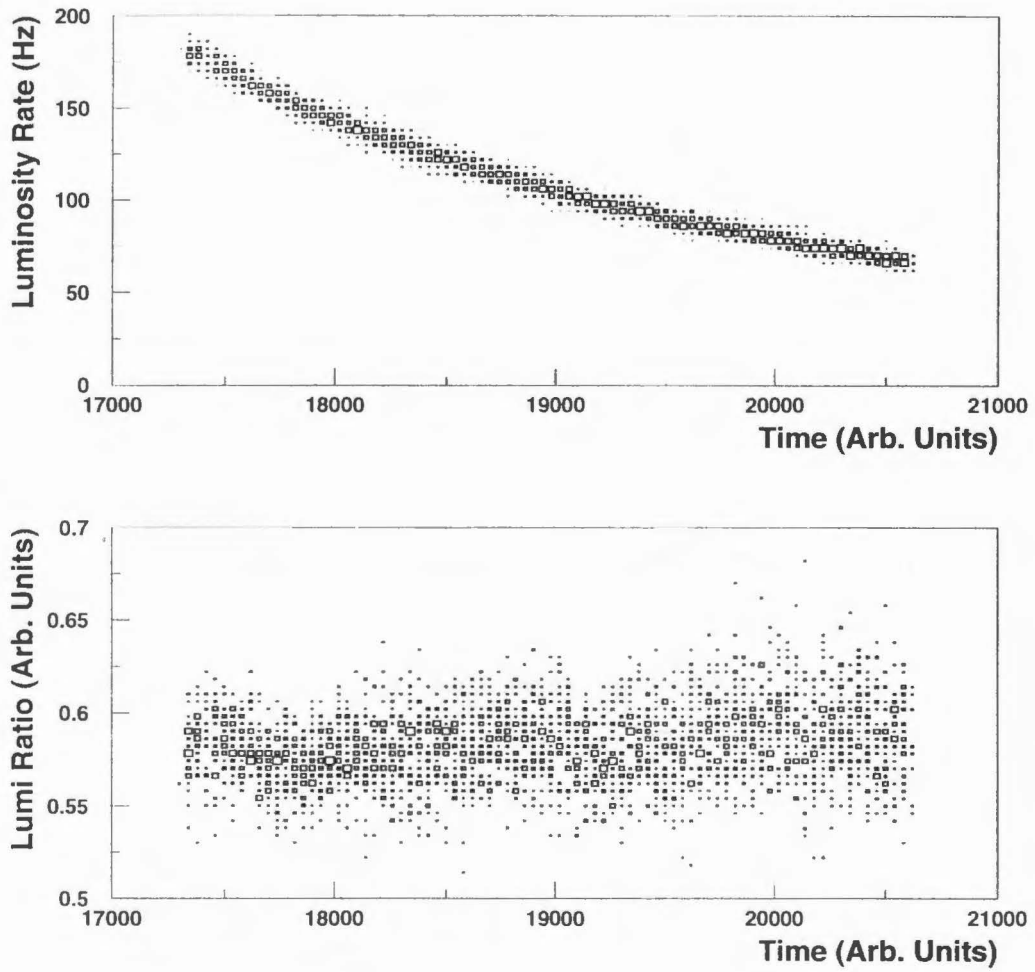
Figure 4.4: Luminosity Versus Time and Luminosity/Current/Target Density for a Fill
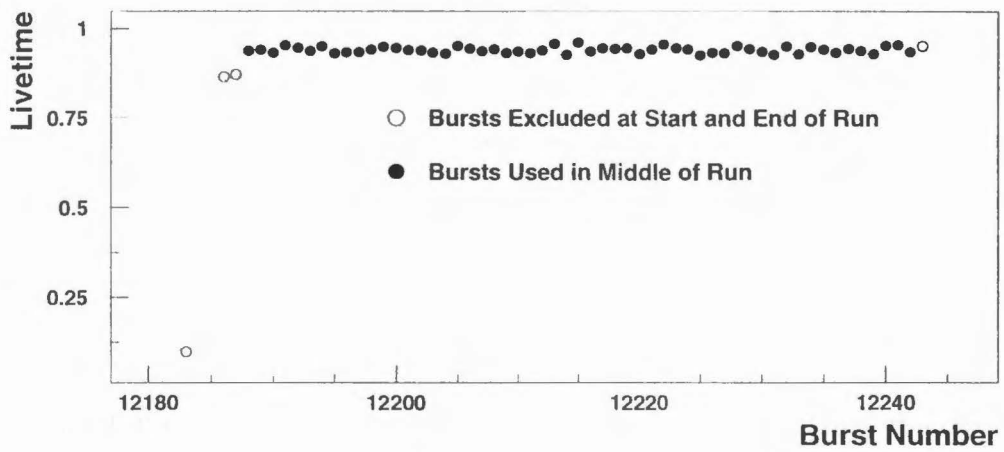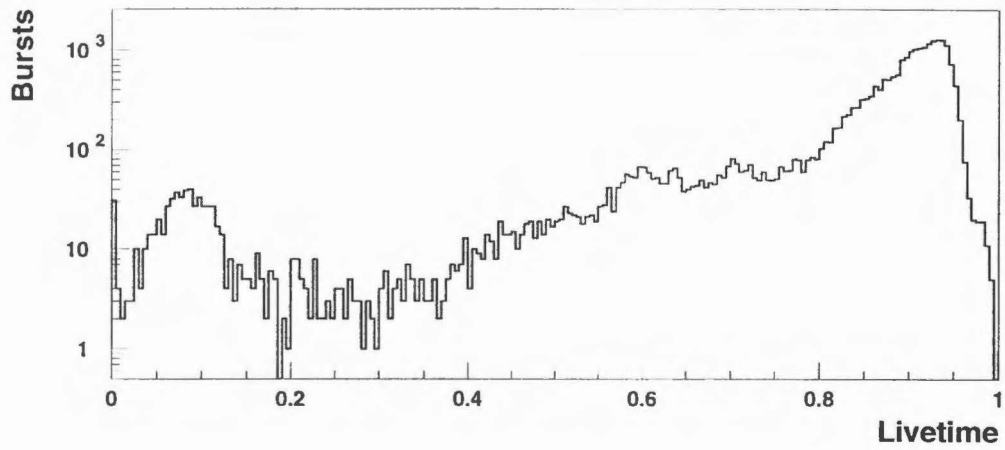
Figure 4.5: (a) Live Time Distribution for a Subset of Data and (b) Livetime per Burst for One Run

4.1.11 Chamber High Voltage Trip Detection

The ACE program (Section 2.4.5) was used to calculate burst by burst efficiencies for all drift chamber planes and total track finding efficiencies for the front and back regions of the top and bottom of the spectrometer. A detailed discussion of ACE was included in Section 2.3.4.

The total tracking efficiency is created by summing the product of efficiencies over each possible combination of chambers that would produce a reconstructed track. An efficiency cut was used on these front and back efficiencies that was varied from 80% to 97.5% to study the systematic variations. The standard cuts were 80.0% front and 95% back. The back region tracking efficiency is higher than the front because of the higher chamber redundancy in the back region (Section 2.4.3).

Background due to hadronic showers from the collimators and synchrotron radiation can produce high currents in the drift chambers. The high voltage of the drift chambers would often 'trip' (rapidly turn off) due to these high currents to protect the chambers. When a trip was detected, the tripped half of the HERMES detector (top or bottom) was not analyzed until the efficiency had risen above the threshold (voltage had ramped back to its nominal value). The burst before the trip was also removed. (The rapid onset of trips often meant the burst before a trip contained a few seconds of good data followed by a period with no reconstructed tracks. The burst will then have a reasonable tracking efficiency calculated from the tracks at the start of the burst but the total number and time distribution of the tracks indicate a track reconstruction problem.) The efficiency of any plane was defined to be zero if no tracks existed to calculate an efficiency for that chamber.

When the high voltage trips off the yield of tracks rapidly goes to zero. Figure 4.6 shows the tracking efficiency (which is a strong function of chamber voltage) and total tracks per burst. It is clear that the data with low tracking efficiency is unusable. A cut is placed to ensure the data has a high efficiency but no correction is made for the tracking efficiency. The chamber efficiencies do not fully correct the difference in event rate when the chambers are run at different voltages or thresholds. The corrections within a fill are small (< 1% variations in the efficiency for good data

within a fill) so they were neglected because of the problem normalizing periods with large efficiency differences.

4.1.12 Scalers

The scaler rates were used to determine if the first hodoscope was working. The rates are very background sensitive but requiring the scalers be non-zero for each burst removed several periods where several channels had tripped. (The PMTs like the drift chambers will trip to protect themselves if their current is too large.) Requiring the scaler rates in each paddle to be non-zero provides little information on the gain of each paddle but is sensitive to trips which turn the paddles off. The first hodoscope is required in the trigger, and including data during hodoscope trips can introduce helicity correlated false asymmetries due to the changes in the trigger efficiency.

4.1.13 Synchronization and Run Initialization

A trigger initialization procedure was performed at the start of each run. During this procedure the digital signal processors were reloaded with the trigger logic. As a result, the first three bursts of each run had very large dead times and were not used in the analysis.

The last burst of each run was eliminated to ensure correct synchronization. The end of run signal from the electronics was not synchronized with the burst reads so there are ambiguities in the amount of time events were recorded during the last burst of each run.

4.1.14 Summary of Burst Cuts

Single bursts were removed from the data set if they failed one of the following criteria:

1) $0.6 \leq$ livetime ≤ 1.0

2) 40 Hz $\leq$ luminosity rate ≤ 210 Hz

3) Burst length < 9 seconds or > 11 seconds

4) Previous burst was in a different target spin state

5) Efficiency Cuts (80% front, 95% back)
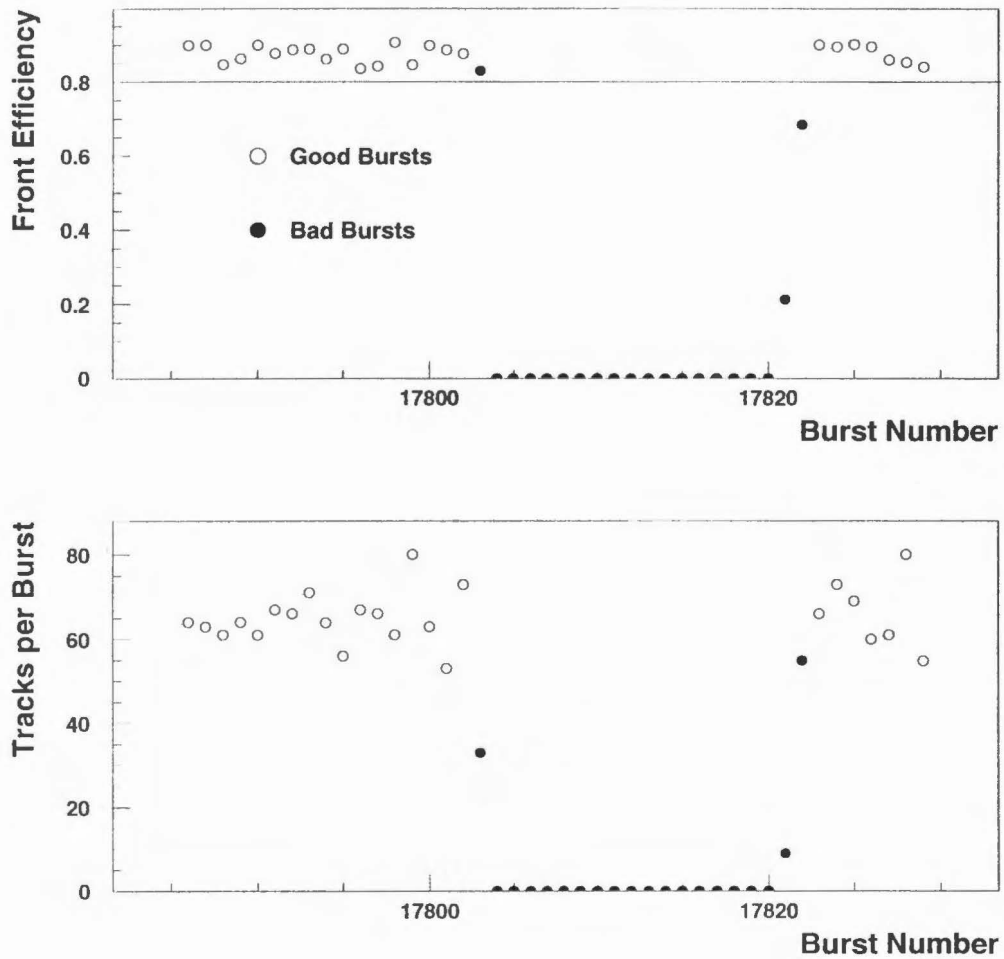
Figure 4.6: Efficiency and Reconstructed Tracks per Burst Near a Detected Trip in the Front Chamber

Selection Criteria	Top		Bottom	
	Runs	Fills	Runs	Fills
initial set	2006	88	2130	88
run stability	1517	72	1609	73
fill length	1441	55	1556	61

Table 4.5: Secondary Run Quality Summary

6) The first three bursts and last burst from each run were removed to eliminate ambiguities from the event synchronization and run initialization problems.

4.1.15 Secondary Run and Fill Selection

The first level data quality checks reduce the HERMES data set to 2180 runs for asymmetry analysis. The burst cuts remove bursts throughout these runs. An attempt has been made to base the analysis on periods of stable data taking. Thus, several other periods were removed from the data sample to select only periods where the data taking was stable. Runs where large periods fail the burst cuts were not used in the analysis and fills with only a small amount of data after these run cuts were also not used.

Any run where more than 30% of the bursts were removed because of trips or any other problems was considered to be unstable. This 'swiss cheese' cut was used to remove periods where there may be instabilities in the spectrometer. The runs which remained after this cut were summed by fill. If a fill had fewer than 200 good bursts in either target spin state, the fill was rejected. Only a small number of fills were removed by this cut and most of the data were from fills with long periods of stable data taking.

This defined the HERMES data for the asymmetry analysis. 64 fills contained long periods of stable data taking which were considered to be suitable for asymmetry analysis. Table 4.5 summarizes the final data selection. A total of 1642 (1441 Top and 1556 Bottom) runs are included in the inclusive physics analysis.

4.1.16 Event Selection

The DIS positrons are extracted from the bursts which have been selected for the analysis. To be selected as a positron candidate, a track must pass a series of cuts to determine that it was a deep inelastic positron from the ^3He target. The cuts placed on the data are listed here.

- $y < 0.85$ (y = ν/E_{beam}) excludes the region with large radiative corrections.

- $Q^2 > 1.0[GeV/c]^2$) ensures the data can be interpreted in terms of a quark-parton model.

- $W^2 > 4.0[GeV/c]^2$ excludes the resonance region by demanding a large invariant mass.

- -30 < Z Vertex < 30 cm (z position at closest approach to the beam axis) and

- T Vertex < 2.0 cm (transverse distance from the beam axis at closest approach) select the He target region.

- abs(Θ_y) > 0.04 ensures the track is fully inside the HERMES spectrometer.

- PID cuts were discussed in Chapter 4.

The positron candidates are binned in x, y, target spin state, and detector half for the asymmetry analysis.

4.1.17 Y Binning

The depolarization factor, D, was introduced in Chapter 1 in the discussion of the extraction of A_1 from the measured asymmetry. The depolarization factor weighs the measured asymmetry and represents the polarization of the virtual photon exchanged by the positron and nucleus.

The HERMES spectrometer has a wide kinematic acceptance and the depolarization factor varies by up to a factor of three for events with low x. The data is also binned in

$$y = \frac{\nu}{E} \tag{4.4}$$

to reduce the variation of the depolarization within a bin. The boundaries of the nine x by three y bins are shown in Table 4.6. Table 4.7 shows the variation of the mean depolarization for the chosen boundaries. The boundaries (y_{low}, y_{1-2}, y_{2-3}, and y_{high}) of the three y bins provide roughly equal statistics for each bin.

x bin	x_{low}	x_{high}	y_{low}	y_{1-2}	y_{2-3}	y_{high}
1	0.023	0.04	0.00	0.68	0.78	0.85
2	0.04	0.055	0.00	0.53	0.67	0.85
3	0.055	0.075	0.00	0.42	0.58	0.85
4	0.075	0.01	0.00	0.34	0.49	0.85
5	0.10	0.14	0.00	0.27	0.42	0.85
6	0.14	0.2	0.00	0.22	0.34	0.85
7	0.2	0.3	0.00	0.17	0.26	0.85
8	0.3	0.4	0.00	0.14	0.23	0.85
9	0.4	0.6	0.00	0.15	0.22	0.85

Table 4.6: x and y Bin Boundaries Used in the Analysis

By binning the data in y as well as x, the variation of the depolarization factor for a given x bin can be reduced. The asymmetries are calculated for each x and y bin and averaged over the y bins for quantities which are a function of x.

$$\frac{A_{\parallel}(x)}{D} = < \frac{A_{\parallel}(x, y)}{D(y)} > \tag{4.5}$$

combines the data with different statistical significance in a natural fashion.

y Bin	x Bin								
	1	2	3	4	5	6	7	8	9
1	0.5981	0.4308	0.3194	0.2472	0.1920	0.1518	0.1163	0.1049	0.1234
2	0.7404	0.5825	0.4669	0.3776	0.3083	0.2502	0.1938	0.1690	0.1771
3	0.8339	0.7700	0.7066	0.6328	0.5649	0.4813	0.3920	0.3501	0.3281

Table 4.7: Mean Depolarization for the x,y Bins

4.1.18 Corrections from the Transverse Asymmetries

Because the momentum of the virtual photon is not parallel to the momentum of the positron, the measured asymmetry, $A_{\parallel}/D$, contains contributions from both A_1^{3He} and A_2^{3He}.

x	$< Q^2 >$	A_2^n	$\sqrt{R}$
0.035	1.06	-0.080±0.241	0.58
0.050	1.27	-0.007±0.166	0.54
0.078	1.87	-0.016±0.138	0.56
0.124	2.69	-0.210±0.156	0.53
0.175	3.40	-0.313±0.204	0.47
0.248	4.00	-0.013±0.241	0.43
0.344	4.46	0.219±0.424	0.39
0.466	5.52	-0.945±0.787	0.33

Table 4.8: A_2^n Measurements from E142 [46]

$$A_{\parallel}/D = A_1 + \eta A_2. \tag{4.6}$$

A measurement of the transverse asymmetry was deferred to maximize the statistics in the measurement of the longitudinal asymmetry. Using the positivity bound on A_2^n ($\sqrt{R}$) would introduce a significant systematic uncertainty in this measurement. Previous measurements of A_2^{3He} suggest that it is consistent with 0, and Table 4.8 shows the values of $A_2^n = F_2^{3He} p_n A_2^{3He} / F_2^n$ measured by the E142 collaboration [47].

It has been assumed that $A_2^n(x)$ is zero and a systematic error equal to the statistical error of previous measurements has been assigned to this quantity. For the two highest x bins, the positivity limit ($\sqrt{R}$) is used because the statistical errors in the measurement are not a stronger constraint on the asymmetry than the positivity limit. Because it has been assumed that the transverse contribution to the measured asymmetry is zero, the transverse terms will be neglected in the following analysis formulae until the discussion of systematic errors is continued in Section 4.6.

4.2 Calculating A_1^{3He}

With the event selection complete, the asymmetry could be extracted from the data summary tapes. The raw asymmetry for scattering from ^3He, $A_{\parallel}$, is extracted for each fill via

$$A_{\parallel}(x, y) = \frac{N^- L^+ - N^+ L^-}{N^- L_P^+ + N^+ L_P^-} \tag{4.7}$$

where the following quantities are sums of all good bursts in a fill:

- N is the number of positrons in a x,y bin,

- L is the observed luminosity (sum of the luminosity monitor scaler),

- and L_P is the total polarization weighted luminosity ($\Sigma L P_t P_b$).

The signs refer to parallel (+) and antiparallel (-) spin alignment of the beam and target.

$A_{\parallel}$ is used for systematic studies of the data (see Section 4.4.1) and the asymmetry is averaged over y bins to calculate $A_{\parallel}(x)/D$ (see Section 4.1.17). Further corrections are required before the physics asymmetries discussed in Chapter 1 can be extracted from the data. These include background, nuclear, and radiative corrections.

Background corrections modify the desired DIS scattering asymmetry due to misidentified hadrons and positrons from charge symmetric processes. These backgrounds can dilute the desired asymmetry and introduce additional asymmetries which must be treated as corrections. The asymmetries from the background processes are measured along with the DIS positron asymmetries to correct the measured asymmetry and extract $A_{\parallel}^{e^+}/D$, the asymmetry from DIS positrons.

Radiative corrections are necessary to extract the single photon exchange asymmetry (Born asymmetry) from the observed asymmetry which is the sum of the first order process and higher order electro-weak processes.

Nuclear corrections relate the asymmetry for the ^3He nucleus to the neutron asymmetry.

4.2.1   Backgrounds

There are two components in the background for the inclusive positron measurement: contamination of misidentified positive hadrons and positrons from non-DIS charge symmetric processes.

$$A_{\parallel} = A_{\parallel}^{e^+} \frac{e^+}{e^+ + e^- + h^+} + A_{\parallel}^{e^-} \frac{e^-}{e^+ + e^- + h^+} + A_{\parallel}^{h^+} \frac{h^+}{e^+ + e^- + h^+} \qquad (4.8)$$

e^+ is the number of events from DIS scattered positrons.

x bin	e^+	e^-	h^+	h^-
1	266323	18305	955883	771548
2	304438	9234	670453	508733
3	356959	5545	503592	367422
4	355833	2755	283316	200337
5	420981	1171	145011	100516
6	423038	305	44118	28965
7	395999	90	10352	5617
8	167323	17	1480	541
9	75803	6	454	126

Table 4.9: Total Events in Full Run List (Nominal Cuts)

e^- is the number of events from charge symmetric processes.

h^+ is the number of events from misidentified hadrons.

All these quantities are measured simultaneously in the HERMES spectrometer. With a knowledge of the fraction of events of each type and the asymmetries of the background processes, one can calculate the asymmetry from DIS scattering from the ^3He nuclei.

Table 4.9 displays the total event sample for each particle type in the spectrometer. The details of the particle identification are included in Chapter 3 and the two background corrections will now be discussed.

Hadron Contamination

The correction for the misidentified positive hadrons is relatively simple. Studies of the hadron contamination (Chapter 3) suggest that a small fraction of the hadrons are misidentified. The asymmetry for the identified hadrons ($A_{\parallel}^{h^+}$) is shown in Figure 4.7. The correction to the measured asymmetry is small compared to the statistical uncertainty in the raw asymmetry. The hadron contamination ($\frac{h^+}{e^+ + e^- + h^+}$) and hadron asymmetry are included in Table 4.2.1.

Charge Symmetric Contamination

Positrons from decay processes as well as DIS positrons can satisfy the kinematic cuts placed on the data. These extraneous events are expected to be charge symmetric, and it is conventional to make a correction to the positron rate based on the observed electron rate. The charge symmetric contamination is slightly more complicated than the contamination from positive hadrons because the electron rate is
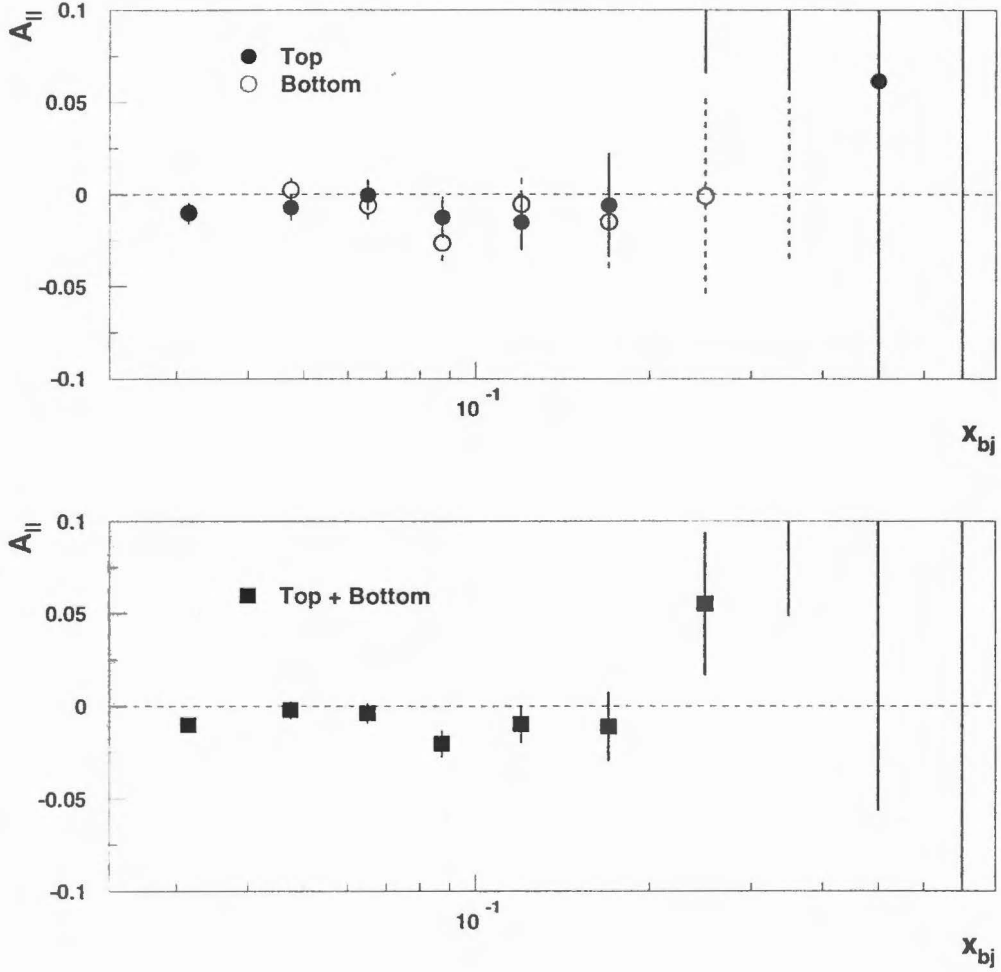
Figure 4.7: Positive Hadron Asymmetry $A_{\parallel}^{h^+}$

x bin	Hadron Contamination	$A_{\parallel}^{h^+}$
1	0.036	-0.0101 ± 0.0290
2	0.025	-0.0183 ± 0.0407
3	0.015	-0.0457 ± 0.0523
4	0.009	-0.1158 ± 0.0742
5	0.004	-0.1398 ± 0.1132
6	0.001	-0.0677 ± 0.2192
7	0.001	0.3293 ± 0.4075
8	0.000	1.3108 ± 0.9312
9	0.000	-0.0069 ± 1.6129

Table 4.10: Corrections for Misidentified Positive Hadrons

x bin	$e^-/(e^+ + e^- + h^+)$	$A_\parallel^{e^-}$
1	4.5%	-0.0101 ± 0.0290
2	1.3%	-0.0183 ± 0.0407
3	0.6%	-0.0457 ± 0.0523
4	0.2%	-0.1158 ± 0.0742
5	0.1%	-0.1398 ± 0.1132
6	0.0%	-0.0677 ± 0.2192
7	0.0%	0.3293 ± 0.4075
8	0.0%	1.3108 ± 0.9312
9	0.0%	-0.0069 ± 1.6129

Table 4.11: Charge Symmetric Background Correction

significantly smaller than the negative hadron rate. As a result, a significant number of the events identified as electrons are in fact misidentified negative hadrons ($\sim 30\%$ in the lowest x bin and the count rate is consistent with the expected misidentified hadrons rate in the upper x bins). A correction for the hadron contamination is included to avoid double counting the hadron background.

$$\frac{e^-}{e^+ + e^- + h^+} = N_{e^-}/N_{e^+} * (1 - C_{h^-}(x)) \tag{4.9}$$

where $\frac{e^-}{e^+ + e^- + h^+}$ represents the corrected contamination; N_{e^-} is the raw number of electrons and $C_{h^-}(x)$ is the negative hadron contamination. The asymmetry measured for the electron candidates is shown in Figure 4.8. As a comparison, the asymmetry for the negative hadrons is shown in Figure 4.9. The two asymmetries are similar and are both slightly negative at small x where the charge symmetric correction is significant. No correction is made to the electron asymmetry for the negative hadron contamination. The correction is very small because the measured asymmetries are similar and the statistical uncertainty in the charge symmetric corrections does not contribute significantly to the total measurement.

The corrections for charge symmetric processes are again small compared to the observed asymmetries. Table 4.11 shows the size of the correction factors for charge symmetric background.
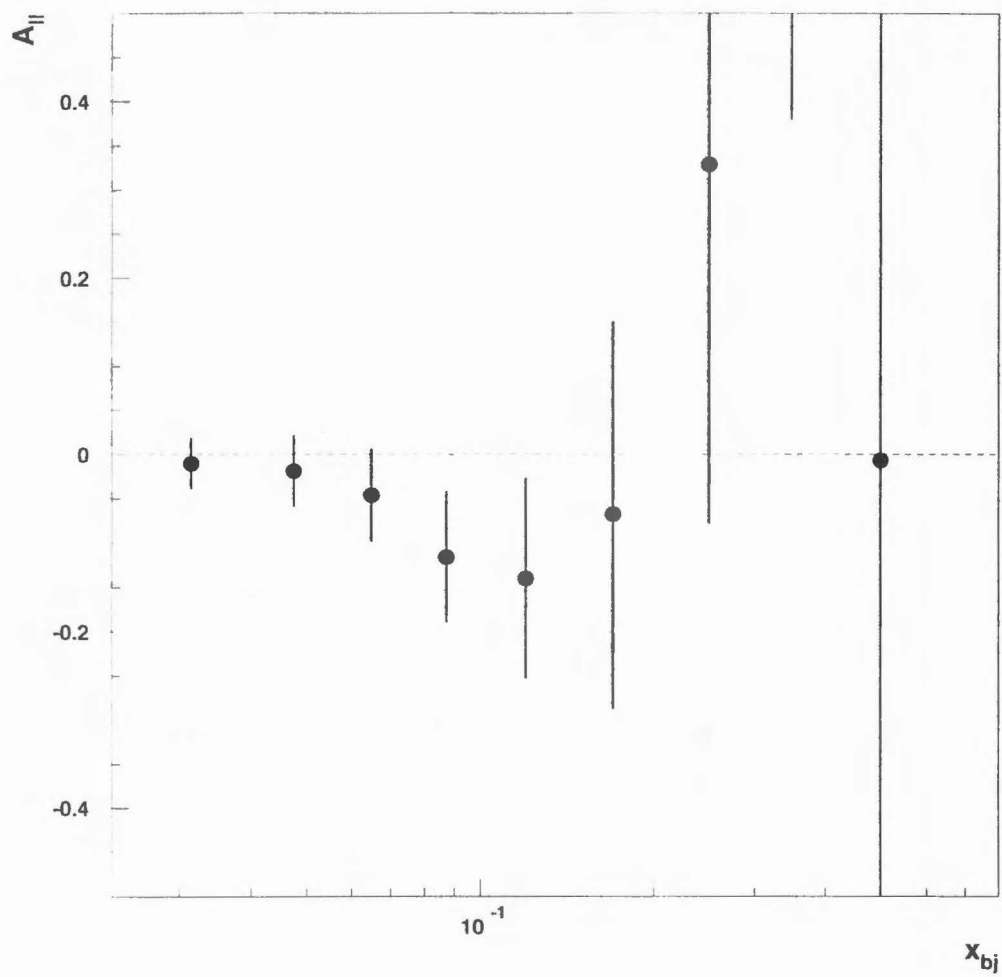
Figure 4.8: Electron Asymmetry
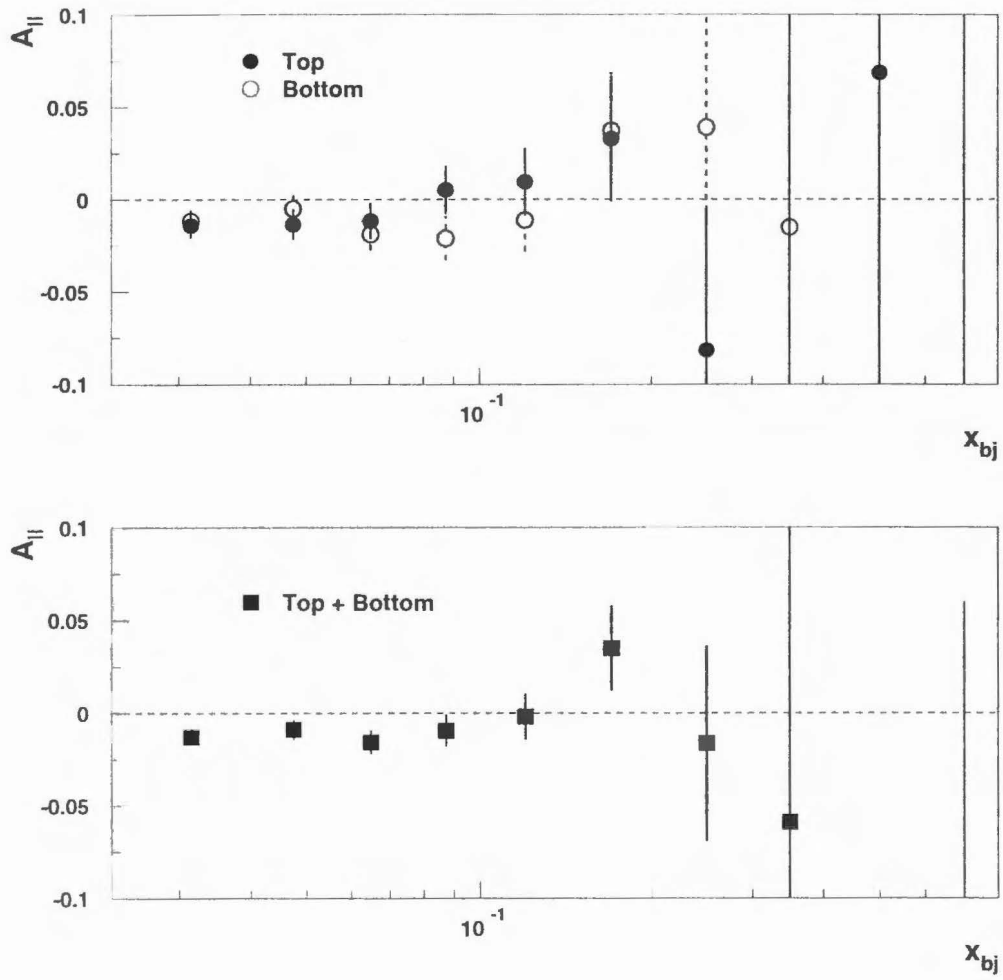
Figure 4.9: Negative Hadron Asymmetry

4.2.2 Radiative Corrections

The formulae used in the discussion of DIS measurements refer to the lowest order diagrams which contribute to the scattering amplitude (Born approximation). Higher order diagrams also contribute to the scattering cross sections and asymmetry. These contributions are referred to as radiative corrections. Elaborate and powerful schemes have been developed to calculate the radiative corrections in DIS scattering. [48] The radiative corrections are traditionally divided into two categories, internal and external.

Internal radiative corrections occur at the primary scattering vertex. Many different processes are included in the internal radiative corrections such as the following:

- Initial (Final) State Bremsstrahlung

- Vertex Corrections

- Vacuum Polarization

- Two Photon Exchange

- Hadron Current Corrections

Feynman diagrams for these processes are shown in Figure 4.10.

Just as the first-order Born process has an asymmetry, the radiative corrections are not symmetric for the two lepton-nucleon spin combinations. The formalism for generating the radiative corrections to spin dependent DIS has been developed previously.

The radiative corrections are calculated with the POLRAD code [49] which has been adapted for the HERMES acceptance and kinematics [50]. The code uses a parameterization of the Schaefer model for $A_1^n(x)$ [51] to model the asymmetry. ΔRC is calculated by radiating the model of A_1^n. The radiative corrections are iterative and the model's parameters are varied until the radiated asymmetry fits the asymmetry calculated from the data. The values and uncertainties of the radiative corrections are tabulated in Table 4.12. The formula for applying the radiative corrections is:

$$A_{Born}^{^3\mathrm{He}} = A_1^{^3\mathrm{He}} - \Delta\mathrm{RC}. \tag{4.10}$$
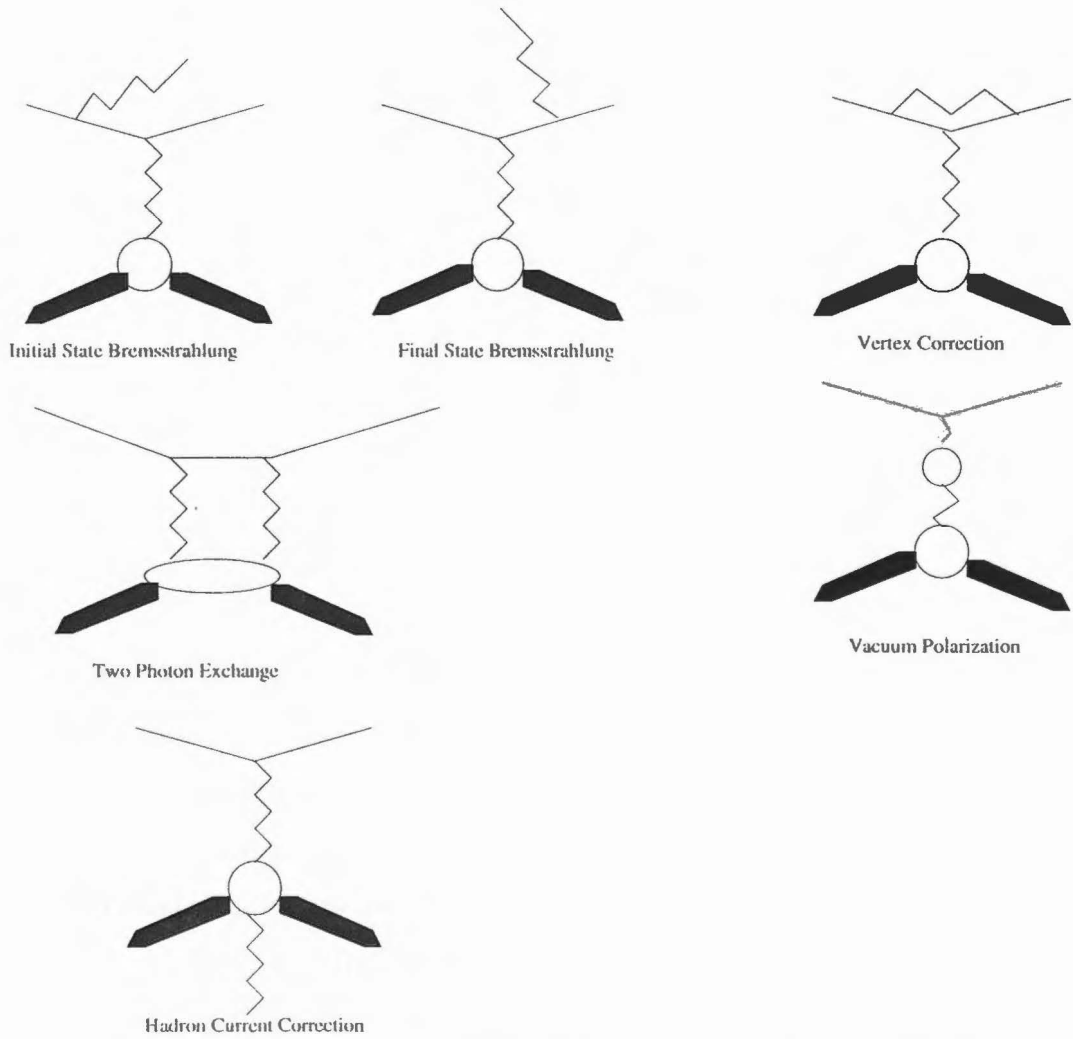
Figure 4.10: Diagrams Which Contribute to the Internal Radiative Corrections

With

$$\Delta \text{RC} = \text{A}_{radiated} - \text{A}_{Born}. \tag{4.11}$$

Studies [52] have estimated the contribution of the radiative corrections to the systematic error. The dominant uncertainties are due to different parameterizations of A_1^n which describe the data.

$< x >$	Radiative Correction	δ RadCorr
0.035	0.0059	0.0029
0.049	0.0051	0.0015
0.066	0.0048	0.0007
0.088	0.0044	0.0005
0.119	0.0042	0.0007
0.168	0.0040	0.0010
0.244	0.0040	0.0013
0.342	0.0040	0.0015
0.464	0.0039	0.0019

Table 4.12: Radiative Corrections for A_1^{3He}

External radiative corrections are the interaction of the positrons with material before and after the scattering nuclei. The HERMES target is very thin and interactions before the scattering can be neglected when calculating the asymmetry A_1^n. Interactions after the scattering vertex change the energy and direction of outgoing tracks. This can shift the binning of the events and 'smear' the asymmetry by averaging different kinematic regions. The HERMES spectrometer is very 'thin', that is, the scattered particles only encounter $\sim 7\%$ of a radiation length before the hodoscopes. So, there is very little multiple scattering and Monte Carlo studies suggest that the effect of smearing can be neglected. [53]

4.2.3 The Measured Asymmetry A_1^{3He}

The values for A_1^{3He} from the top and bottom spectrometer were averaged together for the calculation of A_1^n and g_1^n. The results for the two spectrometers can be seen in Figure 4.11. The difference of the two spectrometers is $2\ \sigma$ for the two lowest x points, but the χ^2/df is 1.2 for the nine points which has a confidence level of 20%.
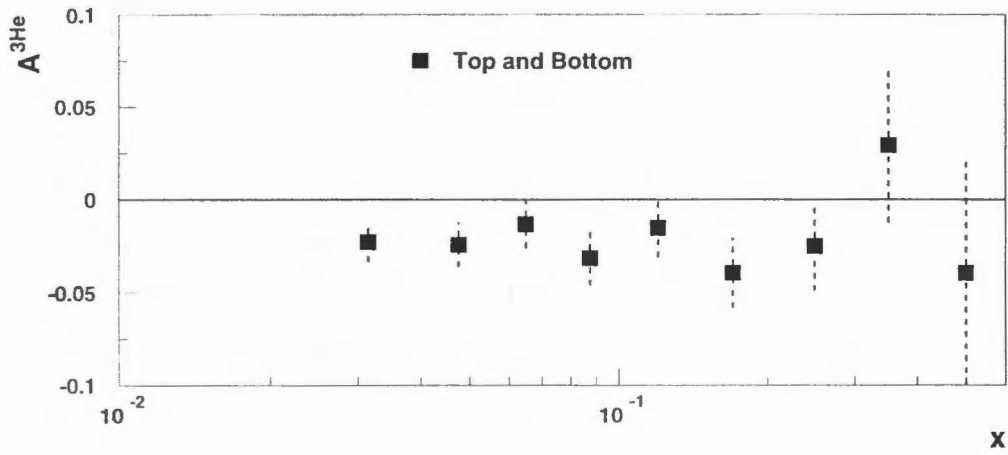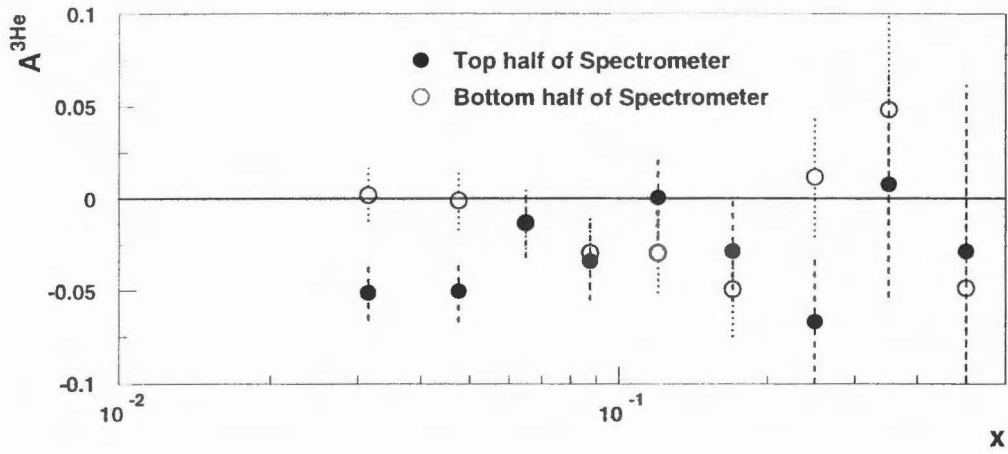
Figure 4.11: A_1^{3He} Versus x
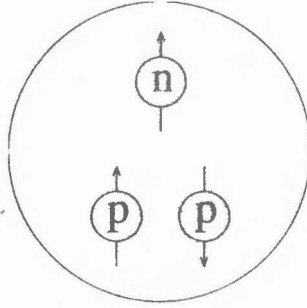
Figure 4.12: Primary Part of ^3He Wave Function

Partial Wave	L	S	P_n^+	P_n^-	P_p^+	P_p^-	%
S	0	1/2	1	0	1	1	88.6
S'	0	1/2	2/3	1/3	4/3	2/3	1.54
D	2	3/2	1/3	2/3	2/3	4/3	8.37

Table 4.13: Partial Wave Decomposition of ^3He

4.3 Extracting A_1^n

It is not feasible to use a free neutron target for DIS experiments. Unlike the proton structure functions, neutron structure functions are measured with a multi-nucleon nucleus. Experiments using polarized D or ^3He can be used to extract A_1^n since simple models relate the spin of the nucleus to the spins of the nucleon constituents. These nuclear effects must be taken into account in the calculation of neutron structure functions. In 1995 a polarized ^3He target was operated in the spectrometer, and this discussion will focus on extracting A_1^n from $A_1^{^3He}$.

The observation that the spin of the neutron dominates the spin of the ^3He nucleus has motivated the use of polarized ^3He targets to measure neutron spin structure functions. In the simplest model of ^3He, the nucleons are in a spatially symmetric S state and the Pauli principle constrains the protons to be paired antisymmetrically in a spin singlet. Figure 4.3 shows this contribution. A more realistic model [54] suggests that this is the dominant portion of the wave function with small contributions from S' and D states. Table 4.13 shows the contributions of the S, D and S' state which has a mixed spin and isospin symmetry.

A best fit to the results from many different models of nucleon - nucleon interac-

tions [55] [56] suggests that the polarized ^3He can be described as a slightly depolarized neutron with a small component of proton polarization opposite the direction of the nuclei's spin.

$$p_n = 0.86 \pm 0.02 \tag{4.12}$$

$$p_p = -0.028 \pm 0.004 \tag{4.13}$$

and the asymmetry of the helium nucleus can be written [56]:

$$A_1^{^3He}(x) = \frac{F_2^n(x)}{F_2^n(x) + 2F_2^p(x)} p_n A_1^n(x) + \frac{F_2^p(x)}{F_2^n(x) + 2F_2^p(x)} p_p A_1^p(x) \tag{4.14}$$

where A_1^p is the virtual photon spin asymmetry for the proton and F_2 is the spin independent structure function. Values for F_2 are obtained from fits to experimental data [57] and A_1^p from the previous E143 measurement [5].

4.3.1   The Measured Asymmetry A_1^n

The virtual photon asymmetry A_1^n can now be extracted from the data using Equation 4.14. The results for the top and bottom spectrometer have been averaged and a total asymmetry for the experiment was calculated. The results for A_1^n are shown in Figure 4.13 and tabulated in Table 4.14. The E142 [4] results with statistical errors are shown in Figure 4.13 for comparison.

$< x >$	Average $A_1^{^3He} \pm$stat.	$A_1^n \pm$stat.
0.035	-0.0245 ± 0.0111	-0.1045 ± 0.0411
0.049	-0.0265 ± 0.0121	-0.1098 ± 0.0450
0.066	-0.0180 ± 0.0129	-0.0758 ± 0.0483
0.088	-0.0311 ± 0.0148	-0.1232 ± 0.0566
0.119	-0.0240 ± 0.0158	-0.0953 ± 0.0631
0.168	-0.0391 ± 0.0187	-0.1563 ± 0.0785
0.244	-0.0208 ± 0.0236	-0.0748 ± 0.1057
0.342	$+0.0239 \pm 0.0408$	$+0.1478 \pm 0.1981$
0.464	-0.0391 ± 0.0604	-0.1560 ± 0.3270

Table 4.14: A_1^n and $A_1^{^3He}$: Top and Bottom Averaged
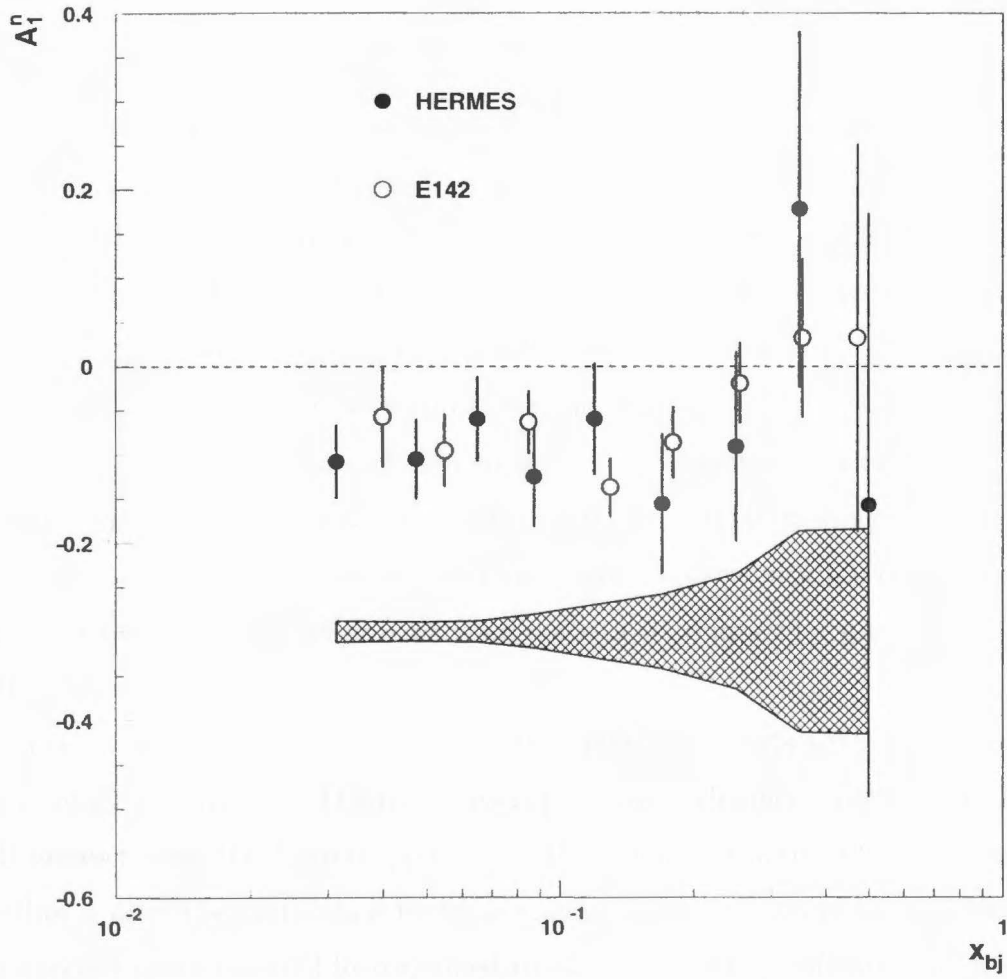
Figure 4.13: A_1^n Versus x With Systematic Errors (Solid Band)

4.4 Systematic Studies of the Asymmetry

4.4.1 Time Stability of the Asymmetry

The g_1^n analysis was performed on a fill by fill basis. Within fills the luminosity was stable and an average of the fill based asymmetries was used to calculate the physics asymmetries. The time dependence between fills and within fills was used to check the stability of the analysis.

The asymmetry ($A_{||}$) over the entire x range (from 0.023 to 0.6) is used for these studies. The statistical errors on the measurements of $A_{||}$ for positrons and positive hadrons are similar, and the error for negative hadrons is slightly larger. Within fills, the asymmetry is calculated for groups of five runs which represents about fifty minutes of data and averaged to calculate an asymmetry per fill. The χ^2 for the asymmetries with a fill are used to calculate a confidence level that the data are statistically distributed within each fill, and the asymmetries per fill are fit to a constant to observe the time stability for the full experiment.

Groups of five runs were chosen to include at least two sets of data in each spin state so the statistics in each spin state would be roughly balanced. There were not enough statistics to calculate a meaningful time dependence for the electrons while the positrons and hadrons provide good statistical accuracy for groups of five run and fills.

The total asymmetries per fill and the confidence levels with the fills are shown in Figures 4.14 to 4.19. The top of each plot shows the measured asymmetry versus fill number, and the bottom plots show the confidence levels of the groups of runs within a fill. The confidence levels are shown versus fill number to show fills with low confidence levels and histogramed to show the total confidence level distribution which should have a uniform density.

The per fill confidence level suggest that there are no large non-statistical effects within a fill. The distributions of confidence levels should be flat. The time stability for the total fills is slightly worse. The asymmetry should be constant versus time, but the χ^2 per degree of freedom for this hypothesis are somewhat higher than would be expected. None of the value of χ^2 per degree of freedom is below a 1% confidence

level, but three of six confidence levels are under 10%.

4.4.2 The Determination of the Statistical Errors

Although there is no large time dependence in the HERMES analysis, additional studies were performed on the yield distributions to check that the data was statistically distributed.

The yields cannot be compared directly because there are large ($\sim 10\%$) variations in the yield from fill to fill as shown in Figure 4.20. The variations in yield can have many causes including variations in the tracking chamber efficiency effecting the count rate and variations in the gain or position of the luminosity monitor. It should be noted that between fills the detector is completely turned off and the luminosity monitor and calorimeter are moved away from the beam pipe. In addition, the time between fills can be from hours to days. Since the efficiencies of the top and bottom chambers are highly correlated, either of these effects could produce the top-bottom correlations evident in Figure 4.20.

Figure 4.21 shows the yield of every good run compared to the mean yield for that fill normalized by the statistical uncertainty of the run. The expected width of this distribution is 1.0. The observed distributions suggest that the fluctuations are slightly larger than expected. The statistical uncertainty in the yield is $\sim 4\%$ per run, and the observed widths suggest there is an additional fluctuation on the order of 1% per run in the yield. This may be due to the 1% raw asymmetry ($A_{\parallel}$) or the 1% variation in the yield observed as a function of current although the effect is slightly larger than would be expected for these effects.

Additional studies by the European analysis group [58] suggested that this effect may be due to additional statistical fluctuations larger than expected from the number of observed positrons. The results of these studies are equivocal as the stability of the asymmetry per fill suggests there is a small additional effect while the studies of shorter time scales show either no effect (asymmetries for groups of five runs) or a small effect (the yield per run). For further discussion see Appendix B.
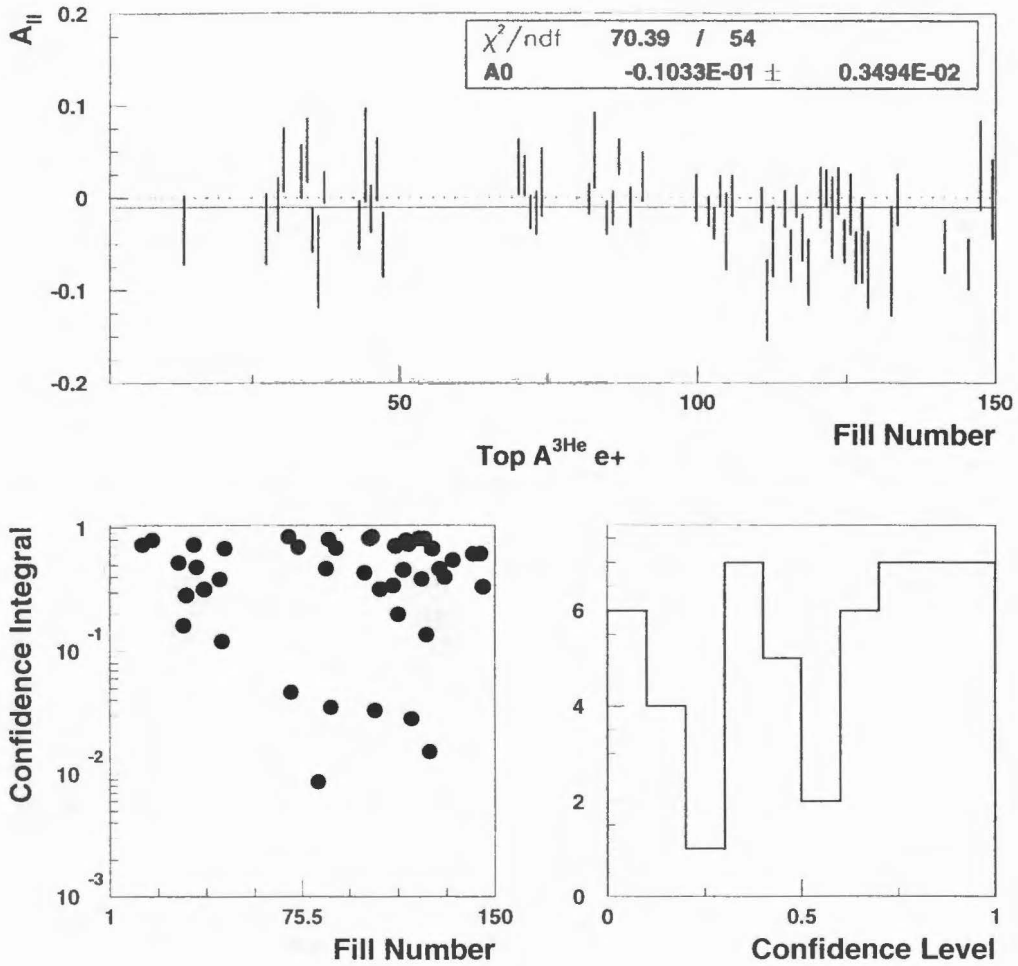
Figure 4.14: Time Dependence Plots for Positrons in the Top Detector: The asymmetry per fill versus fill number, the confidence level of sets of runs within each fill, and the distribution of the confidence levels
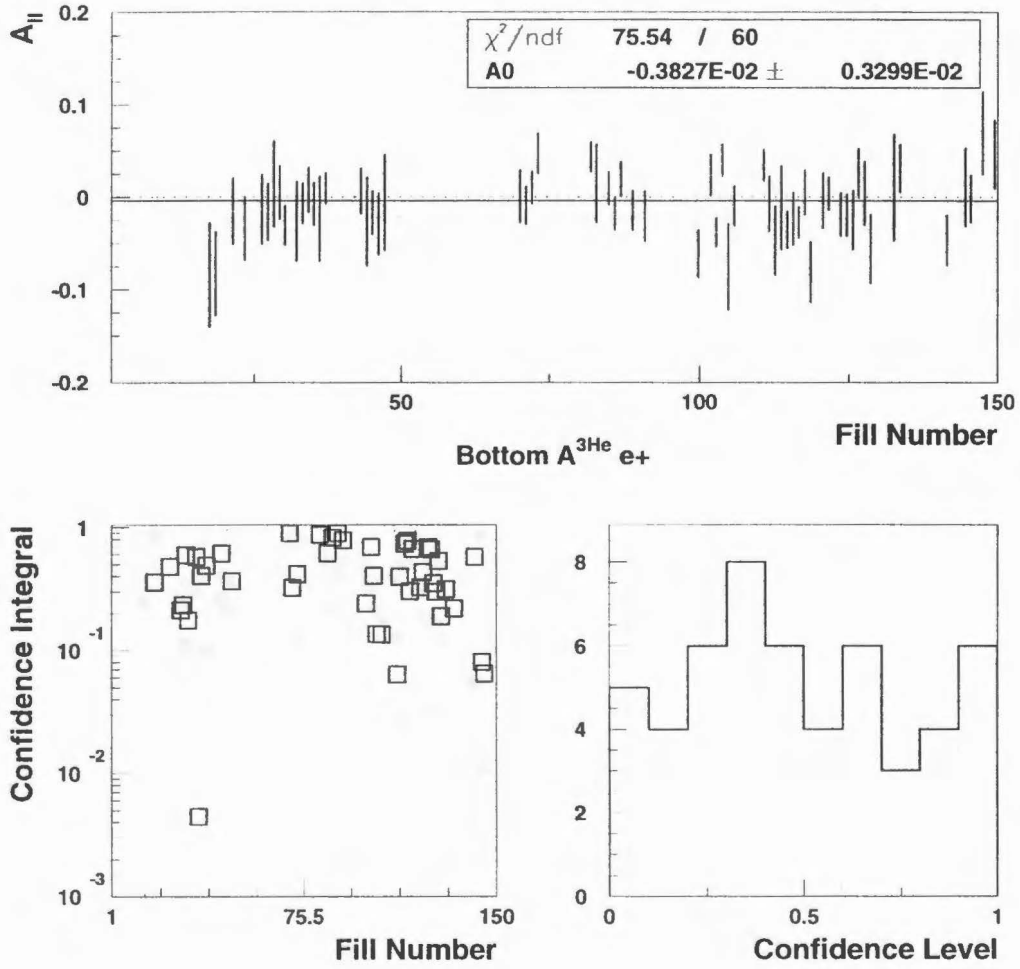
Figure 4.15: Positron Time Dependence Bottom Detector as Defined in Figure 4.14
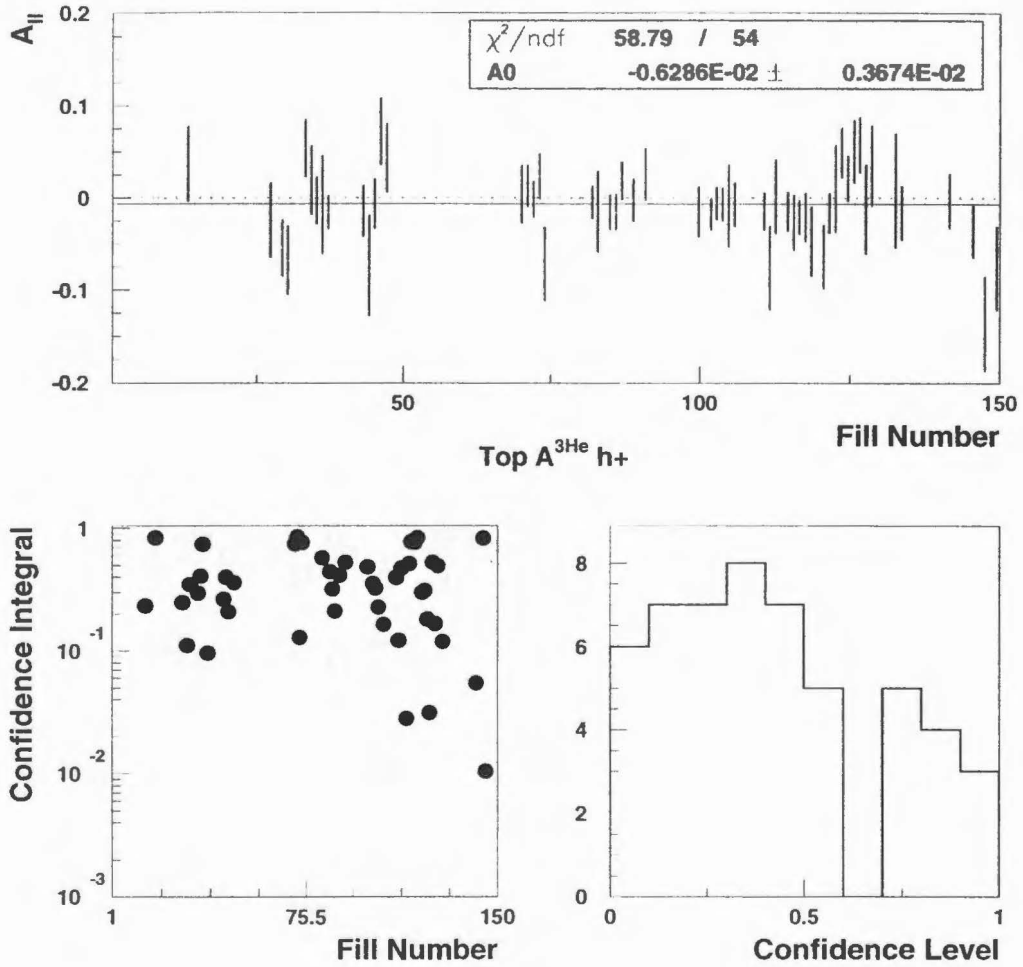
Figure 4.16: Positive Hadron Time Dependence Top Detector as Defined in Figure 4.14
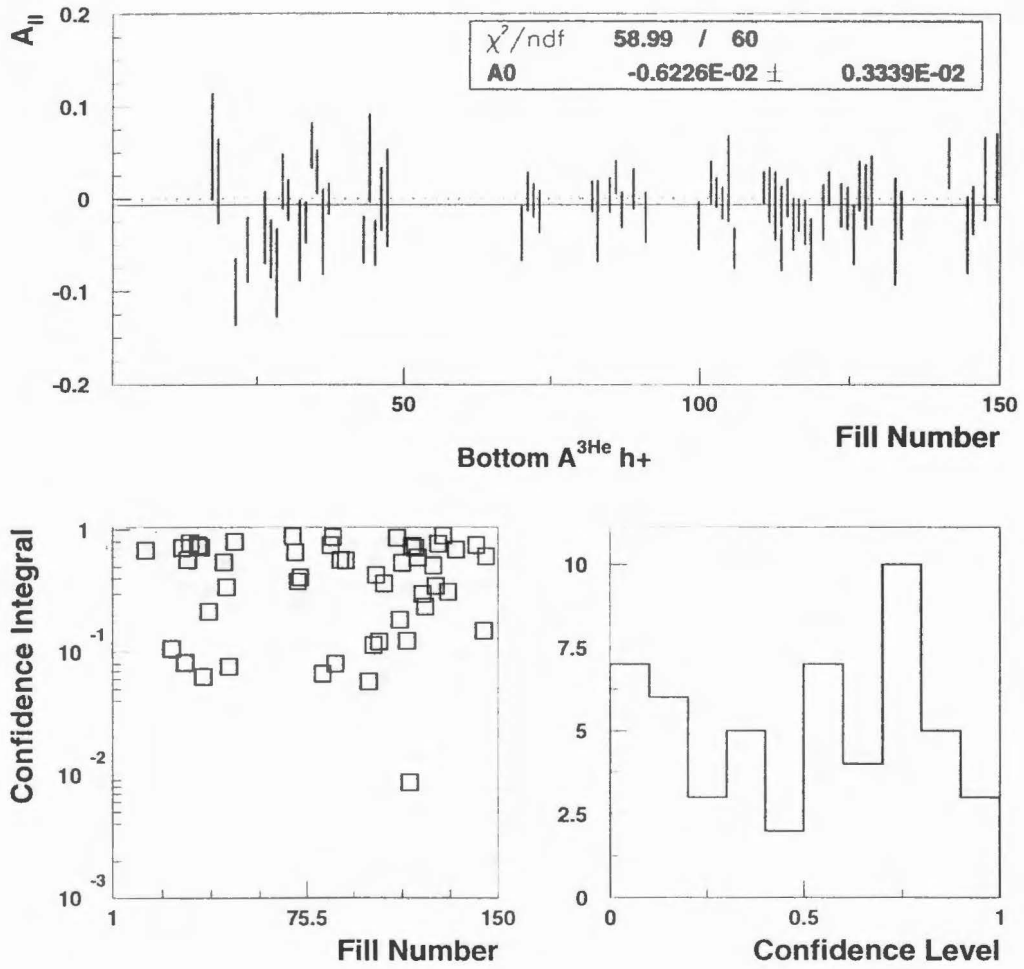
Figure 4.17: Positive Hadron Time Dependence Bottom Detector as Defined in Figure 4.14
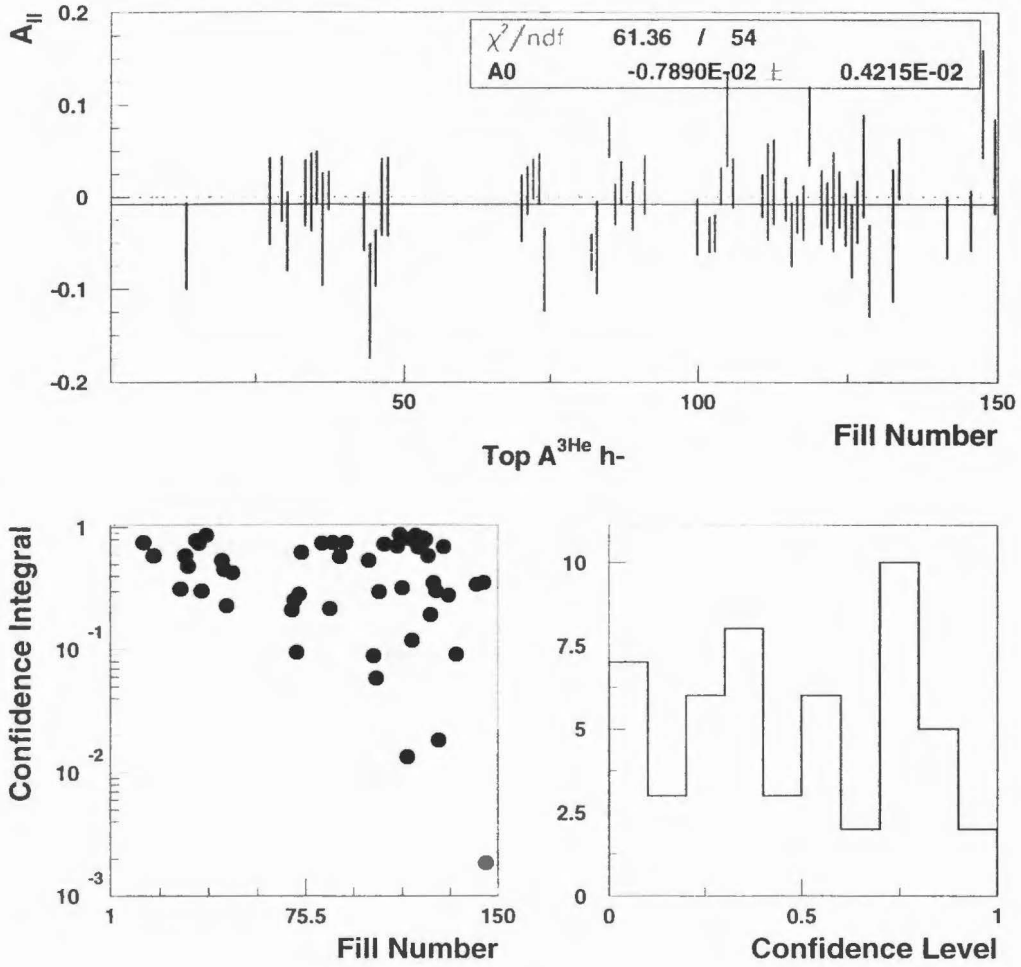
Figure 4.18: Negative Hadron Time Dependence Top Detector as Defined in Figure 4.14
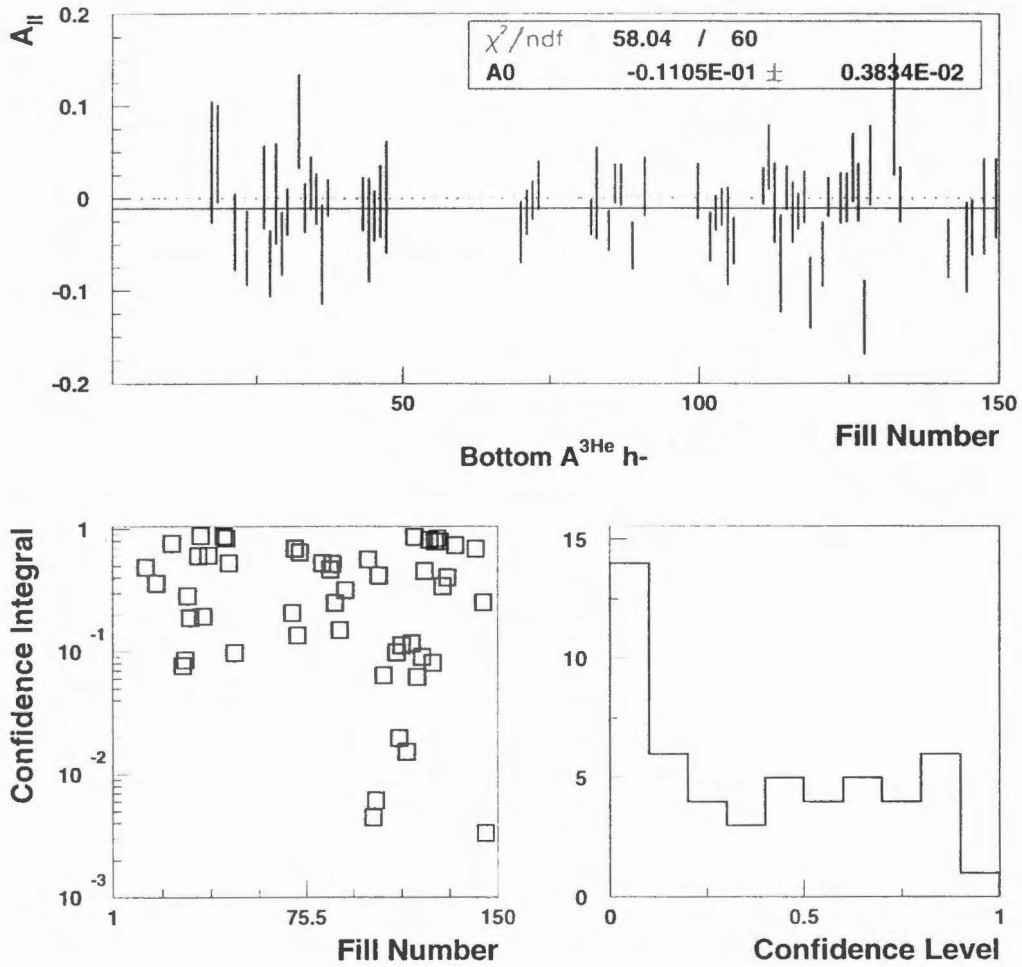
Figure 4.19: Negative Hadron Time Dependence Bottom Detector as Defined in Figure 4.14
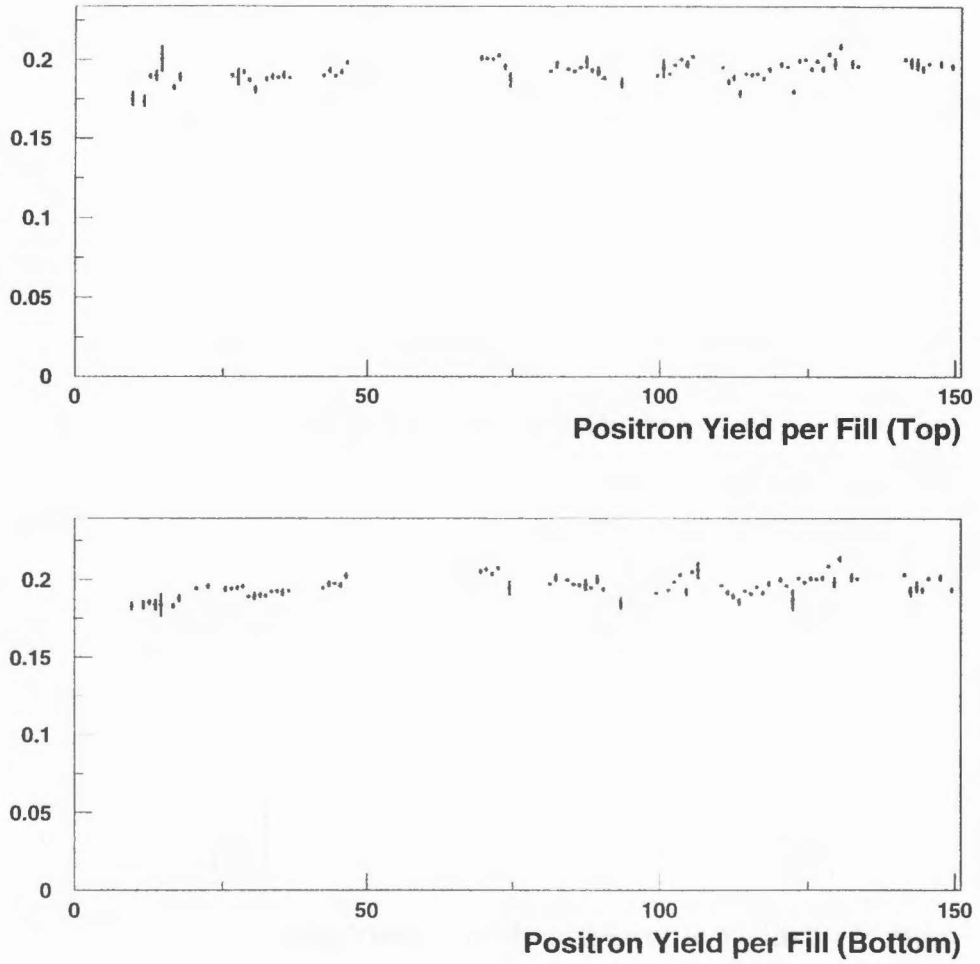
Figure 4.20: Positron Yield Versus Fill for the Top and Bottom Detectors
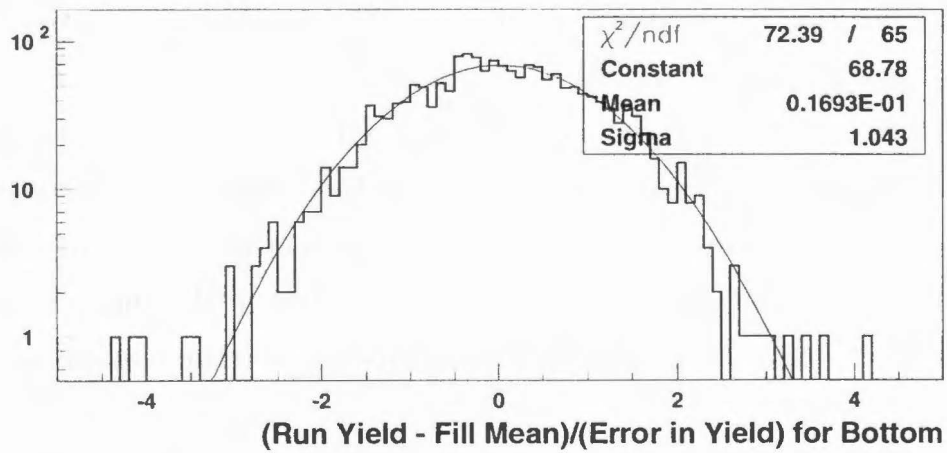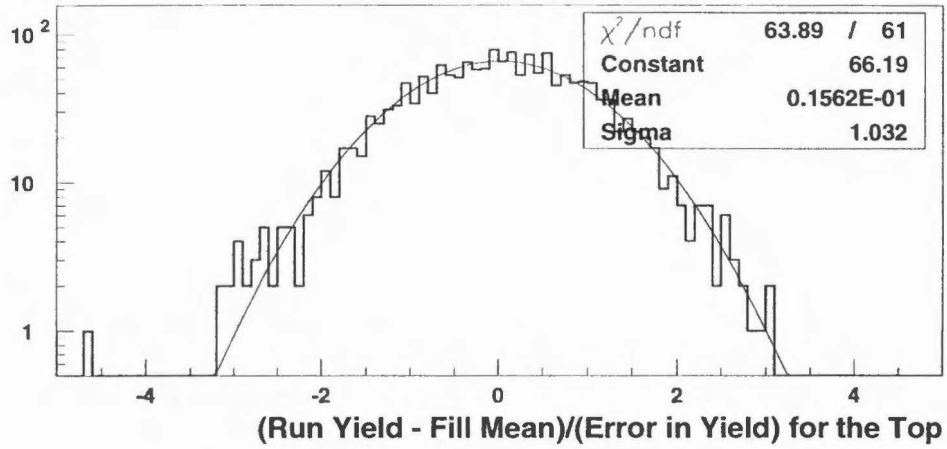
Figure 4.21: Fluctuations in Positron Yield: Top and Bottom
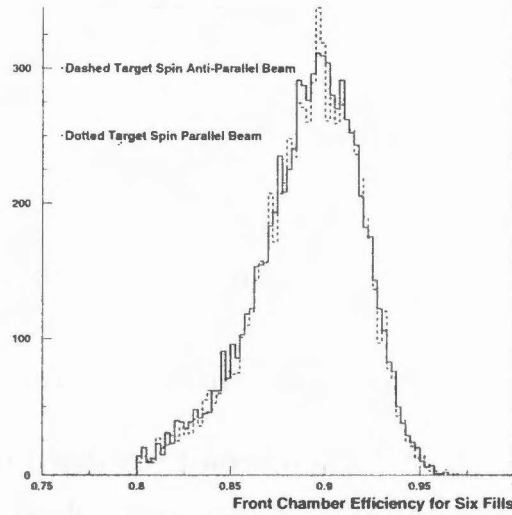
Figure 4.22: —Efficiency Distribution Used in False Asymmetry Checks

4.4.3 False Asymmetries

The rapid flipping (every ten minutes) of the target should average over any false asymmetries. Any properties of the experiment which change on a time scale longer than the spin flip should not contribute to any false asymmetry. Numerous tests did not observe correlations with the spin flip of the target which could produce a false asymmetry. All quantities such as the chamber efficiencies, particle identification response and luminosity monitor rate as a function of current were studied carefully and were found to be independent of the spin state. One of the chamber efficiency distributions as a function of target spin is shown in Figure 4.22.

4.5 Extracting g_1^n

The relation of g_1^n to A_1^n was discussed in Chapter 1. The structure function g_1^n can now be calculated from Equation 1.41 (assuming $A_2^n = 0$):

$$g_1^n = \frac{F_2^n}{2x(1+R)} \frac{A_\parallel^n}{D}.$$

The unpolarized structure function F_2 and the ratio of longitudinal to transverse virtual photon cross sections (R) are required to calculate A_1^n and g_1^n. Neither quantity is measured in the present experiment but fits to previous data exist for both F_2 [57] and R [59]. The value of F_2^n is determined by

$$F_2^n = 2 \cdot F_2^d - F_2^p. \tag{4.15}$$

The results at the measured Q^2 are displayed in Figure 4.23.

4.5.1 Evolving the Structure Function g_1^n to Constant Q^2

The measured structure function is evolved to constant Q^2 to compare with theoretical predictions which are made at constant Q^2. No Q^2 dependence of A_1^n has been observed over the Q^2 range which is relevant for HERMES [60]. As a result, the structure function g_1^n is evolved by assuming A_1^n is not a function of Q^2 and evolving with $F_2^n(x, Q^2)$ and $R(x, Q^2)$.

The results are evolved to a constant Q^2 of 2.5 $[Gev/c]^2$ and plotted in Figure 4.24 and tabulated in Table 4.15.

$< x >$	$R(Q^2 = 2.5)$	$F_2^n(Q^2 = 2.5)$	$g_1^n \pm$stat.$\pm$syst.
0.035	0.3115	0.3326	$-0.3895 \pm 0.1490 \pm 0.059$
0.049	0.3036	0.3259	$-0.2810 \pm 0.1148 \pm 0.032$
0.066	0.2924	0.3180	$-0.1406 \pm 0.0901 \pm 0.015$
0.088	0.2775	0.3079	$-0.1676 \pm 0.0776 \pm 0.019$
0.119	0.2585	0.2936	$-0.0922 \pm 0.0619 \pm 0.011$
0.168	0.2363	0.2708	$-0.1005 \pm 0.0512 \pm 0.012$
0.244	0.2168	0.2326	$-0.0281 \pm 0.0414 \pm 0.006$
0.342	0.2050	0.1792	$+0.0331 \pm 0.0431 \pm 0.005$
0.464	0.1984	0.1175	$-0.0165 \pm 0.0345 \pm 0.003$

Table 4.15: $g_1^n(x, Q^2 = 2.5[GeV/c]^2)$

4.5.2 Measured Integral of $g_1^n(x, Q^2 = 2.5(GeV/c)^2)$

The integral of the neutron spin structure function, $\int g_1^n(x, Q^2)dx$, is of fundamental interest since it appears in tests of the Bjorken and Ellis-Jaffe sum rules. We evaluate the integral at a fixed $Q^2 = 2.5(GeV/c)^2$. The integral in the measured region is:

118
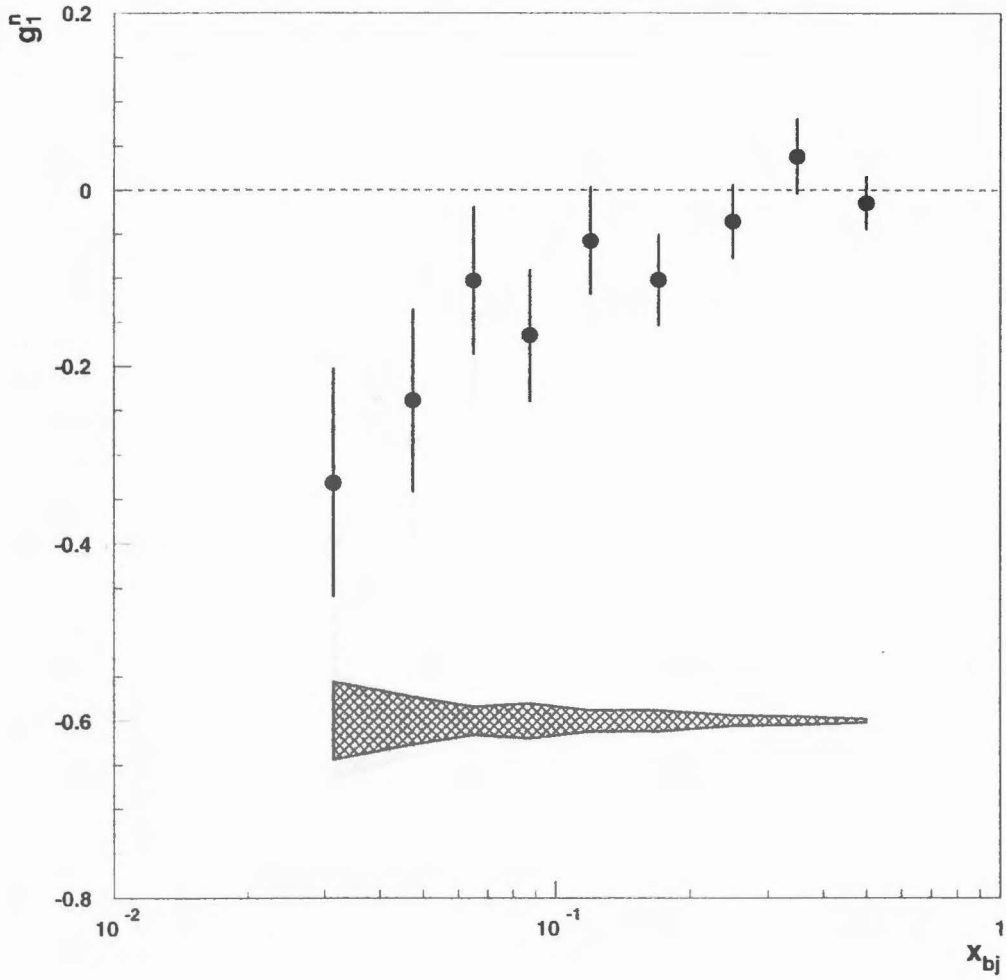
Figure 4.23: g_1^n vs x at Measured Q^2 With Systematic Errors (Solid Band)
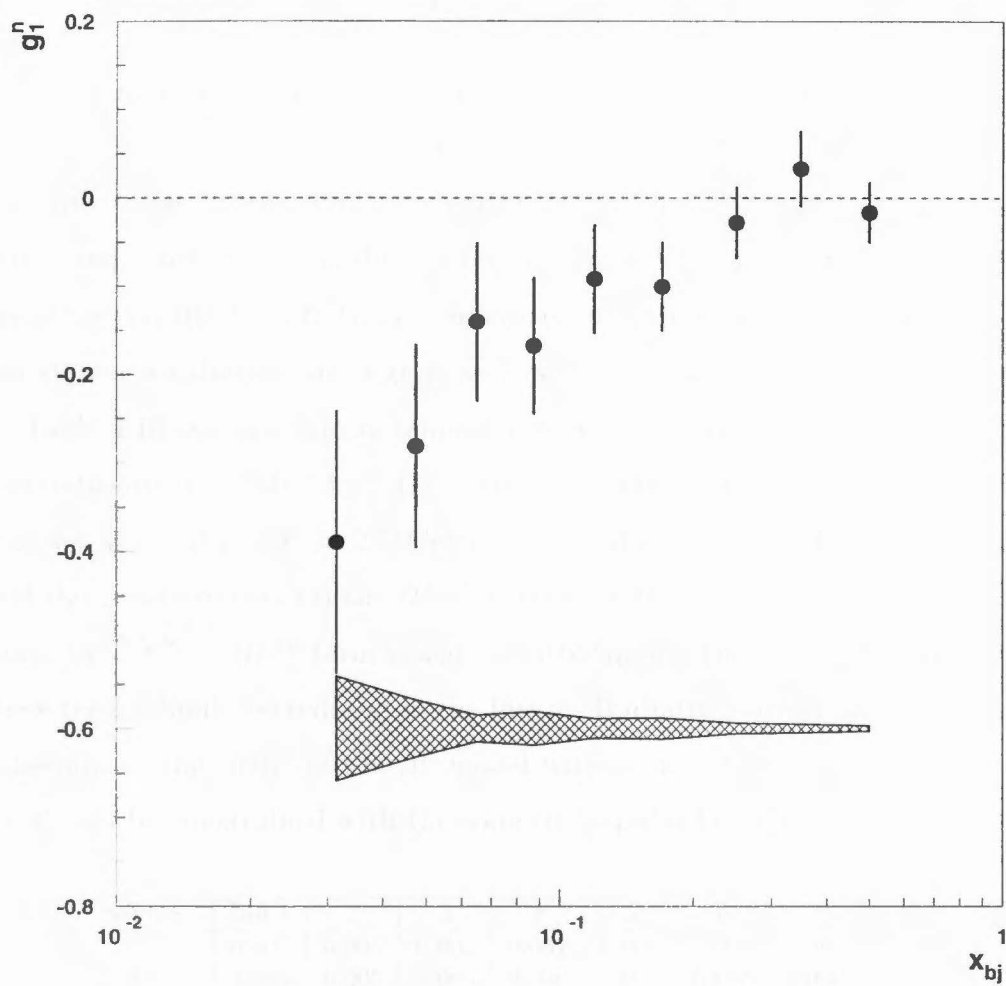
Figure 4.24: g_1^n vs x at Constant Q^2 With Systematic Errors (Solid Band)

$$\int_{0.023}^{0.8} g_1^n(x)\, dx = \sum_{bins} g_1^n\, \Delta x = -0.034 \pm 0.012, \qquad (4.16)$$

where the sum is over the nine data points and the Δx are the bin widths. The statistical errors are added in quadrature since they are uncorrelated from one bin to the next.

4.6 Dominant Systematic Errors

The systematic errors for g_1^n are much smaller than the statistical errors due to poor beam delivery in 1995. It is still important to investigate the contributions of the quantities that dominate the systematic errors in A_1^n and g_1^n. The total systematic errors and contributions of the components to each error are summarized here. There are other contributions to the systematic error such as the uncertainties in A_1^p and F_2^n but these contributions are significantly smaller than the errors which are tabulated.

Table 4.16 contains the systematic errors for A_1^n which are dominated by the uncertainties in A_2^n. Table 4.17, the systematic errors for g_1^n(Measured Q^2), and Table 4.18 for g_1^n(Evolved $Q^2 = 2.5(GeV/c)^2$)) are dominated by the uncertainties in A_2^n and the radiative corrections. The uncertainty in A_2^n is not as significant for g_1^n because the $(\frac{\sqrt{Q^2}}{\nu} - \eta)A_2^n$ term is significantly smaller than the ηA_2^n term in A_1^n. Both these terms should be reduced in the future. Radiative corrections can be reduced by constraining the shape of the A_1^n model with better statistics. The uncertainty due to A_2^n can be constrained with the soon to be published E154 data [61].

Source	Bin 1	2	3	4	5	6	7	8	9
P_b	0.005	0.005	0.003	0.007	0.003	0.009	0.007	0.008	0.012
P_t	0.005	0.005	0.003	0.006	0.003	0.008	0.006	0.007	0.011
$RadCorr$	0.011	0.006	0.003	0.002	0.003	0.004	0.006	0.007	0.010
A_2^n	0.007	0.008	0.011	0.016	0.028	0.040	0.064	0.114	0.114
R	0.005	0.006	0.003	0.007	0.003	0.009	0.005	0.006	0.007
p_n	0.003	0.003	0.001	0.003	0.001	0.004	0.002	0.004	0.004
p_p	0.001	0.001	0.001	0.002	0.003	0.004	0.006	0.008	0.011
Total	0.016	0.014	0.012	0.020	0.029	0.043	0.065	0.115	0.117

Table 4.16: Systematic Errors on $A_1^n(x)$ at the Measured Q^2

Source	Bin 1	2	3	4	5	6	7	8	9	Integral
P_b	0.016	0.012	0.005	0.009	0.003	0.005	0.002	0.002	0.001	0.002
P_t	0.015	0.011	0.005	0.008	0.003	0.005	0.002	0.002	0.001	0.002
$RadCorr$	0.033	0.013	0.005	0.003	0.003	0.003	0.002	0.002	0.001	0.002
A_2^n	0.028	0.015	0.010	0.009	0.009	0.006	0.004	0.003	0.002	0.003
R	0.014	0.007	0.002	0.002	0.000	0.000	0.000	0.000	0.000	0.001
p_n	0.008	0.006	0.002	0.004	0.001	0.002	0.001	0.001	0.000	0.001
p_p	0.002	0.002	0.002	0.003	0.003	0.003	0.002	0.002	0.001	0.001
Total	0.051	0.026	0.014	0.016	0.011	0.011	0.006	0.005	0.003	
Contrib. To int. (%)	0.086	0.040	0.027	0.039	0.042	0.065	0.063	0.047	0.050	0.005 (abs)

Table 4.17: Systematic Errors on $g_1^n(x)$ at the Measured Q^2

Source	Bin 1	2	3	4	5	6	7	8	9	Integral
P_b	0.020	0.013	0.005	0.009	0.003	0.005	0.002	0.002	0.001	0.002
P_t	0.018	0.012	0.005	0.008	0.003	0.005	0.002	0.002	0.001	0.002
$RadCorr$	0.039	0.014	0.005	0.003	0.003	0.003	0.002	0.002	0.001	0.002
A_2^n	0.033	0.016	0.011	0.009	0.009	0.006	0.004	0.003	0.002	0.003
R	0.014	0.007	0.002	0.002	0.000	0.000	0.000	0.001	0.000	0.001
p_n	0.009	0.006	0.003	0.004	0.001	0.002	0.001	0.001	0.000	0.001
p_p	0.003	0.003	0.003	0.003	0.003	0.002	0.002	0.002	0.001	0.001
Total	0.059	0.029	0.015	0.016	0.011	0.011	0.006	0.005	0.003	
Contrib. To int. (%)	0.101	0.044	0.029	0.040	0.043	0.064	0.062	0.048	0.057	0.005 (abs)

Table 4.18: Systematic Errors on $g_1^n(x)$ at $Q^2 = 2.5 GeV^2$

4.6.1 Cut Dependence of the Measured Integral of $g_1^n(x)$

The many cuts detailed in the analysis select the data which is used for the analysis and, thus, the measured asymmetry. The effect of these cuts was studied by varying the cuts over a range where the time dependence was reasonable. That is, the χ^2/df for the asymmetry per fill was approximately the same as that for the standard cuts. Within this reasonable range, varying the cuts had little effect on the measured asymmetry or the integral $\int_{0.023}^{0.6} g_1^n(x)dx$. The variation in calculated asymmetries from these studies is smaller than the systematic errors from the inputs to the calculation of g_1^n. As a result, no additional systematic error has been assigned for the cut dependence. The integral had the strongest dependence on the front chamber total efficiency cut and the results for variations of this cut are shown in Table 4.19.

Efficiency	e^+ χ^2/df	h^+ χ^2/df	h^- χ^2/df	$\int_{0.023}^{0.6} g_1^n$
10%	0.97	1.44	1.54	-0.033
	1.24	1.01	1.37	± 0.010
40%	0.85	1.56	1.41	-0.031
	1.24	0.98	1.43	± 0.010
80%	0.81	1.71	1.62	-0.032
	1.64	1.12	1.48	± 0.010
85%	0.61	1.61	1.40	-0.028
	1.28	0.95	1.23	± 0.011

Table 4.19: Front Chamber Total Tracking Efficiency Cut Dependence

4.7 Comparison to Theory

In order to compare the results of the experiment to theoretical predictions, it is necessary to extrapolate g_1^n into the unmeasured regions of x between 0 and 0.023 and 0.6 and 1.0. These extrapolations will be discussed next.

4.7.1 Low x Extrapolation

The integral in the unmeasured region, $0 < x < 0.023$, is estimated by assuming a Regge-like behavior [62] [63] [64], $g_1(x- > 0) = x^{-\alpha}$, where the Regge intercept α can vary from $-0.5 < \alpha < 0$. In this region sea and gluon contributions dominate the nucleon structure, and it is generally assumed that no difference should exist between proton and neutron behavior.

$$\int_0^{0.023} g_1^n(x)\,dx = \int_0^{0.023} A x^{-\alpha}\,dx \qquad (4.17)$$

Using the leading logarithmic intercept value of $\alpha = 0$ and fitting the data in the two lowest x bins, we obtain an integral of

$$\int_0^{0.023} g_1^n(x)\,dx = -0.005 \pm 0.005. \qquad (4.18)$$

A 100 % uncertainty has been assumed in this extrapolation.

Recent work [65] indicates that an NLO treatment of the low x region could yield different, significantly more negative results for the low x extrapolation. An NLO

treatment of the extrapolation has not been performed and the Regge-like extrapolation is consistent with previous extrapolations [4].

4.7.2 High x Extrapolation

To determine the integral at high x (> 0.6), we estimate A_1^n and the contribution to the integral. There are theoretical reasons to believe that A_1^n goes to 1 as x approaches 1 [66].

The high x contribution to g_1^n is then determined by assuming that A_1^n is positive. A constant value of $A_1^n = 0.5 \pm 0.5$ is used for $x > 0.6$ in the extrapolation. The x dependence of F_2^n is obtained from the parameterization of the NMC proton and deuteron data [57].

This produces a total high x extrapolation of

$$\int_{0.6}^{1} g_1^n(x)\, dx = 0.003 \pm 0.003. \tag{4.19}$$

4.7.3 Total Integral of $g_1^n(x, Q^2 = 2.5(GeV/c)^2$

Combining all of the previous results, we find

$$\Gamma_n^1 = \int_0^1 g_1^n(x, Q^2 = 2.5)\, dx = -0.036 \pm 0.012 \pm 0.005 \pm 0.006 \tag{4.20}$$

where the errors are statistical, systematic, and extrapolation. This result at constant Q^2 can now be compared to the Q^2 evolved values of the structure function sum rules.

4.7.4 The Ellis - Jaffe Sum Rule

The Ellis - Jaffe sum rule (Section 1.5) predicts

$$\Gamma_1^n = -\frac{1}{12}(F + D)C_{ns} + \frac{1}{36}(3F - D)C_{ns} + \frac{1}{9}(3F - D)C_s. \tag{4.21}$$

At $< Q^2 >$ of $(2.5GeV/c)^2$ the QCD corrections take the values

$$C_{ns} = 1 - \left(\frac{\alpha_s(Q^2)}{\pi}\right) - 3.5833\left(\frac{\alpha_s(Q^2)}{\pi}\right)^2 - 20.2153\left(\frac{\alpha_s(Q^2)}{\pi}\right)^3 = 0.8506 \qquad (4.22)$$

$$C_s = 1 - \frac{1}{3}\left(\frac{\alpha_s(Q^2)}{\pi}\right) - 0.5495\left(\frac{\alpha_s(Q^2)}{\pi}\right)^2 = 0.9624 \qquad (4.23)$$

and the sum rule has the theoretical value

$$\Gamma_1^n = -\frac{1}{12}(F + D)C_{ns} + \frac{1}{36}(3F - D)C_{ns} + \frac{1}{9}(3F - D)C_s = -0.013 \pm 0.005. \quad (4.24)$$

This falls two sigma outside of the present measurement.

4.7.5 The Bjorken Sum Rule

Using the E143 proton result of [5]

$$\Gamma_1^p(Q^2 = 2.5(GeV/c)^2) = 0.130 \pm 0.011. \qquad (4.25)$$

The value obtained for the Bjorken sum rule is

$$\Gamma_1^p(Q^2 = 2.5(GeV/c)^2) - \Gamma_1^n(Q^2 = 2.5(GeV/c)^2) = 0.166 \pm 0.016. \qquad (4.26)$$

The theoretical expectation is (Section 1.5) 0.165 ± 0.005.

Thus, the HERMES data combined with the results of E143 is in excellent agreement with the theoretical prediction of the Bjorken sum rule.

This confirms previous results suggesting that the Ellis-Jaffe sum rules are violated while the Bjorken sum rule is satisfied. The values of Γ_1^n and Γ_1^p can be used to extract the spin contribution of the quarks.
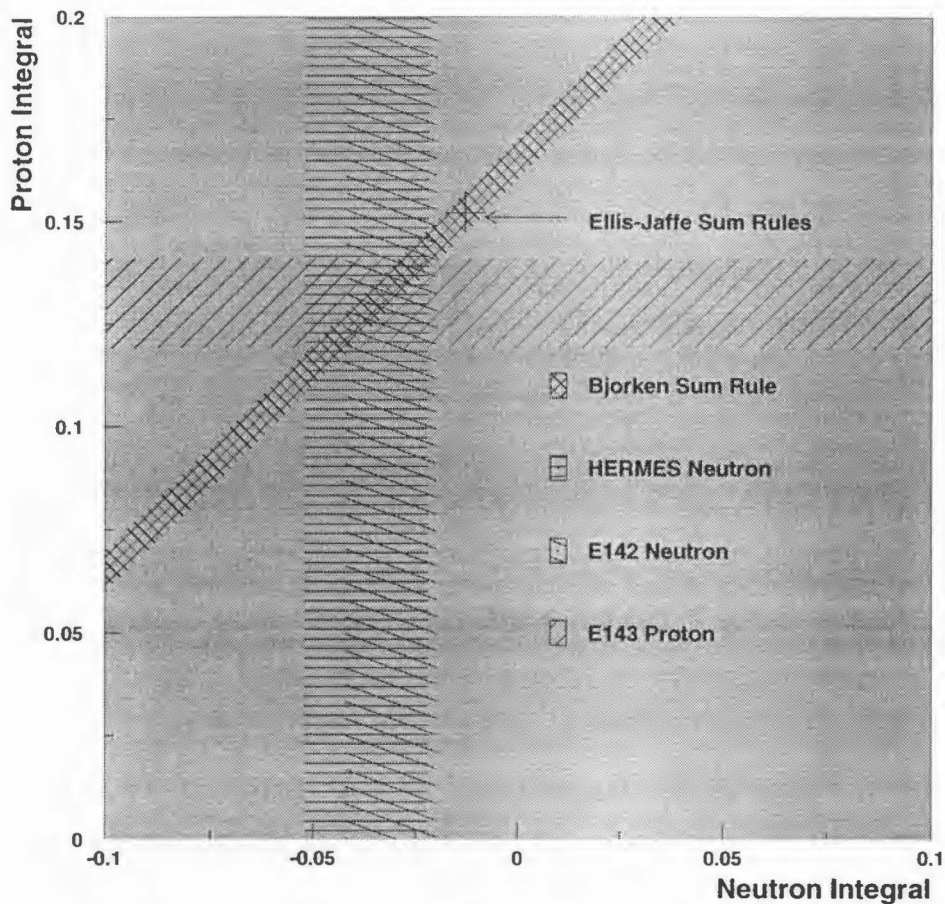
Figure 4.25: The Agreement Between Data From Various Experiments and the Bjorken Sum Rule

4.7.6 Quark Contributions to the Spin of the Nucleon

Using the measured values for the integral Γ_1^n as well as the values of $|\frac{g_A}{g_V}|$ and F/D from hyperon decay, one extracts the system of equations [67] [68]

$$\Gamma_1^n = -\frac{1}{12}(\Delta u - \Delta d)C_{ns} + \frac{1}{36}(\Delta u + \Delta d - 2\Delta s)C_{ns} + \frac{1}{9}(\Delta u + \Delta d + \Delta s)C_s \tag{4.27}$$

$$\Delta u - \Delta d = |\frac{g_A}{g_V}| = 1.257 \tag{4.28}$$

$$3F - D = \Delta u + \Delta d - 2\Delta s = 0.579. \tag{4.29}$$

Solving for $\Delta\Sigma = \Delta u + \Delta d + \Delta s$ we obtain

$$\Delta\Sigma = 38 \pm 11\%. \tag{4.30}$$

This can be compared to the Ellis-Jaffe assumption ($\Delta s = 0$):

$$\Delta\Sigma = \Delta u + \Delta d = 3F - D = 57.9\%. \tag{4.31}$$

Now, the spin decomposition can be performed, yielding

$$\Delta u = 86 \pm 6\% \tag{4.32}$$

$$\Delta d = -41 \pm 6\% \tag{4.33}$$

$$\Delta s = -6.6 \pm 3.7\% \tag{4.34}$$

$$\tag{4.35}$$

which can be interpreted to mean that the quarks carry a fraction of the nucleon spin and that the strange sea is negatively polarized.

Chapter 5   Summary and Conclusion

The neutron spin structure function g_1^n has been measured with a polarized ^3He target. The results are in agreement with those of the SLAC E-142 experiment, but have been determined by an entirely new technique - a windowless polarized internal target with pure atomic species in a positron storage ring. This measurement was made during the commissioning year for the HERMES spectrometer. This indicates the many exciting possibilities of the HERMES spin program, especially with the numerous upgrades to the spectrometer.

The repair of the vertex chambers and insertion of an additional set of drift chambers near the target will greatly increase the tracking resolution and efficiency. The substitution of C_4F_{10} gas in the Cerenkov detector will allow π identification over a much larger momentum range and the proposed upgrade to a RICH (ring imaging Cerenkov) will extend this to π and K identification over the full momentum range of the spectrometer.

Semi-inclusive asymmetries will benefit from both of these upgrades. The higher tracking efficiency will increase the rate of multiple track events and the better hadron identification will allow the identification of the leading hadron. This will allow the decomposition of the asymmetries for different flavors of struck quark and separate valence and sea contributions.

A program of spin physics measurements has begun at HERMES. The 1996 and 1997 proton data will begin the program of semi-inclusive measurements and should produce definitive measurements of the semi-inclusive π asymmetries.

HERMES is part of a second generation of spin physics experiments and will benefit from the high statistics measurements of E154 [69] and E155 [70] at SLAC and upcoming measurements of the high x dependence of A_1^n at CEBAF [71].

Appendix A   Design and Testing of the Hodoscopes

A.1   The HERMES Hodoscopes

A.1.1   Introduction

The HERMES hodoscopes were designed and built by Caltech. Details of the construction and performance are discussed below. Two planes of scintillator are used as hodoscopes and provide fast signals for the first level trigger. The second hodoscope is operated as a preshower detector to improve the particle identification of the spectrometer. A 1.1 cm sheet of lead initiates electro-magnetic showers before the second hodoscope and the calorimeter.

A.1.2   Components and Assembly

The paddles are made from BC-412, a fast scintillator with a large attenuation length (300 - 400 cm). The scintillators are coupled to 5.2 cm diameter Thorn EMI 9954 photomultiplier tubes with fishtail light guides. Assemblies of scintillator, light guide and PMT were glued together with optical cement and installed as single units in the hodoscopes. These units were designed for easy installation in the hodoscope frames and stabilized the PMT lightguide joint against mechanical vibrations. The frame was designed for easy installation and removal of these units. A sketch of the top of an assembled hodoscope is shown in Figure A.1.

The paddles are wrapped in one layer of highly reflective aluminum foil and a layer of opaque tedlar (0.005" thickness). An aluminum end cap was installed over the ends of the foil-wrapped scintillator to ensure electrical contact between the foil wrapping and the hodoscope frame and to produce a uniform mechanical alignment for placement in the frames. The end caps were 1.0 cm high and fit into a series of 0.5 cm deep grooves cut in the base of the hodoscope frames; the top of the end caps
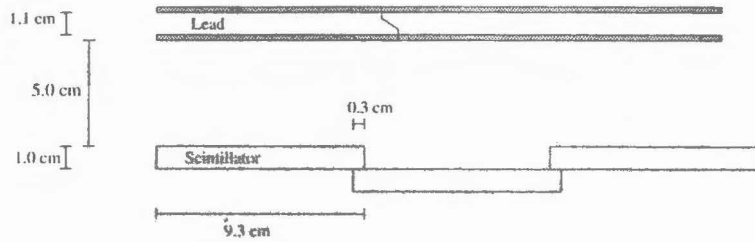
Figure A.2: Hodoscope Paddle Arrangement

was taped to the tedlar to ensure a light tight wrapping of each paddle. The tedlar extended near the end of the lightguides and tape was used to ensure the continuity of the light tight surface over the edge of the PMT.

The modules are staggered in two overlapping rows to provide coverage of the entire region within the acceptance with no gaps between paddles. The rows overlapped 3 mm (Figure A.2) to completely cover the active area of the spectrometer with the minimum number of paddles. This arrangement provides only a crude position measurement as the drift chambers provide much better resolution than the 9 cm wide position resolution of the hodoscopes. The rows of overlapping paddles are arranged so that the first paddle (furthest to the left when looking along the beam direction) is in the front row (closest to magnet) for H1 and the back row for H2.

Each PMT was housed inside a 0.5 mm thick cylindrical μ − metal shield which provided additional magnetic shielding in addition to an integral shield in the PMTs.

The paddles are held by an aluminum frame which gripped the paddles on the lightguide and at the end of the scintillator. The frame was designed to have a small area near the beam pipe and avoid the HERMES acceptance while supporting the lead preshower without sagging more than 1 mm in the middle. Each hodoscope paddle had an aluminum end cap on the end of the scintillator. The aluminum end caps ensured correct alignment in the bottom plate of the hodoscope frame. In the bottom frame, spacers were also mounted near the lightguides. The end caps and spacers secured the hodoscopes in relative position and prevented shifting during the experiment.

A lead sheet is used to initiate the EM showers before the second hodoscope. To protect the lead from creeping and ensure mechanical stability during installation,

two stainless steel sheets are glued to the faces of the lead sheet. Each preshower module has 8 lead sheets attached to the front of the frame. The edges of the lead are beveled as shown in Figure A.2 to prevent any gaps parallel to the path of the particles. Figure 2.17 shows the front view of a hodoscope plane with the lead sheets installed.

A.1.3 PMT Testing

The PMT's exhibited a single P.E. response that was used to calibrate the gain versus voltage for each tube and evaluate the noise levels in the tube. The tubes were operated in a light tight box for one hour to stabilize the dark rate and gain. An attenuated light source was used to provide light in the 'blue' range. The response to single photoelectrons was recorded. If the single P.E. peak could not be clearly resolved from the pedestal (Peak to valley ratio of 1.5), the tubes were rejected. The voltage dependence of the gain was fitted to an exponential and used to select appropriate voltages for operation at DESY.

The noise at the single photoelectron level is not relevant for the operation of the experiment. Several hundred photoelectrons were observed for a minimum ionizing particle traveling through the scintillator, and the trigger threshold was set at half of the signal height for minimum ionizing particles. The dark noise from the tubes is small at this threshold if the single photoelectron peak can be resolved.

A.1.4 Attenuation

The paddles were required to have an effective attenuation length of at least 250 cm to be used in the HERMES spectrometer. This limited the variation in signals due to attenuation to 30% from top to bottom of a paddle within the acceptance.

The effective attenuation length was measured for each paddle at Caltech. Two pairs of finger scintillators were placed above and below two hodoscope paddles (Figure A.4) to identify a sample of cosmic rays through the paddles. The spectra of minimum ionizing particles were recorded for two positions near the ends of each scintillator paddle. An effective attenuation length was calculated from the most likely energy deposition from a fit to a Landau distribution [72]. The effective atten-
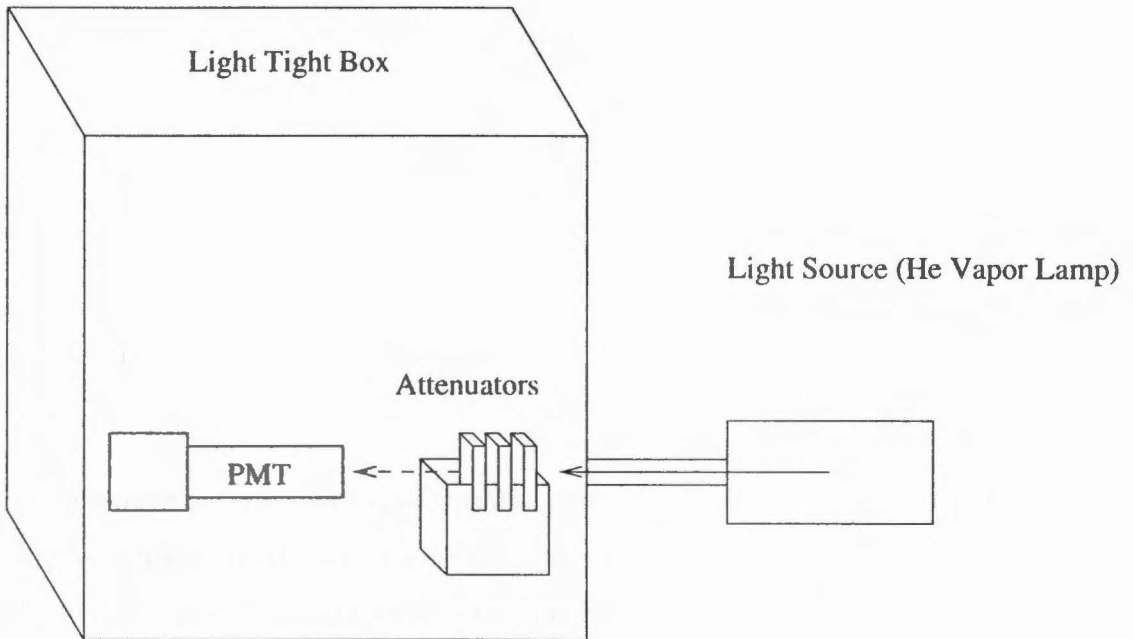
Figure A.3: PMT Gain Measurements

Front View

TF 1

TF2

Paddle 1 (Top)   76 cm

7 cm   Paddle 2 (Bottom)

TF4

TF3

1 cm

9 cm

Side View

9 cm

15 cm
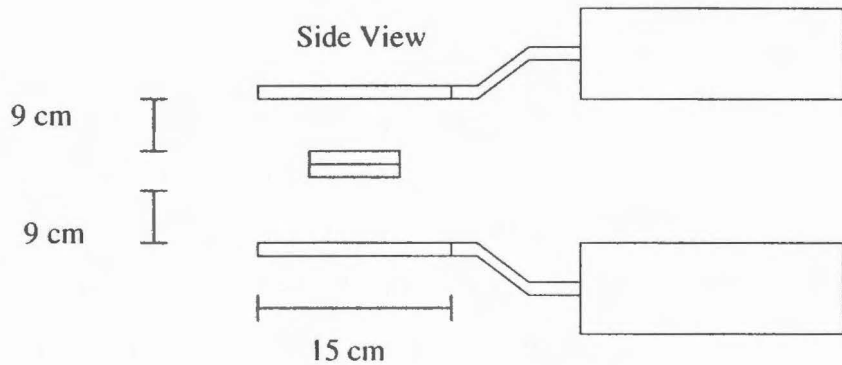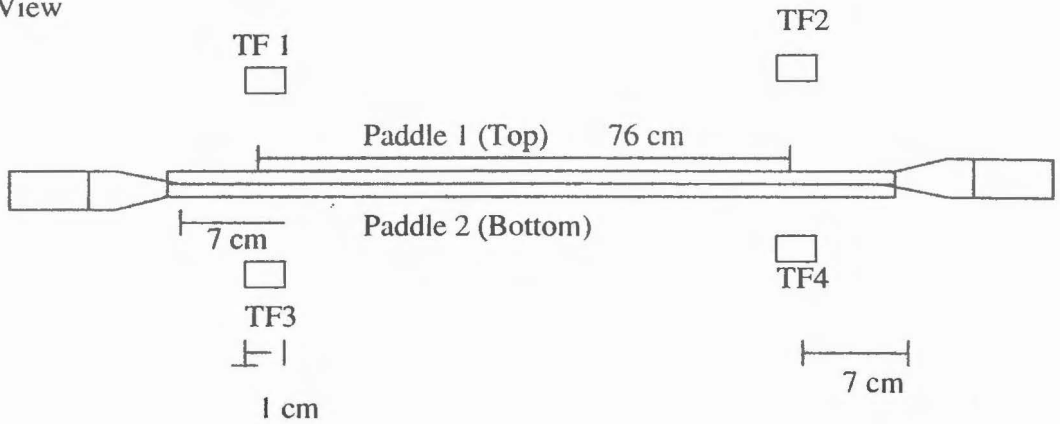
Figure A.4: Hodoscope Paddle Attenuation Tests

uation length assumes an exponential dependence for the attenuation in the paddles. This length was used to quantify the attenuation of each paddle and the measured effective attenuation lengths were between 250 and 450 cm. This effective attenuation is an overestimate of the actual attenuation length because of the reflection from the reflective aluminum at the end of the paddle. The actual position dependence of the attenuation is more complicated than a simple exponential decay as discussed next.

A.1.5   Detailed Attenuation Studies

An additional series of attenuation tests were performed to determine the attenuation as a function of position along the paddle. Reflections from the end of the scintillator mitigate the attenuation near the end of the paddle and acceptance effects near the light guide also alter the distribution. The resulting distribution differs by up to

10% from an exponential dependence. This dependence was parameterized to correct the position dependence of the signals in the spectrometer. Figure A.5 shows a parameterization of the attenuation distribution for a paddle with a relatively good effective attenuation (412 cm) as an example. The data was parameterized via

$$E_{corr} = \frac{E}{(1 + A(\lambda_{eff})y^2)e^{-y/B(\lambda_{eff})}} \tag{A.1}$$

where λ_{eff} is the measured attenuation length; A and B are functions of the attenuation length and have typical values of 1.1×10^{-4} cm^{-2} for A and 96 cm for B for λ_{eff} of 300 cm.

A.1.6   Final Gain Tests

After the scintillator assemblies were glued together, a final test was performed with the cosmic ray attenuation measurement apparatus. This provided the total gain for the assembly at a selected voltage and checked the attenuation measurement. The gain of the assemblies was up to a factor of two higher with a glued PMT lightguide joint compared to a coupling with optical grease. The gain measured in this test was used with the gain curve measured for the PMT to select an appropriate voltage for the assembly.

The paddles with longer attenuation lengths were used in the H2 detector to make the attenuation corrections smaller. Paddles with shorter attenuation lengths were installed on the outside where there is little rate. The paddles in the H2 had effective attenuation lengths between 450 cm in the middle and 300 cm at the edges. This kept the attenuation corrections to under 25% in the preshower detector. The attenuation lengths were between 300 cm in the middle and 250 cm at the edges for the H1. The first hodoscope has only photon particle identification ability where the tag for a photon is essentially no pulse height, so gain corrections are not as important.

A.1.7   Y Position Dependence

The attenuation measurements are used to correct the y position dependence of the data in the off-line analysis.
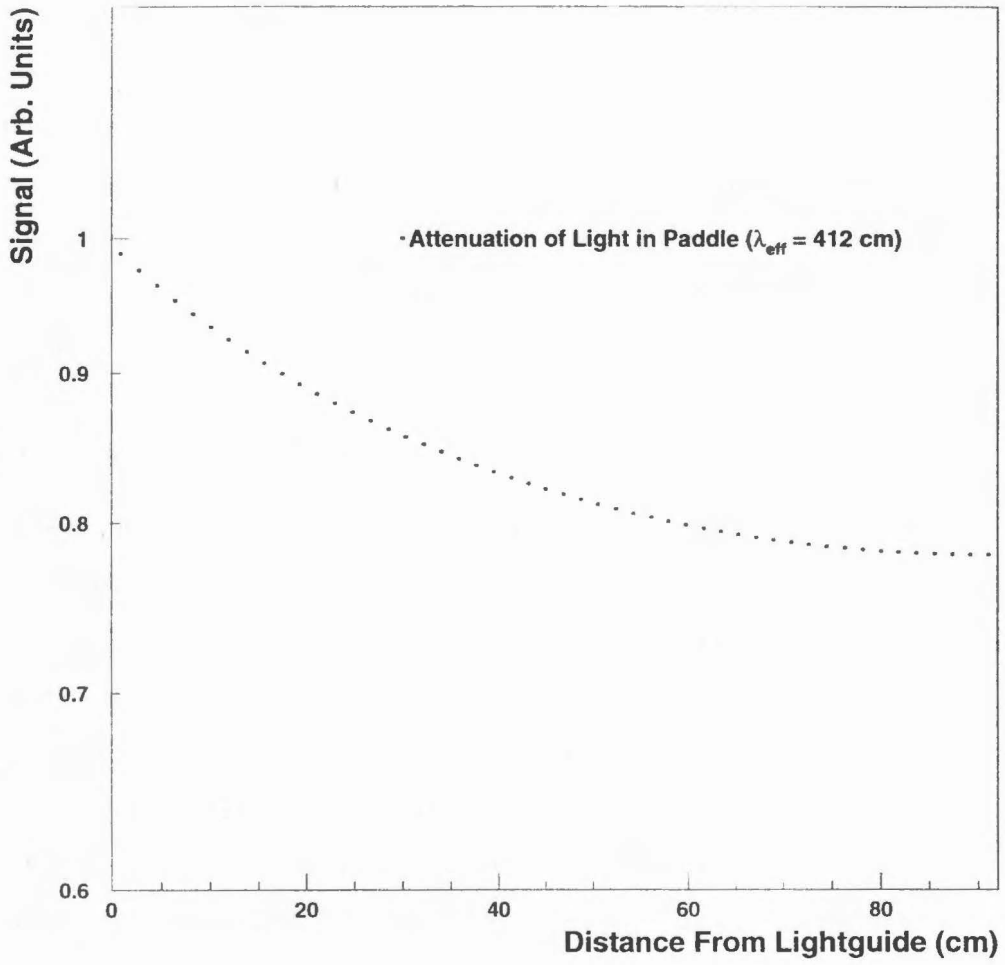
Figure A.5: Light Attenuation in Hodoscope Paddles

After a correction is made for the attenuation in the paddle, there is less than a 1% systematic dependence of reconstructed energy on position along the paddles. Figure A.1.7 shows the most probable energy deposition of minimum ionizing particles as a function of position in the second hodoscope. Monte Carlo simulations suggest that a gain shift of this size will have no appreciable effect on the particle identification in the HERMES spectrometer.

The variations of the height of the minimum ionizing signal observed on an oscilloscope are much smaller (a few %) than the variations in the total integrated charge. This is a result of reflections from the end of the paddle. For signals near the lightguide, two peaks are resolved by the phototube. A large peak from light traveling toward the tube followed by a smaller reflection peak up to ten ns later. The signal from near the end cap has a smaller total charge, but the two peaks (direct and reflected) are not resolved. This significantly reduces the effect of attenuation on the trigger.

A.1.8 X Position Dependence

Calibrations of the HERMES hodoscopes were performed in two ways. The GMS system used a series of laser pulses to calibrate the gain relative to a photodiode (Section 2.4.12) and the minimum ionizing particles were used to provide a fill to fill calibration of the hodoscope paddles. The gains measured this way are used both to track any significant changes in the hodoscope gains and to correct the gains during a second pass of the off-line analysis.

The gain variations in the paddles was very small and agreed for the two methods. The average gain per fill for most paddles changed only a few percent over the course of the entire year. The accuracy of the minimum ionizing measurement depended strongly on the position of the paddle. The central paddles had very high rates, but the event rate falls quickly away from the central region. The gain could be measured to within 1% for all but the four paddles at each edge of the second hodoscope and six paddles at each edge of the first hodoscope within a run. The gain variation of eight H2 paddles for the first month of data are shown in Figure A.7. The outer paddles mentioned above detect particles which are bent a large amount in the magnet, that
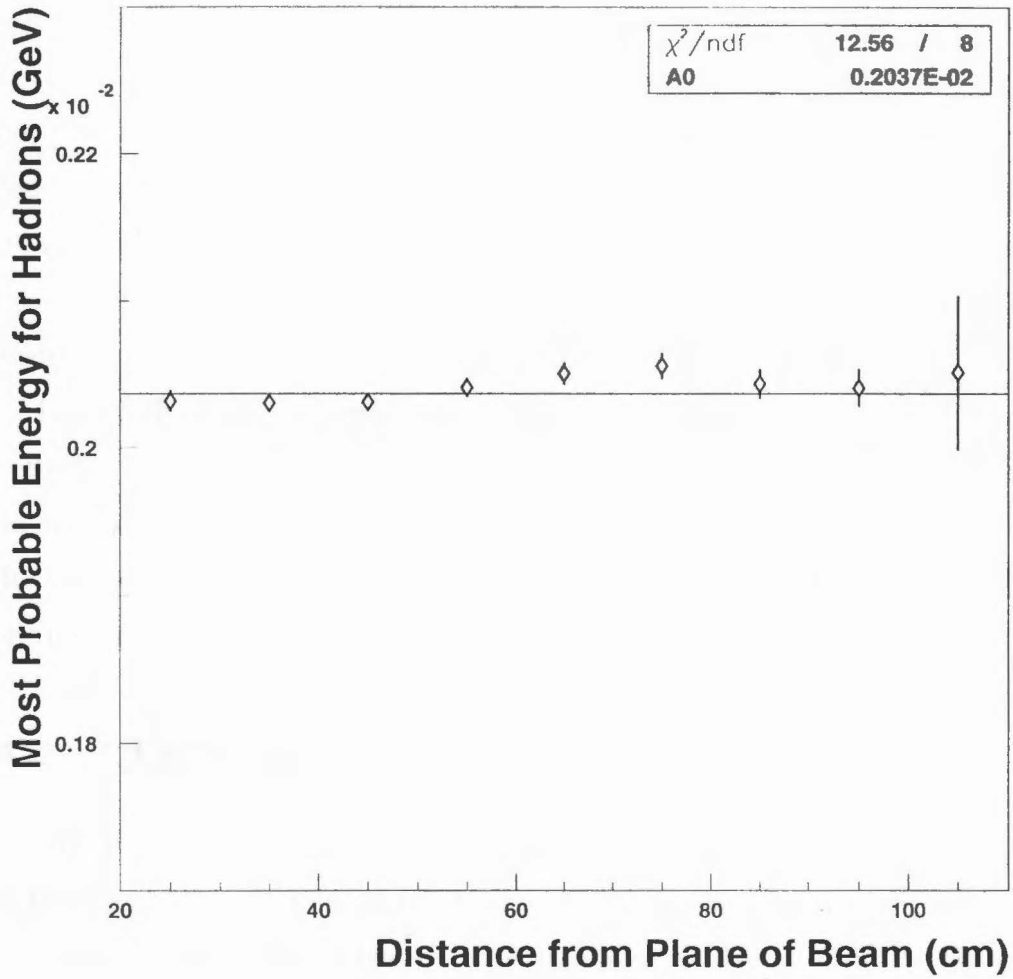
Figure A.6: Hodoscope Y Dependence After Off-line Corrections

is, particles with very low momentum. The DIS positrons are all incident on the well calibrated paddles.

A.1.9 Particle Identification

The H2 counter provides discrimination between positrons and hadrons. A radiator initiates electromagnetic showers that are detected in the H2 scintillator.

The 1.1 cm lead sheet represent 2 radiation lengths and high energy positrons passing through the sheet will begin electromagnetic showers. The energy deposition distribution of positrons in the scintillator is very broad because the deposition is very sensitive to the depth of the lead where the shower begins. The mean energy deposition in the scintillator is near 40 MeV. The nuclear interaction length is 10 cm for lead and most of the hadrons pass through the lead sheet without interacting. These non-interacting hadrons deposit significantly less energy in the scintillator than positrons with equivalent momentum.

The width of the lead preshower was chosen to maximize the hadron separation of both the calorimeter and preshower together. Increasing the width of the lead aids the hadron separation of the preshower but hurts the energy resolution and therefore the hadron separation of the calorimeter. The particle identification abilities of the preshower and calorimeter were tested at CERN.

A.2 CERN Test Beam

An initial test of the preshower was performed at the X1 test beam at CERN from October 11 to 21, 1994, in conjunction with the WA89 collaboration. Additional data were taken to measure the energy resolution and linearity of the calorimeter with the preshower installed and to test the particle identification ability of the detectors at an energy range relevant to HERMES.

A.2.1 Experimental Setup

Particles were identified by two threshold Cerenkov detectors and three finger scintillators. The first Cerenkov contained He gas and the second, N_2. The pressure in the
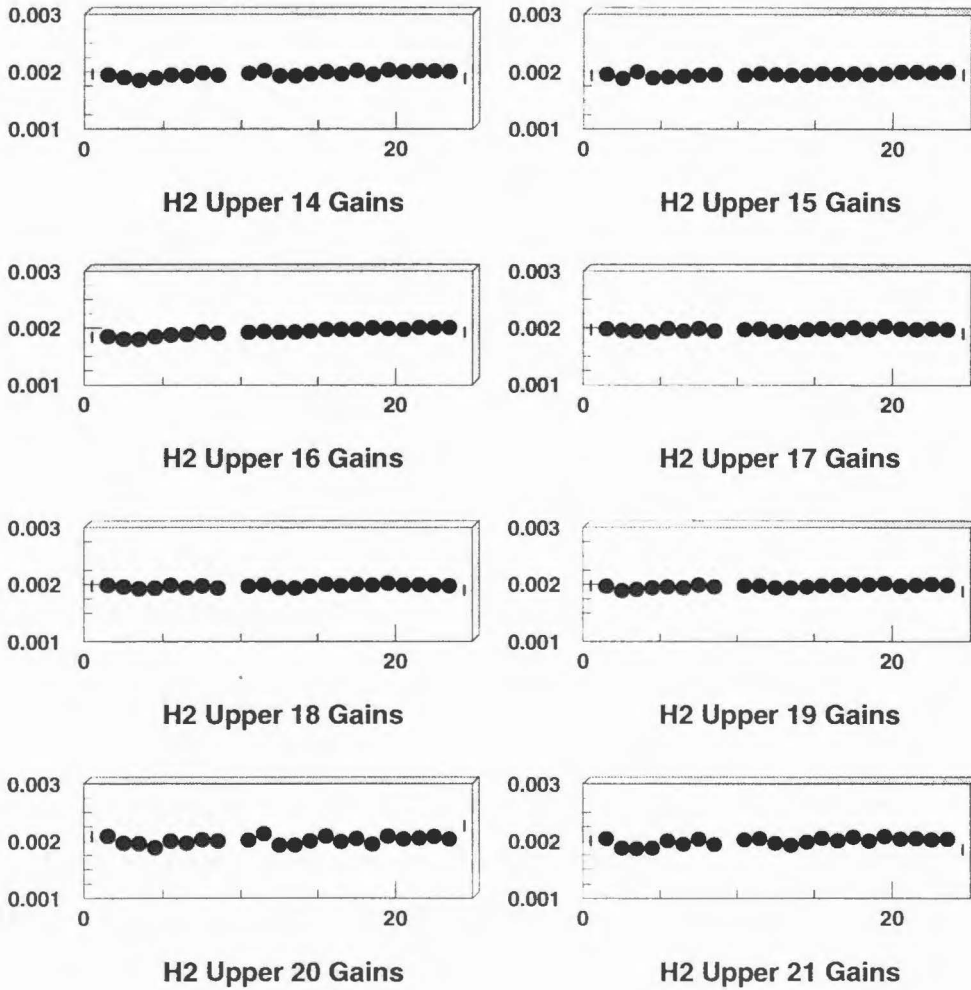
Hodoscope Gains vs Fill

H2 Upper 14 Gains

H2 Upper 15 Gains

H2 Upper 16 Gains

H2 Upper 17 Gains

H2 Upper 18 Gains

H2 Upper 19 Gains

H2 Upper 20 Gains

H2 Upper 21 Gains

Figure A.7: Gain Variation During the First 25 Fills

| Beam Momentum | 3 X 3 Cluster Resolution | |
(GeV/c)	Without Preshower	With Preshower
5	3.9 %	6.8
10	3.2 %	5.0
15	2.7 %	4.3
20	2.7 %	3.6
25	2.5 %	3.1

Table A.1: Calorimeter Resolution With and Without Lead Preshower

two Cerenkov detectors was varied so that the detectors could be used for electron π separation at various momenta. The trigger was a coincidence of the beam burst with the S1 and S2 finger scintillators.

An array of 60 calorimeter blocks (6 X 10) was mounted on a movable platform at the X1 test area. Of these 60 blocks, 36 could be centered on the beam. A test preshower was placed 10 cm in front of the face of the calorimeter blocks. The test preshower was a hodoscope scintillator paddle with a small (9.3 by 9.3 by 1.1cm) lead and stainless steel sandwich mounted 5 cm in front of a hodoscope scintillator paddle. The sandwich had an identical profile as the preshower sheets used in the spectrometer.

A.2.2 Shower Distributions

The energy leakage from 3 X 3 clusters of calorimeter blocks was measured versus the position of the beam on the center block of the cluster. The analysis suggests that 3 X 3 clusters contain the majority of the energy of the shower regardless of the incident position and these clusters can be used to measure the energy deposited by electromagnetic showers in the calorimeter. The resolution of these clusters versus electron beam energy is shown in Table A.1.

A.2.3 The Linearity of the Calorimeter

The absolute energy calibration of the 3 X 3 matrices of lead glass counters is shown in Figure A.8. From an energy of 5 GeV to 30 GeV, the data is reproduced to within 1% by a linear fit. With the inclusion of DESY test beam results, this linearity can be extended down to 1 GeV.
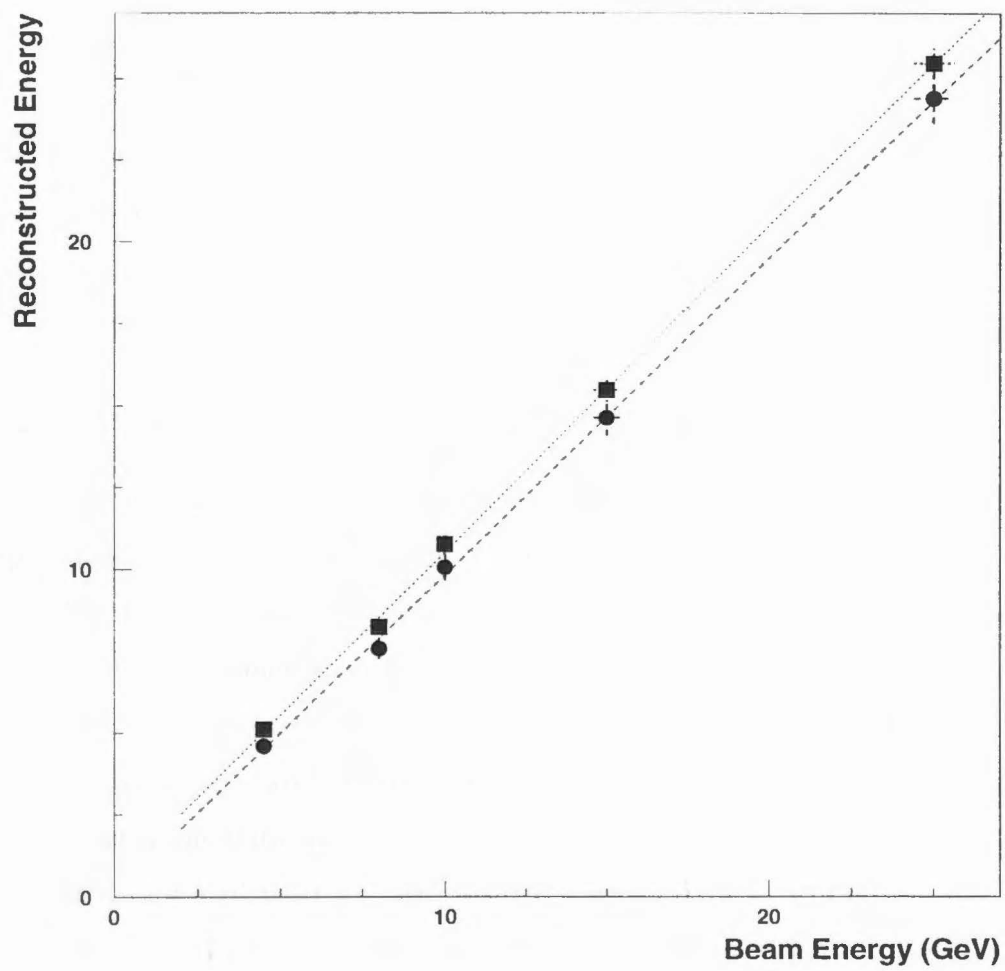
Figure A.8: Calorimeter Linearity

Momentum	10 GeV/c		15 GeV/c	
Cut (ADC)	π rejection	e^- efficiency	π rejection	e^- efficiency
100	0.725 ± 0.005	0.998 ± 0.001	0.706 ± 0.004	0.998 ± 0.001
200	0.895 ± 0.004	0.996 ± 0.001	0.880 ± 0.003	0.997 ± 0.001
300	0.921 ± 0.003	0.990 ± 0.002	0.912 ± 0.003	0.995 ± 0.001
400	0.933 ± 0.003	0.983 ± 0.002	0.923 ± 0.002	0.988 ± 0.002
500	0.939 ± 0.003	0.969 ± 0.003	0.929 ± 0.002	0.979 ± 0.003
600	0.943 ± 0.003	0.952 ± 0.003	0.933 ± 0.002	0.970 ± 0.003
700	0.946 ± 0.003	0.933 ± 0.004	0.937 ± 0.002	0.959 ± 0.004

Table A.2: Hadron Rejection and Electron Identification of the Preshower

A.2.4 The Hodoscope Response

The response of the hodoscope to hadrons and positrons has been shown in Figure 3.1. The CERN tests provided the first measurements of the preshower response to high energy particles. The mean energy deposition of electrons in the scintillator is shown as a function of beam energy in Figure A.9.

A.2.5 Particle Identification

The main goal of the CERN tests was the measurement of the particle identification capabilities of the combined preshower and calorimeter. The hadron distribution for HERMES is expected to be a strong function of momentum with the majority of the hadrons at low momentum. For the identification of deep inelastic positrons, it is important to have good pion rejection between 5 and 15 GeV/c. Data with the pion and electron beams was taken at 10 and 15 GeV/c. The pion rate was too low to take a reasonable data sample at momenta below 10 GeV/c in the available time.

Data samples of 6381 π^- and 4030 e^- were taken at 10 GeV/c and 11086 π^- and 2946 e^- at 15 GeV/c. The measured efficiencies and hadron rejections for the preshower and calorimeter are tabulated in Tables A.2 and A.3. The hadron rejection and electron efficiency for the preshower are also plotted in Figures A.10 and A.11.
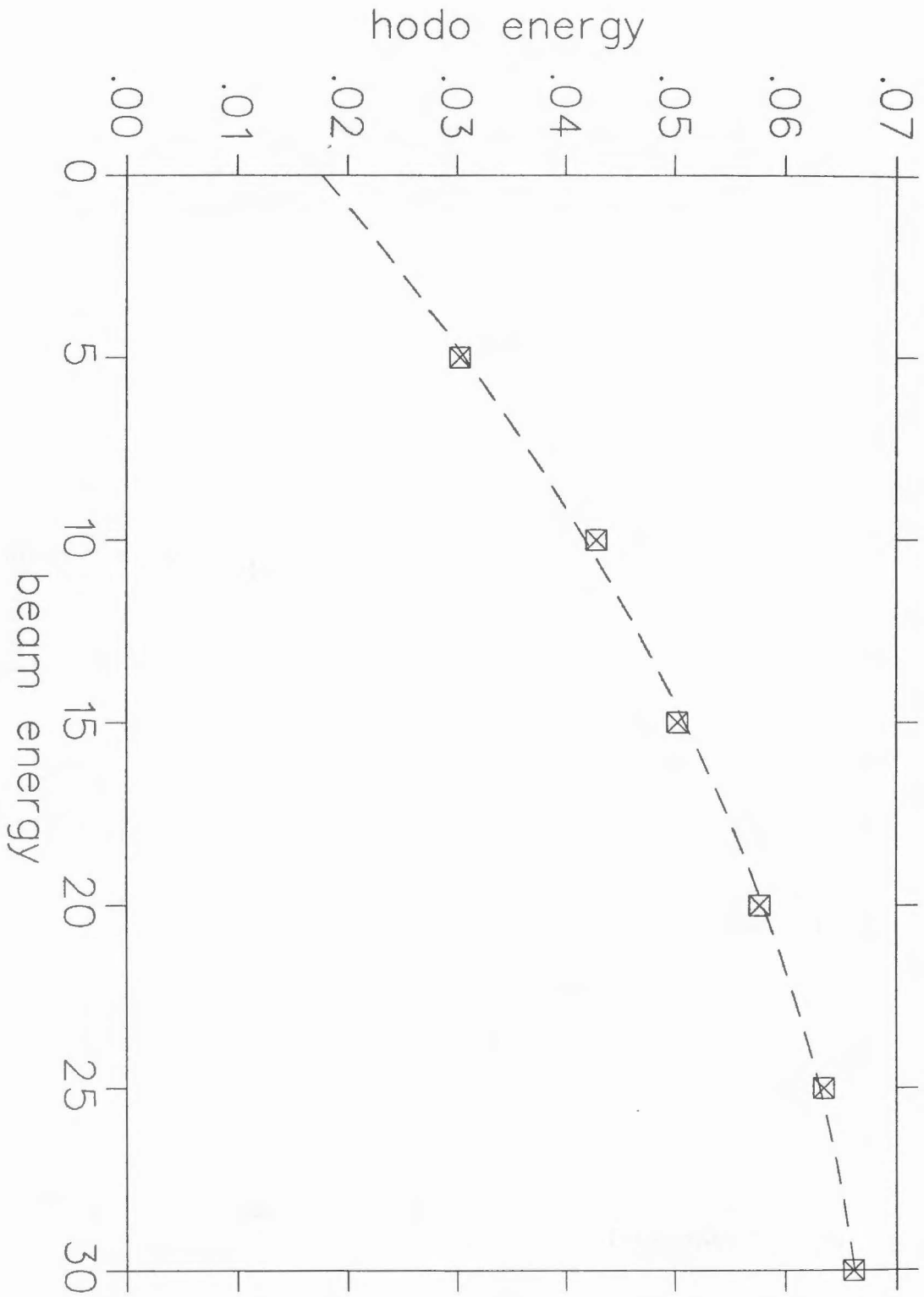
Figure A.9: Mean Electron Energy vs Momentum for the Preshower: Both Scales in GeV

Momentum	10 GeV/c		15 GeV/c	
Cut (E/P)	π rejection	e^- efficiency	π rejection	e^- efficiency
0.7	0.047 ± 0.003	0.987 ± 0.002	0.035 ± 0.002	0.997 ± 0.001
0.8	0.028 ± 0.002	0.984 ± 0.002	0.020 ± 0.001	0.991 ± 0.002
0.9	0.009 ± 0.001	0.974 ± 0.003	0.012 ± 0.001	0.976 ± 0.003

Table A.3: Hadron Rejection and Electron Identification of the Calorimeter

Figure A.10: Electron Efficiency of Preshower

Figure A.11: Pion Rejection in Preshower

Appendix B   Merging Independent Results

Two groups independently analyzed the 1995 HERMES data. The NAPA (North American Physics Analysis) results have been presented in detail in this thesis while the EURO (European Physics Analysis) results are presented elsewhere. [58] Since the time dependences and results for the two analyses were very simila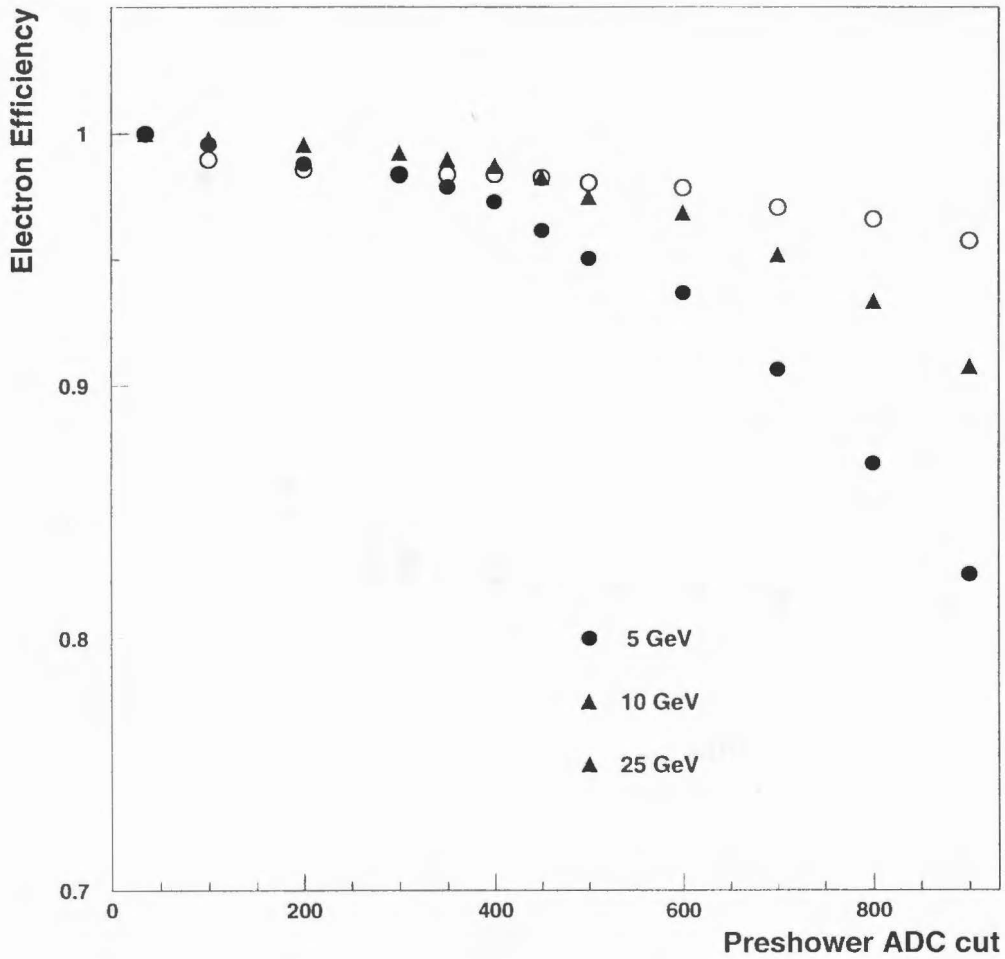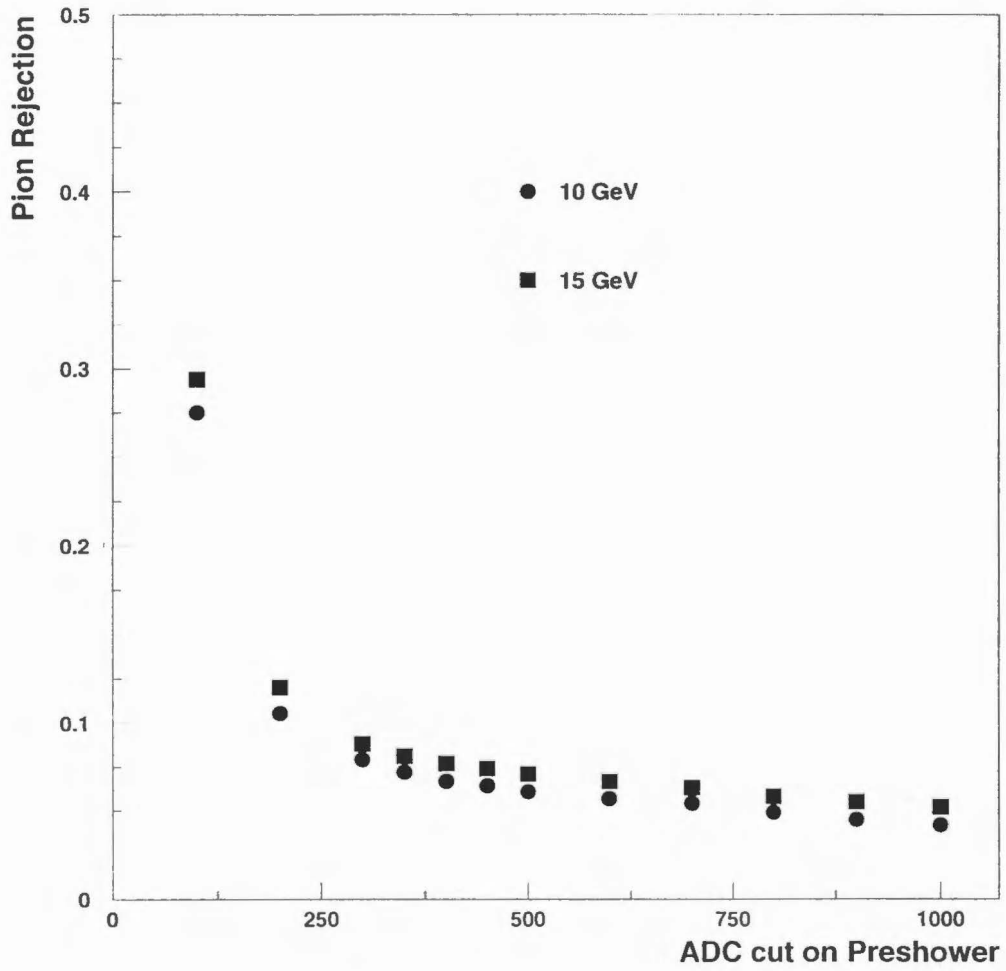r, it was not clear which analysis should be selected for publication. It was decided that an average of the two results would be created for the official HERMES 1995 $A_1^{^3He}$.

$<x>$	NAPA $A_1^{^3He}\pm$stat.	EURO $A_1^{^3He}\pm$stat.	Average
0.035	-0.0246 ± 0.0113	-0.0244 ± 0.0109	-0.0245 ± 0.0111
0.049	-0.0250 ± 0.0122	-0.0280 ± 0.0121	-0.0265 ± 0.0121
0.066	-0.0137 ± 0.0130	-0.0222 ± 0.0128	-0.0180 ± 0.0129
0.088	-0.0317 ± 0.0149	-0.0305 ± 0.0147	-0.0311 ± 0.0148
0.119	-0.0153 ± 0.0159	-0.0327 ± 0.0156	-0.0240 ± 0.0158
0.168	-0.0395 ± 0.0190	-0.0387 ± 0.0184	-0.0391 ± 0.0187
0.244	-0.0251 ± 0.0241	-0.0166 ± 0.0232	-0.0208 ± 0.0236
0.342	$+0.0292 \pm 0.0416$	$+0.0187 \pm 0.0401$	$+0.0239 \pm 0.0408$
0.464	-0.0394 ± 0.0610	-0.0388 ± 0.0597	-0.0391 ± 0.0604

Table B.1: Averaged Measurement of $A_1^{^3He}$

$<x>$	Average $A_1^{^3He}\pm$stat.	$A_1^n\pm$stat.	$g_1^n\pm$stat.
0.035	-0.0245 ± 0.0111	-0.1045 ± 0.0411	-0.3203 ± 0.1260
0.049	-0.0265 ± 0.0121	-0.1098 ± 0.0450	-0.2498 ± 0.1024
0.066	-0.0180 ± 0.0129	-0.0758 ± 0.0483	-0.1316 ± 0.0839
0.088	-0.0311 ± 0.0148	-0.1232 ± 0.0566	-0.1630 ± 0.0750
0.119	-0.0240 ± 0.0158	-0.0953 ± 0.0631	-0.0928 ± 0.0614
0.168	-0.0391 ± 0.0187	-0.1563 ± 0.0785	-0.1029 ± 0.0517
0.244	-0.0208 ± 0.0236	-0.0748 ± 0.1057	-0.0296 ± 0.0419
0.342	$+0.0239 \pm 0.0408$	$+0.1478 \pm 0.1981$	$+0.0317 \pm 0.0425$
0.464	-0.0391 ± 0.0604	-0.1560 ± 0.3270	-0.0146 ± 0.0305

Table B.2: A_1^n and g_1^n From the Average $A_1^{^3He}$

There is little statistical motivation for averaging two alternative measurements with the same data, but the differences in the results are small. The values of g_1^n (Table B.2) calculated from the average $A_1^{^3He}$ values are consistent with both the EURO and

NAPA g_1^n values. The integral of g_1^n over the measured region is -0.034 ± 0.012, the average of -0.035 ± 0.012 for the European analysis and -0.033 ± 0.012 for the American analysis. The difference between the analyses is of the same order as the cut dependence studies and no additional systematic error has been assigned for the difference between the alternate analyses.

$< x >$	NAPA $g_1^n \pm$stat.	EURO $g_1^n \pm$stat.	Average
0.035	-0.3214 ± 0.1283	-0.318 ± 0.048	-0.3197 ± 0.1267
0.049	-0.2371 ± 0.1032	-0.265 ± 0.029	-0.2510 ± 0.1041
0.066	-0.1037 ± 0.0846	-0.161 ± 0.023	-0.1323 ± 0.0858
0.088	-0.1660 ± 0.0755	-0.167 ± 0.021	-0.1665 ± 0.0767
0.119	-0.0589 ± 0.0618	-0.131 ± 0.016	-0.0949 ± 0.0619
0.168	-0.1040 ± 0.0525	-0.103 ± 0.017	-0.1035 ± 0.0522
0.244	-0.0373 ± 0.0427	-0.024 ± 0.010	-0.0307 ± 0.0424
0.342	$+0.0373 \pm 0.0434$	$+0.025 \pm 0.013$	0.0312 ± 0.0427
0.464	-0.0147 ± 0.0308	-0.011 ± 0.011	-0.0128 ± 0.0304

Table B.3: Averaged Measurement of g_1^n at Measured Q^2

To compensate for this effect, the statistical error bars of the published data have been expanded by 10% to account for these fluctuations. The confidence levels of the many time stability plots improve significantly if the error bars are increased 10%. The χ^2 is reduced by 20% and the three problematic distributions have a χ^2/df of 1. This may be an over correction since two of the plots have a χ^2/df of 0.8, but the decision was made to publish a conservative error calculation.

Bibliography

[1] G. Baum *et al.*, Phys. Rev. Lett. **51**, 1135 (1983).

[2] J. Ashman *et al.*, Phys. Lett. B **206**, 364 (1988).

[3] B. Adeva *et al.*, Phys. Lett. B **302**, 533 (1993).

[4] P. Anthony *et al.*, Phys. Rev. D **54**, 6620 (1996).

[5] K. Abe *et al.*, Phys. Rev. Lett. **75**, 25 (1995).

[6] D. Griffiths, *Introduction to Elementary Particles* (John Wiley and Sons, Inc., New York, 1987).

[7] V. Hughes and J. Kuti, Ann. Rev. Nucl. Part. Sci. **33**, 611 (1983).

[8] F. Halzen and A. Martin, *Quarks and Leptons* (John Wiley and Sons, Inc., New York, 1984).

[9] A. Hey and J. Mandula, Phys. Rev. D **5**, 2610 (1972).

[10] M. Doncel and E. de Rafael, Nuovo Cimento **4A**, 363 (1971).

[11] J. Bjorken, Phys. Rev. **179**, 1547 (1969).

[12] J. Bjorken and E. Paschos, Phys. Rev. **185**, 1975 (1969).

[13] F. Close, *An Introduction to Quarks and Partons* (Academic Press, New York, 1979).

[14] J. Bjorken, Phys. Rev. **148**, 1467 (1966).

[15] S. Larin and J. Vermaseren, Phys. Lett. B **259**, 345 (1991).

[16] M. Schmelling and R. St.Dennis, Phys. Lett. B **329**, 393 (1993).

[17] J. Ellis and R. Jaffe, Phys. Rev. D **9**, 1444 (1974).

[18] F. Close and R. Roberts, Phys. Lett. B **316**, 165 (1993).

[19] S. Larin, Phys. Lett. B **334**, 192 (1994).

[20] M. Alguard *et al.*, Phys. Rev. Lett. **41**, 70 (1978).

[21] A. Sokolov and I. Ternov, Sov. Phys. Doklady **8**, 1203 (1964).

[22] M. Dueren, Ph.D. thesis, Univ. Erlangen, 1995.

[23] V. Bargmann, L. Michel, and V. Telegdi, Phys. Rev. Lett. **2**, 435 (1959).

[24] J. Johnson *et al.*, N.I.M. **204**, 261 (1983).

[25] J. Buon and K. Steffen, N.I.M. **A245**, 248 (1986).

[26] D. Barber *et al.*, N.I.M. A **329**, 79 (1993).

[27] T. Gentile and R. McKeown, Phys. Rev. A **47**, 456 (1993).

[28] H. Collaboration, Technical Report No. 93/06, DESY-PRC (unpublished).

[29] C. E. Jones *et al.*, Phys. Rev. C **47**, 110 (1993).

[30] T. Gentile and R. McKeown, NIM A **389**, 389 (1997).

[31] J. Price and W. Haeberli, N.I.M. A **349**, 321 (1994).

[32] W. Lorenzon *et al.*, Phys. Rev. A **47**, 468 (1993).

[33] M. Pitt *et al.*, in *Proc. of Int. Workshop on Polarized Beams and Polarized G as Targets* (in preparation, Koln, 1995).

[34] M. Dell'Orzo and L. Ristori, N.I.M. A **278**, 436 (1989).

[35] P. Battaiotto *et al.*, N.I.M. A **287**, 431 (1990).

[36] M. Dell'Orzo and L. Ristori, N.I.M. A **287**, 436 (1990).

[37] W. Wander, Ph.D. thesis, Univ. Erlangen, 1996.

[38] M. Kolstein, private communication, 1996.

[39] C. Fabjan, in *Experimental Techniques in High Energy Physics*, edited by T. Ferbel (Addison-Wesley Publishing Company, Inc., Menlo Park, 1987).

[40] H. Avakian *et al.*, N.I.M. **A378**, 155 (1996).

[41] R. Brun *et al.*, Technical Report No. DD/EE/84-1, CERN (**unpublished**).

[42] R. Fernow, *Introduction to Experimental Particle Physics* (Cambridge University Press, Cambridge, 1986).

[43] P. D. Group, Phys. Rev. D **54**, 0 (1996).

[44] W. Allison and R. Wright, in *Experimental Techniques in High Energy Physics*, edited by T. Ferbel (Addison-Wesley Publishing Company, Inc., Menlo Park, 1987).

[45] J. Bjorken and S. Drell, *Relativistic Quantum Mechanics* (McGraw-Hill, Inc., New York, 1965).

[46] R. Kaiser, private communication, 1997.

[47] M. Spengos, Ph.D. thesis, The American University, 1994.

[48] L. Mo and Y. Tsai, Rev. Mod. Phys. **41**, 205 (1969).

[49] I. Akushivich and N. Shumeiko, J. Phys. G: Nucl. Part. Phys. **20**, 513 (1994).

[50] I. Akushivich and N. Shumeiko, HERMES Internal Note **95-25**, 0 (1995).

[51] A. Schaefer, Phys. Lett. B **208**, 175 (1987).

[52] D. Ryckbosch *et al.*, HERMES Internal Note **96-046**, 0 (1996).

[53] M. Ferstl, private communication, 1997.

[54] B. Blankleider and R. Woloshyn, Phys. Rev. C **29**, 538 (1984).

[55] Friar, Phys. Rev. C **42**, 2310 (1990).

[56] C. C. degli Atti *et al.*, Phys. Rev. C **48**, R968 (1993).

[57] P. Amaudruz *et al.*, Phys. Lett. B **295**, 159 (1992).

[58] M. Dueren, Technical Report No. 97/007, DESY (unpublished).

[59] L. Whitlow *et al.*, Phys. Lett. B **250**, 193 (1990).

[60] K. Abe *et al.*, Phys. Lett. B **364**, 61 (1995).

[61] K. Abe *et al.*, SLAC-PUB-7460, 1997.

[62] R. Heimann, Nucl. Phys. B **64**, 429 (1973).

[63] S. B. amd P.V. Landshoff, Phys. Lett. B **336**, 537 (1994).

[64] B. Badelek *et al.*, Rev. Mod. Phys. **64**, 927 (1992).

[65] R. Ball *et al.*, Phys. Lett. B **378**, 2557 (1995).

[66] G. Farrar and D. Jackson, Phys. Rev. Lett **35**, 1416 (1975).

[67] J. Ellis and M. Karliner, Phys. Lett. B **213**, 73 (1988).

[68] J. Ellis and M. Karliner, Phys. Lett.. B **341**, 397 (1985).

[69] K. Abe *et al.*, Phys. Rev. Lett. **79**, 26 (1997).

[70] R. Arnold *et al.*, SLAC Proposal E155, 1993.

[71] Z.-E. Meziani, CEBAF Proposal, 1994.

[72] T. Tabata and R. Ito, N.I.M. **158**, 521 (1979).